IS-T 1731

NMR and NQR study of the thermodynamically stable quasicrystals

by

Shastri, Ananda

PHD Thesis submitted to Iowa State University

Ames Laboratory, U.S. DOE
Iowa State University
Ames, Iowa 50011

Date Transmitted: February 10, 1995

PREPARED FOR THE U.S. DEPARTMENT OF ENERGY
UNDER CONTRACT NO. W-7405-Eng-82.

DISCLAIMER

NMR and NQR study of the thermodynamically stable quasicrystals

Ananda Shastri

Major Professor: Dr. F. Borsa
Iowa State University

^{27}Al and ^{63,65}Cu NMR measurements are reported for powder samples of stable AlCuFe and AlCuRu icosahedral quasicrystals and their crystalline approximants, and for a AlPdMn single grain quasicrystal. Furthermore, ^{27}Al NQR spectra at 4.2 K have been observed in the AlCuFe and AlCuRu samples. From the quadrupole perturbed NMR spectra at different magnetic fields, and from the zero field NQR spectra, a wide distribution of local electric field gradient (EFG) tensor components and principal axis system orientations was found at the Al site. A model EFG calculation based on a 1/1 AlCuFe approximant was successful in explaining the observed NQR spectra. It is concluded that the average local gradient is largely determined by the p - electron wave function at the Al site, while the width of the distribution is due to the lattice contribution to the EFG. Comparison of ^{63}Cu NMR with ^{27}Al NMR shows that the EFG distribution at the two sites is similar , but that the electronic contribution to the EFG is considerably smaller at the Cu site, in agreement with a more s - type wave function of the conduction electrons. The overall spread of EFG values is well reproduced by the calculation based on the approximant. However, the experimental spectra indicate a much larger number of non - equivalent sites when compared with the simulated NQR spectra based on the 1/1 approximant. It is argued that the short range, local chemical order is well represented by the approximant, but differences in coordination must be

included at intermediate range in the quasicrystal. Measurements of ^{27}Al Knight shift, magnetic susceptibility, and nuclear spin - lattice relaxation time as a function of temperature yield results which indicate a reduction of the density of states at the Fermi level by a factor of 7 or 8 from the value in Al metal, consistent with the notion of a pseudogap for these quasicrystals. No differences in the measured parameters were detected as a function of composition of the quasicrystalline alloys, arguing against a fine structure in the density of states at the Fermi level.

TABLE OF CONTENTS

CHAPTER 1. INTRODUCTION

A. Historical Background

Before the discovery of quasicrystals it had generally been thought that five-fold symmetry was forbidden in solids, that Bragg reflection of x-rays implied a periodic arrangement of atoms in a material, and that all solids could generally be classified as either crystalline or amorphous. In 1984 when rapidly solidified aluminum-manganese alloys produced diffraction patterns consisting of sharp diffraction peaks that showed icosahedral symmetry, these generally held beliefs of solid state physics began to receive intense scrutiny by many physicists, metallurgists, and crystallographers [1].

A quasicrystal is neither periodic nor disordered. Mathematically, quasicrystallinity is a distinct type of long-range translational order that follows as a consequence of its noncrystallographic orientational symmetry (e.g. icosahedral symmetry), with the result that the structure is self-similar--i.e. the structure will be mapped into itself if the structural length scale is multiplied by an appropriate constant.

Though the evidence of an AlMn structure exhibiting quasicrystalline properties was reported in 1984, the mathematical theory of quasiperiodic structures was developed much earlier [2]. As early as 1902 the notion of quasiperiodic functions had been introduced by mathematicians, by 1936 incommensurate modulated structures--i.e. stable structures with atomic positions displaced from the crystal lattice with a periodicity incommensurate with the spatial periodicity of the lattice they decorate-- had been discovered , and by the mid- to late-1930's theoretical descriptions of quasiperiodic functions in terms of periodic functions in higher dimensional spaces had been developed by H. Bohr (brother of Niels Bohr) and H. Cohn [3]. The quasicrystalline space groups were formulated before 1980, and in 1984 D. Levine and P. J. Steinhardt published a study of an idealized atomic structure that was

quasiperiodic rather than periodic, and which had crystallographically forbidden symmetries. The year 1984 therefore marked the intersection of theoretical descriptions of noncrystalline solids with the experimental evidence for the existence of quasicrystals [2].

As the materials exhibiting quasicrystalline properties have improved, various models have been developed to describe their structure. The first quasicrystals in AlMn were not thermodynamically stable -- they transformed to crystalline structures upon annealing --and their diffraction peaks showed broadening that indicated disorder. For this reason, P. W. Stephens and A. I. Goldman proposed a structural model of AlMn as icosahedral glasses, in which icosahedral clusters were randomly stacked according to certain rules. In the same year, 1986, that Stephens and Goldman published their paper, the first thermodynamically stable quasicrystal was obtained in the AlCuLi alloy system. Though the icosahedral glass model worked well in the case of AlMn, the diffraction peak widths of AlCuLi did not scale as the icosahedral glass model predicted, making room for the another model which explained the linewidths by assuming that strains were quenched during the rapid solidification from the melt. Then in 1988 the first "perfect" quasicrystals were reported in the AlCuFe system, followed shortly by the AlCuRu quasicrystals, and then in 1990 by AlPdMn. These quasicrystals were perfect from the experimental standpoint in that they were both thermodynamically stable and did not exhibit any evidence of disorder through broadening of the diffraction peaks, therefore making their diffraction peak widths limited only by the resolution of the instrument. The structure of these highly ordered "perfect" quasicrystals can be described most simply in 6 dimensional space hyperspace, as is discussed in Chaper 2, which provides much of the terminology and physical concepts for the study of quasicrystals.

Though the six dimensional hyperspace model may explain many features of the quasilattice, the three dimensional decoration of the lattice with atoms is an elusive problem that has not been solved. This is one of the most intriguing aspects of the stable

quasicrystals: despite their high degree of long-range order, the chemical ordering of atoms on the quasilattice is uncertain, as is the distribution of local atomic environments.

B. NMR/NQR: Electronic and Structural Properties

It is important to note that the structural and electronic properties of quasicrystals are linked, and that understanding one is key to understanding the other. The high degree of symmetry of icosahedral quasicrystals makes the "pseudo-Brillouin zone"--the Wigner-Seitz cell in reciprocal space based upon the most intense diffraction peaks--nearly spherical. This fact, combined with the evidence that quasicrystalline structures tend to be most stable when the Fermi surface makes contact with the pseudo-Brillouin (Hume-Rothery condition), leads one to expect a drastic reduction in the density of states at the Fermi level from the free electron value, called a pseudogap. In addition, there has been a great deal of speculation concerning the existence of fine structure in the density of states, vis. oscillations that occur on a scale less than 0.02 eV.

Nuclear magnetic resonance techniques are well suited for investigating both the local environments of the resonant nuclei, and the electronic structure near the Fermi surface. Nuclear magnetic resonance (NMR) and nuclear quadrupole resonance (NQR) have been used since their discovery in the 1940's to study the physics of gases, liquids, and solids, and have yielded not only fundamental quantitative information about the nuclei of atoms but also new insights into the structure and dynamics of many substances. These nuclear resonance techniques have been applied with great success to the study of many solids, because by studying nuclear resonance spectra one may obtain information about the distribution of electric field gradients and magnetic fields at the nuclear sites. For this reason, nuclear resonance techniques allow one to probe the effect of the local environments around the resonant nucleus on the nuclear energy levels, out to the first few nearest neighbors. This information is contained in the characteristics of the nuclear resonance spectra, such as line

position, width, shape, and relative intensity. In metallic systems, the shift of the nuclear resonance from that of a free nucleus in solution is called the Knight shift, and its magnitude gives information about the density of states at the Fermi energy. Similar information may also be obtained from the nuclear spin-lattice relaxation time T_1, which is the time it takes for the excited nucleus to give its energy to the lattice. In many cases, T_1 is more sensitive to changes in electronic structure than the Knight shift.

Though NMR has not been as extensively applied to the study of quasicrystals as have scattering techniques, NMR studies have been reported by several groups [4 - 15], including studies by Hippert et al. [12], Drews et al [9], and Hill et al. [15] in the stable icosahedral quasicrystals of AlCuFe and AlCuRu. These studies may be classified under two broad categories: those that investigate the local environments of the resonant nuclei [4 - 10], and those that probe the electronic states near the Fermi surface [5 - 7, 9 - 13]. However, considerable variations exist in the interpretation of the distributions of local environments through the NMR spectra, as well as the Knight shift and nuclear relaxation data, leading to widely different measurements in these quantities. Therefore, a careful NMR/NQR investigation is warranted to attempt to obtain accurate Knight shift and relaxation time values, and to determine the nature of the distribution of local environments.

C. Overview of Contents

In the chapters that follow, we present the methods and results of an investigation into both aspects, structural and electronic, of the stable quasicrystals AlCuFe, AlCuRu, and AlPdMn.

Chapter 2 presents the definition of quasicrystallinity, as well as a description of the perfect quasicrystals in hyperspace. Then the pseudo-Brillouin zone will be defined, and the effect of its symmetry on the electronic properties will be explained. The electronic and

transport properties of linear coefficient of the specific heat, γ, thermopower S, Hall coefficient R_H, and conductivity σ, will be discussed in AlCuFe and AlCuRu alloys.

Chapter 3 discusses the theoretical aspects of NMR and NQR experiments, and lays the ground work for the data analysis of the NMR spectra (see also Appendix 1), and the nuclear spin-lattice relaxation times.

Chapter 4 discusses sample preparation methods, and the apparatus involved in each experiment, particularly the field scanning experiments, the medium-range pressure experiment, and the NQR experiment.

Chapter 5 includes NMR and NQR investigations into the distributions of local environments in AlCuFe icosahedral and approximant phases, AlCuRu samples, and a single grain AlPdMn icosahedral quasicrystal. The focus is to determine the distribution of local electric field gradient tensors through both ^{27}Al NMR and NQR, and to analyze data through simulations of the NMR and NQR resonance lines. We found a broad, continuous distribution of electric field gradient (EFG) tensor components at the aluminum sites in AlCuRu and AlCuFe quasicrystals, which may be explained based on a simple EFG model calculation. The distribution of EFG gradients was corroborated by aluminum NMR in a single grain AlPdMn quasicrystal. In addition, a large fraction of the copper nuclei may sit, on the average, at sites of higher symmetry than the aluminum nuclei..

Chapter 6 discusses NMR experiments that probe the pseudogap in quasicrystals and their approximants. The values of Knight shift and spin-lattice relaxation time were obtained, corrections being included for distributions of quadrupole interactions that exist in these materials. It will be shown that a simple s-band model accounts for the values of Knight shift and relaxation time, and therefore that these quantities are directly related to the density of states at the Fermi energy. In AlCuRu, a study of NMR parameters with composition, a medium range pressure study of ^{27}Al Knight shift and ^{65}Cu spin-lattice relaxation time, and

preliminary high temperature ^{27}Al NMR data, will be discussed in the light of pseudogap fine structure. Neither the compositional study, nor medium-range pressure study, yield evidence in support of proposed pseudogap fine structure on a scale less than 0.02 eV. In addition, AlCuFe NMR parameters will be compared for the quasicrystal and its approximant, and the effects of long range order in determining electronic properties discussed.

Chapter 7 includes the summary and conclusions.

CHAPTER 2. QUASICRYSTALS: GENERAL PROPERTIES

In this chapter we present the hyperspace model of quasicrystals, and discuss the importance of the pseudo-Brillouin zone in determining the electronic properties and transport properties of quasicrystals. We also discuss structural properties of AlCuFe, AlCuRu, and AlPdMn, and review experiments designed to detect the fine structure in the pseudogaps of various quasicrystals.

A. Quasilattices and Hyperspace

Lattice periodicity is not necessary for a solid to have long range positional order. This fact was highlighted in the early 1930's when incommensurate crystals were discovered. These systems can be described as the result of two interpenetrating crystalline lattices whose lattice constants are incommensurate with each other. Therefore, the spatial periods of the two sublattices are related by an irrational number, and the overall lattice is not periodic. Since the two sublattices are periodic, however, one finds that these systems exhibit sharp diffraction peaks, though the diffraction peaks are not equally spaced in reciprocal space as they are for a crystalline system [2].

What distinguishes quasicrystals from crystals, incommensurate crystals in particular, is that quasicrystals have non-crystallographic point symmetries. There are exactly 14 types of three dimensional crystalline lattices, the Bravais lattices, whose symmetries therefore comprise all the symmetries seen in ordinary crystals [16]. In theses crystalline lattices, there are no 5-, 8-, or 12-fold axes, and for this reason such symmetries are termed "non-crystallographic symmetries." Quasicrystals, by definition, have long-range order but non-crystallographic orientational symmetries, the most famous of which is icosahedral symmetry, as is found in the perfect quasicrystals of AlCuFe, AlCuRu, and AlPdMn.

Because quasicrystals are not periodic--they do not have a unit cell--the mass density function in space is not a periodic function. However, mathematically it is possible to

describe any aperiodic function as a periodic function in a higher dimensional space. For a quasicrystal, six dimensions are required, meaning that the primitive reciprocal space vectors are six in number, with the result that there are six indices for the labeling of diffraction peaks. One choice for these primitive vectors is shown in Fig. 2.1, and is called the "umbrella convention" described by Elser [17]. In this convention, the magnitude of the reciprocal lattice vector that corresponds to the (100000) diffraction peak is given by π/a, where a is the quasilattice constant equal to the edge length of the tiles used to generate the quasilattice [18].

The idea that a quasilattice may be described periodically in six-dimensional space means that atomic three-dimensional quasilattices may be obtained by slicing through the six-dimensional hyperspace. Fig. 2.2 illustrates this for a one dimensional model of a quasicrystal. . The atomic position are determined by the intersection of the line segment through each lattice point, called the atomic surface, with the diagonal solid line used to represent physical space. In order for the atomic arrangement to be aperiodic, the slope of the physical space line must be incommensurate with the "planes" of the two-dimensional lattice. The result is a sequence of two kinds of segments, one short and one long, occurring without any repeating pattern or "unit cell," as has been shown by Katz and Duneau [19]. Periodic arrangements will occur, however, when the slopes between physical space and the hyperspace planes are commensurate. These periodic structures are called approximants, because in physical space their local atomic environments become more and more like those of the quasicrystal as their lattice parameters inflate indefinitely. For three-dimensional icosahedral quasicrystals, there exist a series of approximants with cubic symmetry, and the degree to which their local environments approximate that of the icosahedral quasicrystals is called the order of the approximant. The order is designated by the ratios 1/0, 1/1, 2/1, 3/2,

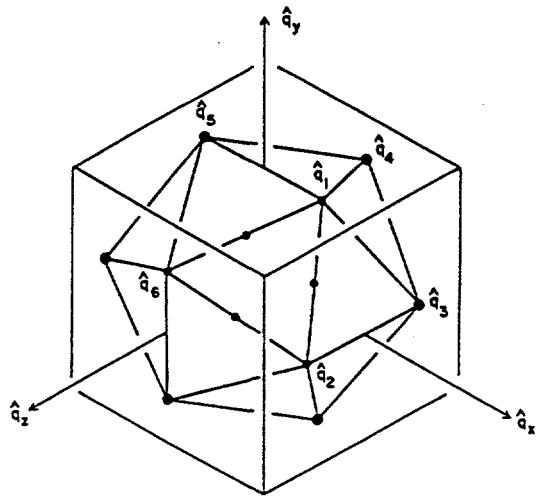

Fig. 2.1. The six reciprocal lattice vectors that form the basis in reciprocal space for icosahedral quasicrystals. Taken from Goldman and Widom, ref. [20].

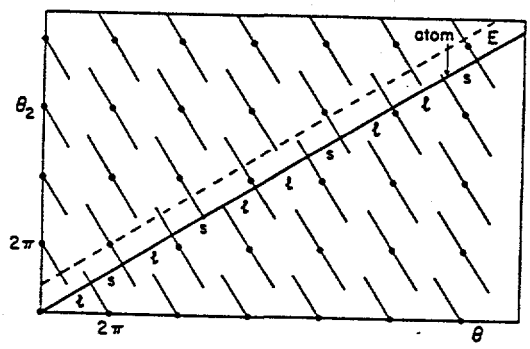

Fig. 2.2 Hyperspace model of a one dimensional quasicrystal. Figure illustrates how a periodic lattice in a higher dimensional space may be used to generate a quasicrystal in a lower dimensional space. See text for details. (Taken from Goldman and Widom, ref. [20]).

5/3, ..., which converge to the golden ratio $\tau = (1 + \sqrt{5})/2 = 1.618...$ Each successive term corresponds to a structure

having a lattice parameter inflated by τ relative to the one before it. The volumes, and therefore the number of atoms in the unit cell, consequently scale as $\tau^3 \approx 4$.

It is interesting to note from Fig. 2.2 that if the chain were periodic, an infinite number of sites would have the same global environment of surrounding atoms. In the quasiperiodic case, no two atoms have the same global environment, though there are an infinite number of sites with the same local environment out to any finite distance d [19]. This is called self-similarity, and shows up in both the real space and the reciprocal space structure of quasicrystals.

The quasilattice may also be described in terms of tilings, i.e. subunits that fit together to fill all space and which result in global icosahedral symmetry. One of the most famous such tilings is the Penrose tiling, consisting in three-dimensions of two rhombohedra, one fat and one thin. The tiling picture has been very useful in the study of the structural stability of quasicrystals [3].

It should be emphasized that though the quasilattices may be described by the above models, the chemical ordering and the atomic positions are still very much in question, since periodicity in a higher dimensional space does not translate to a tiling in three dimensions [2], and consequent knowledge of atomic positions. Therefore the study of local environments in quasicrystals is very important to understanding how, on the atomic level, quasicrystals are built.

B. Structural Properties: AlCuFe, AlCuRu, AlPdMn

The structures of AlCuFe, AlCuRu, and AlPdMn have been characterized by studies of their long-range order, through high resolution electron microscopy, x-ray diffraction, and electron diffraction [2]. AlCuFe many be formed in two phases: a perfect icosahedral

quasicrystal, and a 3/2 rhombohedral approximant [21]. The icosahedral phase has x-ray diffraction peaks that are limited only by the resolution of the spectrometer, and additional studies using a synchrotron high resolution powder diffractometer have shown no significant broadening of the lines [2]. The quasilattice constant of $Al_{65}Cu_{20}Fe_{15}$ is a = 4.45 Å [2]. The approximant has a rhombohedral unit cell with lattice parameter a = 18.86 Å and $\alpha = 63.43$ ° [2]. AlCuRu is known to form icosahedral phases over a broader range of compositions than AlCuFe, as demonstrated by Shield et al. [22]. The stoichiometries $Al_{85-x}Cu_xRu_{15}$ x=15, 17, 20 are of particular interest, since the relatively small difference in composition between samples, combined with the constancy of the Ru concentration, make these alloys attractive in the study of electronic properties of perfect icosahedral quasicrystals. The quasilattice constant of $Al_{65}Cu_{20}Ru_{15}$ is 4.53 Å [2], and the extent of long-range order in both AlCuFe and AlCuRu alloys, inferred from the diffraction peak widths, exceeds 1 μm [23]. AlPdMn shows even more dramatic long-range order, and Kycia et al. have shown that large, single grain samples ≈ 1 cm length scales show positional order over length scales of 10 μm [24]. Such large, nearly perfect quasicrystalline single grains make possible for the first time NMR studies of single grain quasicrystals, unfeasible in AlCuFe alloys due to the small single grains (≈ 100 μm scale) that form.

Techniques that probe short-range order such as x-ray absorption fine structure (EXAFS), Mössbauer effect, and NMR have been applied to the perfect icosahedral phases, but to a lesser extent than coherent scattering techniques. NQR, which is 10 - 100 times less sensitive than NMR, has not been reported in any quasicrystalline system prior to this investigation. The results of such local environment studies are quantitative characterizations of average local environments surrounding a particular species of atom. Sadoc and Dubois reported average nearest-neighbor distances in $Al_{71}Pd_{19}Mn_{10}$ obtained through EXAFS that give average nearest-neighbor bond lengths of 2.50 Å, 2.60 Å, and 2.80 Å respectively for

Al-Mn, Al-Pd, and Al-Al bond lengths [25]. Hu et al. used EXAFS data obtained from $Al_{65}Cu_{20}Ru_{15}$ to refine a structural model, but reported difficulty in obtaining information on the Al pair density functions due to the low energy of the Al K edge [26]. ^{27}Al NMR has been reported in several metastable [4 , 5, 8] and stable quasicrystals [12], [9], [10], [15]. Warren [4] and Drews [9] argue that NMR shows a distribution of local electric field gradients (EFG), and hence local environments, but characterization of the distribution is uncertain

C. Electronic and Transport Properties of AlCuFe and AlCuRu

Once the concept of quasicrystalline structure has been accepted, it is logical to turn to a study of the electronic properties to determine what, if any, differences exist between properties of quasicrystals and those of crystalline and amorphous phases. Such studies have been extensively reviewed by Poon [18], a prime focus being to determine whether the high degree of global symmetry in icosahedral phases will result in unusual electronic properties.

That something interesting might occur is suggested on an intuitive level when one considers scattering in a crystal.

Two regions of reciprocal space are fundamental to understanding electronic properties in crystals. The Brillouin zone is defined in a crystal as the Wigner-Seitz cell in reciprocal space. By definition, it is constructed by bisecting with planes the segments joining nearest-neighbor reciprocal space lattice points, the zone then being formed by the boundaries of the intersecting planes. The Fermi surface, by definition, divides the occupied electronic orbitals from the unoccupied ones at absolute zero, and is nearly spherical in most metals and alloys [18].The importance of the Brillouin zone is its relationship to Bragg's law of scattering, which may be stated that any particle with a wave vector that begins at the origin of the zone and ends at the surface of the zone will be Bragg reflected, and therefore will not freely

propagate through the crystal [18]. Therefore, if the Fermi surface, with radius k_F, touches the Brillouin zone, one has

$$k_F = \frac{|G|}{2}$$

where **G** is a reciprocal space lattice vector, and electrons at the intersection will be reflected and therefore no longer free. Since electrons within $k_B T$ of the Fermi surface are the ones that determine the electronic behavior of the material, the Fermi surface-Brillouin zone interaction is important in determining electronic characteristics.

Quasicrystals require an extension of the Brillouin zone concept, since they are not periodic, and their reciprocal spaces are densely filled with points of varying intensities. One defines the "pseudo-Brillouin" zone in quasicrystals as the zone constructed from the perpendicular bisecting planes for the reciprocal lattice vectors associated with the most intense scattering peaks [18]. For icosahedral quasicrystals, these zones are highly symmetric, as shown in Fig. 2.3.

In icosahedral quasicrystals, therefore, if the nearly spherical Fermi surface were to make contact with the highly symmetric pseudo-Brillouin zone, the high degree of overlap of the two, relative to what is usually found in crystalline systems, should result in drastic reduction of the electronic states near the Fermi surface called a "pseudogap." In fact, Bancel and Heiney [27], based on a survey of aluminum-based, icosahedral alloys, suggested that icosahedral phases are structurally stabilized when $k_F = |G|/2$, which is a rule that applies to many simple metals, and is known as the Hume-Rothery rule. If the Fermi energy lies near the minimum of the pseudogap, Vaks et al. have shown that the energy of icosahedral phase formation is competitive with that of crystalline phases [28].

Another possible effect, arising from the multitude of weaker reflections in reciprocal space, is a rapid oscillation in the electronic density within the pseudogap, called pseudogap fine structure. Calculations by Fujiwara [29] in the approximant phase of AlCuLi have lent

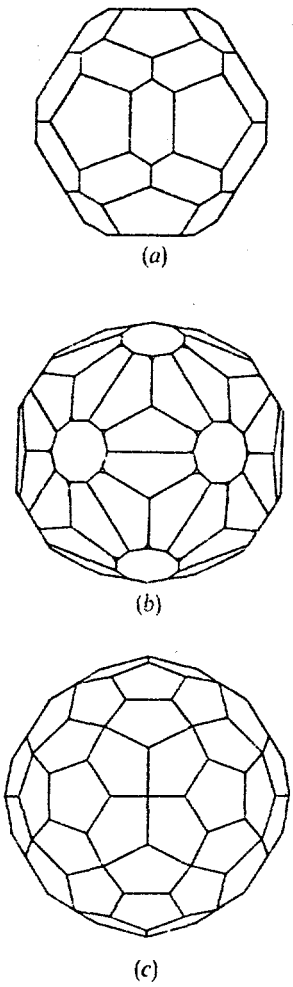

Fig. 2.3 Pseudo-Brillouin zones constructed as described in the text: (a) The zone for face-centred icosahedral alloys such as AlCuFe and AlCuRu alloys, constructed from the [422222] and the [4422002] planes; (b), (c) Zones for simple icosahedral alloys AlCuMg and GaZnMg. Taken from [18].

support to this idea, as Fig. 2.4 shows. Attempts to find experimental evidence of this effect have been extensively discussed by Poon [18], and have been attempted in both metastable and stable icosahedral phase alloys. The metastable phases of GaZnMg and AlCuMg form icosahedral phases over a wide compositional range, and consist of simple metals, allowing analysis of the data in terms of a free electron model. As the composition of the alloy is changed, the radius of the Fermi sphere changes according to $k_F \propto n^{1/3}$, where n is the number of electrons per unit volume. Wagner et al. [30] argue that compositional studies of properties sensitive to the density of states at the Fermi energy can probe structure in the DOS on an energy scale of 10^{-2} eV, as opposed to a resolution of 0.25 eV for soft x-ray photoemission [30]. Wagner et al. reported anomalies in thermopower, specific heat, and Hall coefficient measurements at approximately the critical electron per atom ratios, Z_C, calculated by Vaks et al. for a nearly free electron model, as well as non-monotonic behavior in the specific heat data (Fig. 2.5). The interpretation of these effects as due to pseudogap fine structure is clouded by the fact that in metastable systems, the presence of strains and defects, which widen the x-ray diffraction peaks, also washes out the pseudo-Brillouin zone boundary, thereby reducing the effects of the zone on electronic properties. Based on the wide x-ray diffraction peaks of AlCuMg, therefore, Poon points out that one would expect the pseudogap fine structure to be spread out over nearly one half the compositional range studied, much wider than the oscillations detected (see Fig. 2.5).

The need for a study in the perfect icosahedral phases therefore becomes apparent, and the best candidate at this time is the AlCuRu system.

Transport properties in the $Al_{85-x}Cu_xRu_{15}$ system have been extensively measured, but the NMR parameters have not. Biggs et al. [31] report the γ values 0.11, 0.23, and 0.2 mJ/g-at K^2 for x=20, 17, 15 respectively (Fig. 2.6 (a)), which they compare with the free electron

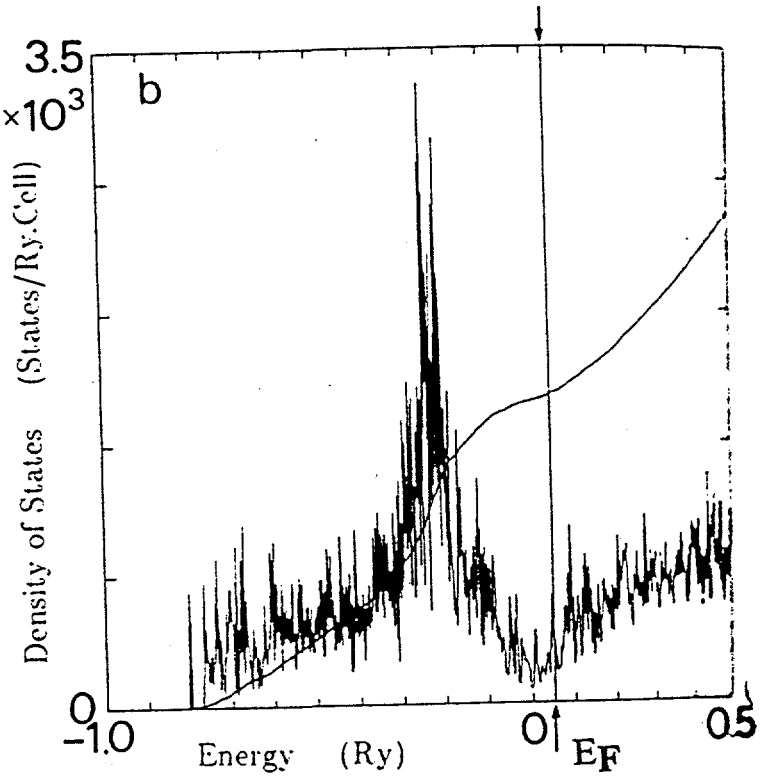

Fig. 2.4 Pseudogap fine structure. Calculations by Fujiwara et al. in the AlCuLi approximant show fine structure in the pseudogap. Taken from [29].

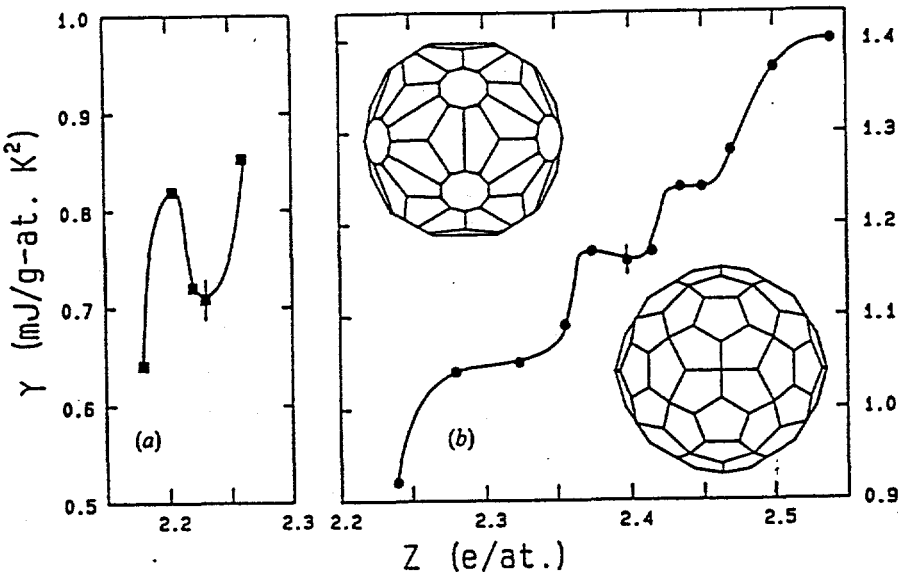

Fig. 2.5 The linear coefficient γ of the specific heat for metastable icosahedral quasicrystals GaZnMg (left graph) and AlCuMg (right graph). Each point corresponds to a different sample stoichiometry, and the electron per atom concentration Z is calculated based on a nearly free electron model. Solid lines are guides for the eye. Taken from Wagner et al. 1990 ref. [30].

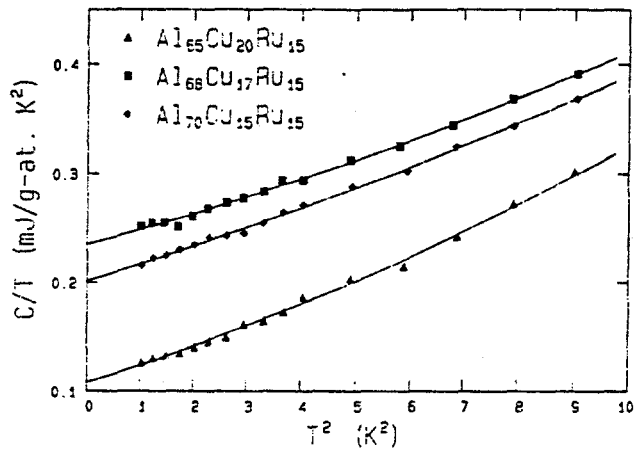

(a)

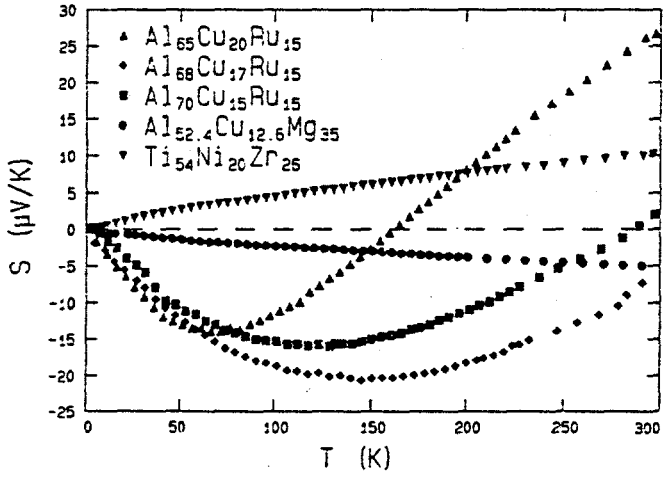

(b)

Fig. 2.6 Specific heat and thermopower data for the perfect icosahedral quasicrystals of AlCuRu. (a) γ values are obtained from the y-axis intercepts, and show considerable variation; (b) thermopower shows change sign in AlCuRu alloys; metastable icosahedral phases of TiNiZr and AlCuMg exhibit metallic glass behavior and are included for comparison. Taken from Biggs et al. ref. [31].

value of 1.1. In addition, they report marginally metallic room temperature conductivities of $\sigma(295\ K) \approx 200\ \Omega^{-1}cm^{-1}$. Based on magnetoresistivity measurements, Biggs et al. report a short electron mean free path l given by $k_F l \approx 0.3$, and through Hall effect measurements have found that $n = 2.4 \times 10^{20}$, 5×10^{20} cm^{-3} for the x = 20, and x =15, 17 samples respectively. They also report an unusual temperature dependence for the Hall coefficients and thermopowers (Fig. 2.6(b)), noting that no theories for the regime $k_F l < 1$ are currently available for comparison.

Biggs et al. suggest that the rapid changes in γ, and the sign change of S, may be indications of pseudogap fine structure. The factor of 2 change in γ, which in the free electron picture is related to the DOS by $\gamma \propto D(E_F)$, Biggs suggests, may be a manifestation of the rapid oscillations predicted. In addition, the change in sign of the thermopower, defined as the coefficient of proportionality between the temperature gradient in a material and the electric field that results from it (Seeback effect), may be qualitatively explained by taking a result from the theory of non-crystalline solids [32]

$$S \propto \frac{1}{\sigma(T)} \int \left(\frac{E - E_F}{k_B T} \right) \frac{\partial f}{\partial E} \sigma_E dE$$

where $\sigma(T)$ is the conductivity at temperature T, σ_E is related to $D(E_F)$, and f is the Fermi function. Poon [18] argues that the qualitative behavior of S in Fig. 2.6 (b) may be understood through the above equation, the integrand of which is an odd function about the Fermi energy E_F of width $k_B T$. If $D(E_F)$ varies slowly with respect to $k_B(300\ K) \approx 0.02$ eV no sign change will occur as T decreases, but if $D(E_F)$ changes rapidly compared with 0.02 eV, a sign change might be expected, as seen in Fig. 2.6 (b). Poon therefore argues the thermopower may be understood in the light of pseudogap fine structure on a scale less than 0.02 eV.

The AlCuFe system presents the opportunity for studying the effects of long-range order versus intermediate-range order in determining electronic properties, since it can be prepared

in the icosahedral phase, crystalline approximant phase, and amorphous phase [18]. The electronic transport properties of these materials have been investigated extensively by Wagner et al [30]. They report room temperature conductivity values for the icosahedral, crystalline, and amorphous phases which are respectively 380, 400, and 1,400 $\Omega^{-1}cm^{-1}$. Specific heat measurements yield $\gamma = 0.31$ and 0.29 mJ/g-at K^2 for the icosahedral and crystalline phases respectively, with corresponding Debye temperatures being 539 and 583 K. Temperature dependence of thermopower and Hall coefficient are similar to those of the AlCuRu system. In addition, carrier concentrations determined from the Hall coefficient are lower in the icosahedral and crystalline phases than in the amorphous phase. There is great similarity in the transport properties of the icosahedral and crystalline phases. The crystalline phase is a 3/2 approximant with $\approx$ 1,400 atoms in its unit cell, and the similarity of transport properties is consistent with theoretical work [33], [29] indicating a deepening of the pseudogap as the order of the approximate increases.

CHAPTER 3
NUCLEAR MAGNETIC RESONANCE: GENERAL DISCUSSION

In this chapter we discuss static and dynamic aspects of the theory of nuclear magnetic resonance (NMR) as will be applied to the study of AlCuFe, AlCuRu, and AlPdMn quasicrystals. The term "static" refers to the time independent interactions between the nuclei and the lattice that yield the nuclear energy levels, and therefore the NMR spectra; "dynamic" refers to the time dependent interactions that stimulate nuclear transitions and lead to relaxation of the nuclear levels from an excited state.

A. Physical Pictures of NMR Processes

There are two ways of viewing nuclear magnetic resonance: in terms of transitions between discrete energy levels, which stems from the work of E. M. Purcell; and as a rotation of the net nuclear magnetic moment, which comes from the research of F. Bloch [34]. In Purcell's picture, nuclear magnetic resonance is viewed as stimulated transitions by oscillating radio frequency (RF) fields between nuclear energy levels created by a static magnetic field $\mathbf{H_0}$. In Boch's picture, the nuclear moments are viewed as classical moments precessing around $\mathbf{H_0}$, and nuclear magnetic resonance is seen as the rotation of the nuclear moments from the z'-axis down into the x'-y' plane when a perpendicular field--oscillating with frequency near the Larmor frequency of nuclear precession--is applied perpendicular to $\mathbf{H_0}$. The two pictures are equivalent, though each one has its conceptual strengths and weakness. From Bloch's semi-classical picture of NMR phenomena as rotating magnetic moments, one may readily understand what physical parameters enhance the sensitivity of the measurement, and so we focus first on this conceptualization.

Atomic nuclei carry a nuclear magnetic moment, usually on the order of $10^{-3} - 10^{-4}$ μ_B (Bohr magnetons), by virtue of possessing nuclear spin I. This nuclear moment is given by $\mu = \gamma\hbar\mathbf{I}$, where γ is the gyromagnetic ratio of the nucleus. When there is no external magnetic field the net magnetization of the sample is zero, since the nuclear spins have no

preferred direction. When a static field $\mathbf{H_0}$ is applied to N nuclei in a solid at constant uniform temperature T, the net magnetization is given by Curie's Law:

$$M = \frac{N\gamma^2\hbar^2 I(I+1)H_0}{3k_B T} \qquad (3.0)$$

This magnetization is oriented along the direction of the static magnetic field--defined here as the z'-axis. Since the system is assumed to be in thermal equilibrium, only the net magnetization along the z'-axis is non-zero. Because the detection coil can only detect the component of the net magnetization rotating in the x'-y' plane, no signal can be detected from the equilibrium state of the system. To measure the moment therefore, one must destroy the equilibrium.

This may be done with--among many other methods--a sequence of two RF pulses called a Hahn echo sequence. In Bloch's picture, the first pulse provides a magnetic field H_1 perpendicular to the z'-axis. The torque on the net moment from H_1 then rotates the net magnetization down toward the x'-y' plane. When the magnetization reaches the x'-y' plane the pulse is turned off, with the result that the magnetization is--in the laboratory frame--precessing and can therefore be detected by the pickup coil where it generates a voltage proportional to the net magnetization. Once in the x'-y' plane, the net magnetization decays as the individual nuclear moments--which see slighly different local magnetic fields--dephase with respect to one another. This signal is called the free induction decay (FID). The second pulse in the Hahn echo sequence becomes necessary if electrical ringdown after the pulse distorts the FID, or if the dephasing time is too short, making it difficult for the NMR receiver to acquire the complete FID.

The resulting signal is proportional to the net magnetization, and therefore proportional to the number of nuclei in resonance, the gyromagnetic ratio squared, and inversely proportional to the temperature. If the echo height is plotted versus the carrier frequency, the result is an NMR spectrum.

B. Magnetic Dipole Transition Spectra

In NMR and NQR experiments the axis of the detection coil is perpendicular to the axis of quantization of the nuclear levels. Therefore the oscillating field $\mathbf{H}_1 = \mathbf{H}_1 e^{i\omega t}$ may be chosen without loss of generality to be along the x'-axis of the lab frame. By Fermi's Golden Rule the transition rate is given by

$$W_{m,n} = \frac{2\pi}{\hbar}\left|\langle \mu \cdot \mathbf{H}_1 \rangle\right|^2 \propto \left|\langle m|I_+|n\rangle\right|^2 \tag{3.1}$$

Thuse allowed transitions occur for $\Delta m = \pm 1$ with intensity proportional to

$$\left|\langle m|I_+|m-1\rangle\right|^2 = I(I+1) - m(m-1) \tag{3.2}$$

In general, NMR and NQR spectra, denoted as $I(\nu)$, may be described in bulk samples as a collection of lines due to all the nuclear dipole transitions for every nucleus at resonance in the solid. This may be expressed as [35]

$$I(\nu) \propto \left(\frac{h\nu}{k_B T}\right)\sum\left|\langle m|I_+|m-1\rangle\right|^2 \tag{3.3}$$

where the summation is over all magnetic dipole transitions that occur at frequency ν. The prefactor includes the temperature T of the thermal reservoir, and comes from the Boltzmann distribution of the level populations at thermal equilibrium.

The area under the total spectrum may be obtained from the Kramers-Kronig relations since $I(\nu)$ is the imaginary part of a complex susceptibility $\chi(\omega) = \chi'(\omega) + i\chi''(\omega)$. The Kramers-Kronig relationship, which relates the real and imaginary components, gives for the case of narrow resonance lines [34 Slichter]

$$\int_0^\infty I(\nu)d\nu = \frac{\pi}{2}\chi_0\omega_0 \tag{3.4}$$

where

$$\chi_0 \equiv \frac{N\gamma^2\hbar^2 I(I+1)}{3k_B T} \tag{3.5}$$

$$\omega_0 \equiv \gamma H_0$$

C. Nuclear Properties

Of the stable isotopes in the quasicrystals we studied--^{27}Al, ^{63,65}Cu, Mn--the abundances of each isotope and the gyromagnetic ratio are given in Table 3.1. On the basis of abundance and gyromagnetic ratio, Al and Cu are the best candidates, along with Mn. In this study, which focusses primarily on AlCuFe and AlCuRu alloy systems, we perform NMR on Al and Cu nuclei, leaving the Mn in AlPdMn for later investigations.

At this point we note that ^{27}Al and ^{63,65}Cu all have a quadrupole moments which are, respectively, 0.140, -0.209, -0.195 in units of $e\cdot 10^{-24}$ cm^2 ($e=4.80\times10^{-10}$ (erg-cm)$^{1/2}$) [36]. In general a nucleus with spin I has a quadrupole moment when I>1/2. A nucleus in most chemical substances is surrounded by inner-shell electrons, valence-shell electrons, and various other atoms or ions. The electric charges on these particles produce an electric potential V at the position of the quadrupolar nucleus, and when this distribution has a symmetry less than cubic, the electric field gradients (EFG), $V_{ij} \equiv \partial^2 V / \partial x_i \partial x_j$, are non-zero. The effect that quadrupole interactions have on the spectra of AlCuFe and AlCuRu alloys is important, and therefore to understand powder and single grain NMR and NQR spectra of quadrupolar nuclei, we turn to a discussion of the Hamiltonians and energy levels.

D. Static Properties: Magnetic and Quadrupole Effects

The field of electric quadrupole interactions in magnetic resonance can be divided roughly into two areas according to the relative magnitude of the nuclear quadrupole interactions. In the first case, usually called the "low field" case, the nuclear quadrupole interaction dominates all other effects, and resonance experiments performed under these conditions will be referred to as "NQR" experiments. In NQR experiments the static external field has a magnitude anywhere from zero to at most a few hundred gauss. In the second case, usually called the "high field" case, the nuclear electric quadrupole interaction energy is assumed small compared to the interaction energy of the nuclear magnetic moment with the

Table 3.1 Nuclear abundance, gyromagnetic ratio, and nuclear spin for isotopes in the icosahedral quasicrystals of this study [36]

Nucleus	Abundance	$\gamma / 2\pi$	Nuclear spin
^{27}Al	100%	11.094	5/2
^{55}Mn	100%	10.501	5/2
^{63}Cu	69%	11.285	3/2
^{65}Cu	31%	12.090	3/2
^{105}Pd	22%	1.74	5/2
^{101}Ru	17%	2.10	5/2
^{99}Ru	13%	1.10	5/2
^{57}Fe	2%	1.376	1/2

external magnetic field $\mathbf{H_0}$. A resonance experiment performed under these conditions is what will be continually referred to here as simply an "NMR" experiment. The quadrupole effect manifests itself as a perturbation of the purely magnetic interactions, and the perturbations can split the resonance lines into several components. In addition to creating a fine structure in the resonance line, the quadrupole interactions may lead to a broadening or apparent loss of intensity of the resonance line.

In order to quantitatively discuss quadrupole effects in the spectra of powder and single grain quasicrystalline samples, one must turn to a discussion of the Hamiltonians and energy levels in the cases of NQR and NMR.

A discussion of the quantum mechanical quadrupole interaction Hamiltonian usually begins with a calculation in classical electrostatics applied to the nucleus [34]. From electrostatics one knows that to find the interaction energy of an arbitrary charge distribution $\rho(\mathbf{r})$ in a potential $V(\mathbf{r})$ due to external sources one must calculate

$$E = \int d^3r\, \rho(\mathbf{r}) V(\mathbf{r}) \tag{3.6}$$

As is well known, one may approximate this integral by performing a series expansion of $V(\mathbf{r})$ about the origin. What emerges as a result is an expansion of the energy E in terms of the derivatives of the external potential $V(\mathbf{r})$, and integrals over the charge distribution called the multipole moments. Choosing the origin as the center of mass of the nucleus, these terms represent energy contributions from different aspects of the geometry of the charge distribution. The first term is the electric monopole term, and represents the energy of the entire nuclear charge distribution taken as a point charge, an is therefore independent of the nuclear orientation. The second term is the electric dipole term, which goes to zero since center of mass and the center of charge coincide. The third term is the electric quadrupole term, and is dependent upon the orientation of the nucleus. One may write the quadrupole term as

$$E_Q = \frac{1}{6}\sum_{i,j} V_{ij} e Q_{ij} \tag{3.7}$$

where the components of the EFG tensor are given by

$$V_{ij} \equiv \left.\frac{\partial^2 V}{\partial x_i \partial x_j}\right|_{r=0} \tag{3.8}$$

and where $x_i \equiv x, y, z$, and the components of the quadrupole moment are

$$eQ_{ij} \equiv \int d^3r \left(3x_i x_j - \delta_{ij} r^2\right)\rho(\mathbf{r}) \tag{3.9}$$

Finally, one may note that because the potential $V(\mathbf{r})$ is due to external charges, Laplace's equation $\nabla^2 V = 0$ must hold, giving the relation

$$V_{xx} + V_{yy} + V_{zz} = 0 \tag{3.10}$$

Therefore the EFG tensor is traceless, i.e. the diagonal terms of the tensor sum to zero in every coordinate system.

1. Definition of Non-equivalent Sites

For a quadrupolar nucleus at a site of less than cubic symmetry there will be contributions to the electric field gradient from electronic and lattice charge distributions. The EFG tensor due to lattice contributions in the point charge approximation is [34 Slichter]

$$V_{ij} = \sum_k \frac{eZ_k}{r_k^3}\left(\frac{3x_i x_j}{r_k^2} - \delta_{ij}\right) \tag{3.11}$$

where $x_{i=1,2,3}$ are the x-, y-, and z-components of the displacement vector, of magnitude r_k, between the nucleus at which the EFG is to be calculated and the ions of the lattice with charge Z_k. When this tensor is diagonalized to yield the components in the principal axis system, the components are labeled V_{xx}, V_{yy}, V_{zz} according to the relation

$$|V_{zz}| \geq |V_{yy}| \geq |V_{xx}| \tag{3.12}$$

From Laplace's equation (eqn. (3.10)) only two of the components are independent, and the magnitudes of the components in the principal axis system are completely determined by V_{zz} and η, where

$$\eta \equiv \frac{V_{xx} - V_{yy}}{V_{zz}} \tag{3.13}$$

with $0 \leq \eta \leq 1$ by definition.

The term "non-equivalent site" refers to sites with different values of the tensor components V_{zz} and η. Since the contribution to the EFG from successive coordination shells varies slowly as 1/r, the values of V_{zz} and η depend on several coordination shells. Therefore the "local environment" includes significant contributions out to the sixth coordination shell.

2. Nuclear Quadrupole Resonance

i. NQR Hamiltonian

In the case of NQR, one may write the Hamiltonian most simply in the principal axis system of the electric field gradient tensor, denoted by unprimed letters. In this system, the Hamiltonian simplifies to [34 Slichter]

$$H_Q = \frac{h\nu_Q}{6}\left[\left(3I_z^2 - I^2\right) + \eta\left(I_x^2 - I_y^2\right)\right] \tag{3.14}$$

where I_x, I_y, and I_z are the components of the spin operator **I**, and where

$$\nu_Q = \frac{3eQV_{zz}}{2I(2I-1)h} \tag{3.15}$$

For the case of Al (I = 5/2) this becomes $\nu_Q = 3eQV_{zz} / 20h$. The quantity eQ is the nuclear quadrupole moment. The quantity eQV_{zz}/h is called the nuclear quadrupole coupling frequency, and both eQV_{zz}/h and η are characteristics of the nucleus in a specified environment, i.e. in a solid--such as a quasicrystal--they are directly related to the electric charge distribution in that particular material. If eQV_{zz}/h is large enough, i.e. larger than 1 MHz, one may apply pulse NQR techniques to determine eQV_{zz}/h and its distribution of values with high accuracy. When eQV_{zz}/h is small, i.e. smaller than 1 MHz, eQV_{zz}/h may be measured by means of the quadrupole effect on the NMR line in a high magnetic field.

ii. Energy Levels and Transitions: I = 5/2

The problem of analytically determining the energy levels of the Hamiltonian for a general value of the asymmetry parameter η is difficult, and no exact solution exists for nuclear spins other than I=1 and 3/2. For other integer and half-integer spins, one must either solve the secular equation for the eigenvalue problem $H_Q|\varphi\rangle = h\nu|\varphi\rangle$ numerically, or use perturbation theory to obtain the eigenvalues in the form of a series expansion in η when η is sufficiently small. For nuclear spin I = 5/2 one finds two allowed transition frequencies, one for the $\pm 3/2 \leftrightarrow \pm 1/2$ and one for the $\pm 5/2 \leftrightarrow \pm 3/2$ transition:

$$\begin{aligned} \pm 3/2 \leftrightarrow \pm 1/2 \qquad & \nu_1 = \nu_Q f(\eta) \\ \pm 5/2 \leftrightarrow \pm 3/2 \qquad & \nu_2 = 2\nu_Q g(\eta) \end{aligned} \tag{3.16}$$

where the functions $f(\eta)$ and $g(\eta)$ have been determined numerically [36] over the full range of η. These functions are plotted for reference in Fig. 3.1. There it can be seen that $g(\eta)$ varies by only 0.1 over the entire range $0 \le \eta \le 1$, but that $f(\eta)$ varies by 0.7. Therefore the $\pm 5/2 \leftrightarrow \pm 3/2$ is the less sensitive of the two transitions to changes in η.

For the case of axial symmetry, one may easily obtain the exact eigenvalues. For $\eta = 0$ the Hamiltonian becomes

$$H_Q = \frac{h\nu_Q}{6}\left(3I_z^2 - I^2\right) \tag{3.17}$$

which results in the energy eigenvalues

$$E_m = \frac{h\nu_Q}{6}\left(3m^2 - I(I+1)\right) \tag{3.18}$$

and the level spacings $\Delta E_m \equiv E_m - E_{m-1}$

$$\Delta E_m = h\nu_Q(m - 1/2) \tag{3.19}$$

giving transition frequencies ν_Q and $2\nu_Q$ for the $\pm 3/2 \leftrightarrow \pm 1/2$ and $\pm 5/2 \leftrightarrow \pm 3/2$ transitions respectively. The quantum number m belongs to the operator I_z in the EFG principal axis system. Therefore the case of axial symmetry highlights the fact that in NQR

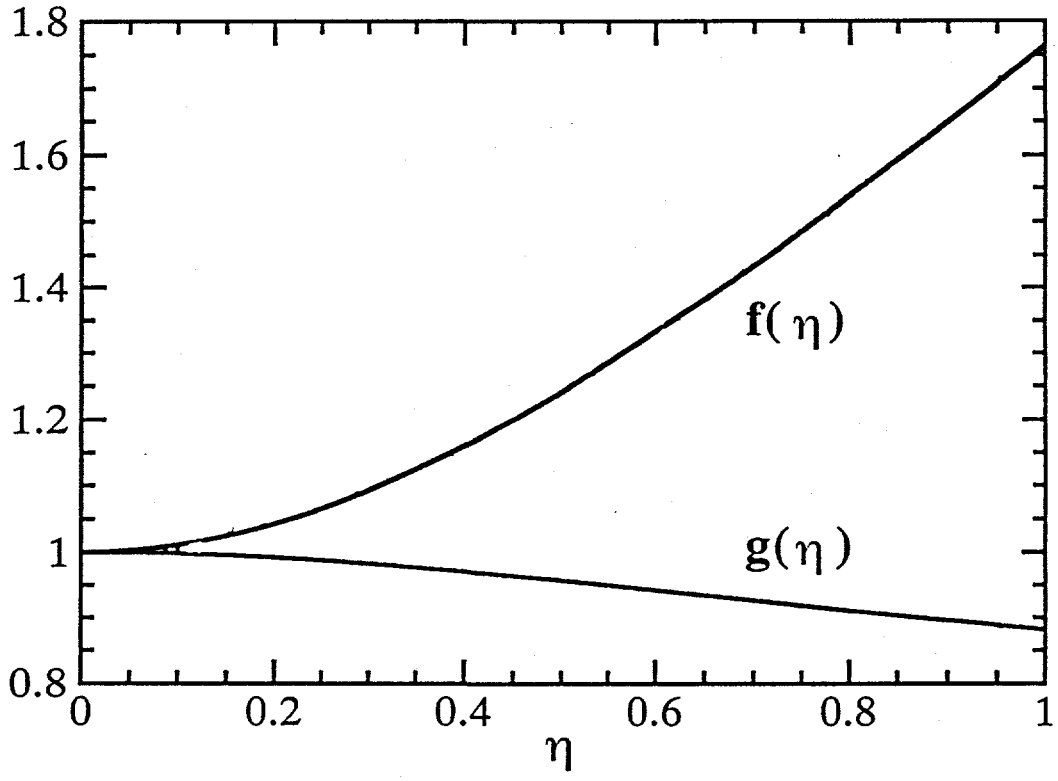

Fig. 3.1 The function f(η) and g(η) for the I = 5/2 NQR transitions ±3/2 ↔ ±1/2, and ±5/2 ↔ ±3/2 respectively. Graphs based on numerical data taken from [36]

experiments the z-component of the nuclear magnetization occurs along the z-axis of the EFG principal axis system. Since the EFG principal axis system depends on the symmetry of the local environment, the distribution of local environments results in a distribution of principal axis systems, and there is no one unique z-axis direction as there is in NMR. However, the application of a Hahn echo pulse sequence to nuclear quadrupole levels has the same effect as in NMR, which is to rotate the net magnetization vector that is perpendicular to the pulsed magnetic field H_1 down into the x-y plane, and then to rephase it with the second pulse.

iii. NQR Spectra and EFG Tensors

It will now be argued that the NQR lines give the distribution of electric field gradient tensor components. From eqn. (3.3) we have

$$I(\nu) \propto \frac{h\nu}{k_B T} \sum \left| \langle n | I_+ | n-1 \rangle \right|^2 \qquad (3.3)$$

By taking an NQR spectrum over the $\pm 5/2 \leftrightarrow \pm 3/2$ transition for I = 5/2, for example, the sum in Eqn. (3.3) becomes

$$I(\nu) \propto \frac{h\nu}{k_B T} \sum_{\Delta E = h\nu} \left| \left\langle \tfrac{5}{2} \right| I_x \left| \tfrac{3}{2} \right\rangle \right|^2 = \frac{h\nu}{k_B T} \left| \left\langle \tfrac{5}{2} \right| I_x \left| \tfrac{3}{2} \right\rangle \right|^2 \rho(\nu) \qquad (3.20)$$

Therefore, by dividing the experimental NQR spectrum by ν one gets a curve proportional to the distribution of transition frequencies $\rho(\nu)$. The transition frequencies satisfy $\nu = 2\nu_Q g(\eta)$ where, as seen in Fig. 3.1 and therefore

$$I(\nu)/\nu \propto \rho(\eta, V_{zz}) \qquad (3.21)$$

3. Nuclear Magnetic Resonance

i. NMR Hamiltonian

The NMR Hamiltonian in the case of quadrupole interactions is more complicated than the NQR Hamiltonian, because the static field $\mathbf{H_0}$ polarizes unpaired electrons in the conduction band, enhancing the dipole-dipole interaction between the nuclear and electronic moments [34 Slichter]. This introduces an additional term into the Hamiltonian that depends on a quantity called the Knight shift tensor K. The static field also induces electronic current densities resulting in magnetic fields that couple to the nucleus through a quantity called the chemical shift tensor σ, but a literature review of ^{27}Al chemical shifts in Cu environments indicates that the chemical shifts are 3-8 times smaller than the Knight shifts in AlCuFe and AlCuRu quasicrystals [37]. Therefore we drop the chemical shift from the formulas.

The NMR Hamiltonian therefore consists of interactions described by the Knight shift tensor and the EFG tensor. We assume that the local symmetry of the nucleus forces the principal axis systems of both tensors to be the same. This is reasonable since the principal axis system for an interaction tensor is determined by the symmetry of the local environment of the nuclear site. The common principal axis system of the Knight shift tensor and the EFG tensor will be referred to from now on as *the* principal axis system.

For quadrupolar nuclei in diamagnetic substances--such as ^{27}Al and ^{63,65}Cu in AlCuFe and AlCuRu quasicrystals--one may write the following NMR Hamiltonian [38]:

$$H = H_Z + H_M + H_Q \tag{3.22}$$

The Zeeman term H_Z--coming from the coupling of the nuclear moment to the static magnetic field-- is

$$H_Z \equiv -\gamma\hbar I_z H_0 \tag{3.23}$$

The magnetic term H_M is

$$H_M \equiv -\gamma\hbar I_z H_0 \left[K_{iso} + K_{an}\left(\frac{3\cos^2\theta - 1}{2}\right) + \varepsilon\frac{K_{an}}{2}\sin^2\theta\cos 2\phi \right] \tag{3.24}$$

where the Euler angles θ and ϕ determine the orientation of the magnetic field $\mathbf{H_0}$ in the principal axis system. The Knight shift tensor quantities may be defined in terms of the components of the tensor in the principal axis axis frame [39]:

$$K_{iso} \equiv \frac{1}{3}(K_{xx} + K_{yy} + K_{zz})$$

$$K_{an} \equiv K_{zz} - K_{iso} \tag{3.25}$$

$$\varepsilon \equiv \frac{K_{xx} - K_{yy}}{K_{an}}$$

. The quadrupole term, as seen before, is

$$H_Q \equiv \frac{h\nu_Q}{6}\left[\left(3I_z^2 - I^2\right) + \eta\left(I_x^2 - I_y^2\right)\right] \tag{3.26}$$

where I_x, I_y, I_z correspond to the components of the spin operator in the principal axis system. The transformation of the spin components from the principal axis frame to the lab frame is given by

$$\begin{aligned} I_x &= I_{x'}\cos\phi + I_{y'}\cos\theta\sin\phi + I_{z'}\sin\theta\sin\phi \\ I_y &= -I_{x'}\sin\phi + I_{y'}\cos\theta\cos\phi + I_{z'}\sin\theta\cos\phi \\ I_z &= -I_{y'}\sin\theta + I_{z'}\cos\theta \end{aligned} \tag{3.27}$$

Making this change of coordinate system will give the energy eigenvalues.

ii. Energy Levels and Transitions: I = 5/2

The eigenvalue problem may now be solved to first and second order assuming the magnetic and quadrupole interactions are perturbations on the Zeeman levels. Instead of writing the energy eigenvalues, however, we write the difference in energy between adjacent levels $E=E_m - E_{m-1}$. This gives [38]:

$$E = E_Z + E_M + E_Q \tag{3.28}$$

where

$$E_Z = h\nu_0 \equiv -\gamma\hbar H_0 \tag{3.29}$$

$$E_M = h\nu_0\left(K_{iso} + \frac{K_{an}}{2}(3\cos^2\theta - 1) - \frac{\varepsilon K_{an}}{2}\sin^2\theta\cos 2\phi\right) \tag{3.30}$$

and where the first and second order quadrupole contributions

$$E_Q = E_Q^{(1)} + E_Q^{(2)} \tag{3.31}$$

may be written as

$$E_Q^{(1)} = -\frac{h\nu_Q}{2}\left(m - \frac{1}{2}\right)\left(3\cos^2\theta - 1 - \eta\cos 2\phi\sin^2\theta\right) \tag{3.32}$$

$$E_Q^{(2)} \equiv \frac{\nu_Q^{\,2}}{12\nu_0}\left\{\frac{3}{2}\sin^2\theta[(A+B)\cos^2\theta - B] + \eta\cos 2\phi\sin^2\theta[(A+B)\cos^2\theta + B]\right.$$
$$\left. + \frac{\eta^2}{6}\left[A - (A+4B)\cos^2\theta - (A+B)\cos^2 2\phi(\cos^2\theta - 1)^2\right]\right\} \tag{3.33}$$

where A=24m(m-1)-4I(I+1)+9 and B=[6m(m-1)-2I(I+1)+3]/4.

These formulas are needed to write the NMR line shape simulation program discussed in Appendix 1. There the outline of the simulation program is discussed.

iii. NMR Spectra in Single Grains and Powders

An idealized single grain NMR spectrum is shown in Fig. 3.2. Since the NMR resonance condition for quadrupolar nuclei therefore becomes dependent upon the Euler angles of the static field $\mathbf{H_0}$ in the principal axis system, single crystal and powder samples will result in NMR spectra that are fundamentally different. The single crystal NMR spectrum will have 2I sharp resonance lines that change position as the crystalline axes are rotated with respect to $\mathbf{H_0}$.

For the case of a single crystal, one can simplify the Hamiltonian in order to understand the effect of the various interactions upon the energy levels. We will simplify the problem by assuming axial symmetry from which it follows that $\eta = \varepsilon = 0$. In addition, we will keep only first order terms. Instead of thinking in terms of the energy separation $E=E_m - E_{m-1}$ between two adjacent levels we will carry on the discussion in terms of the resonance frequency $\nu \equiv E/h$, given by

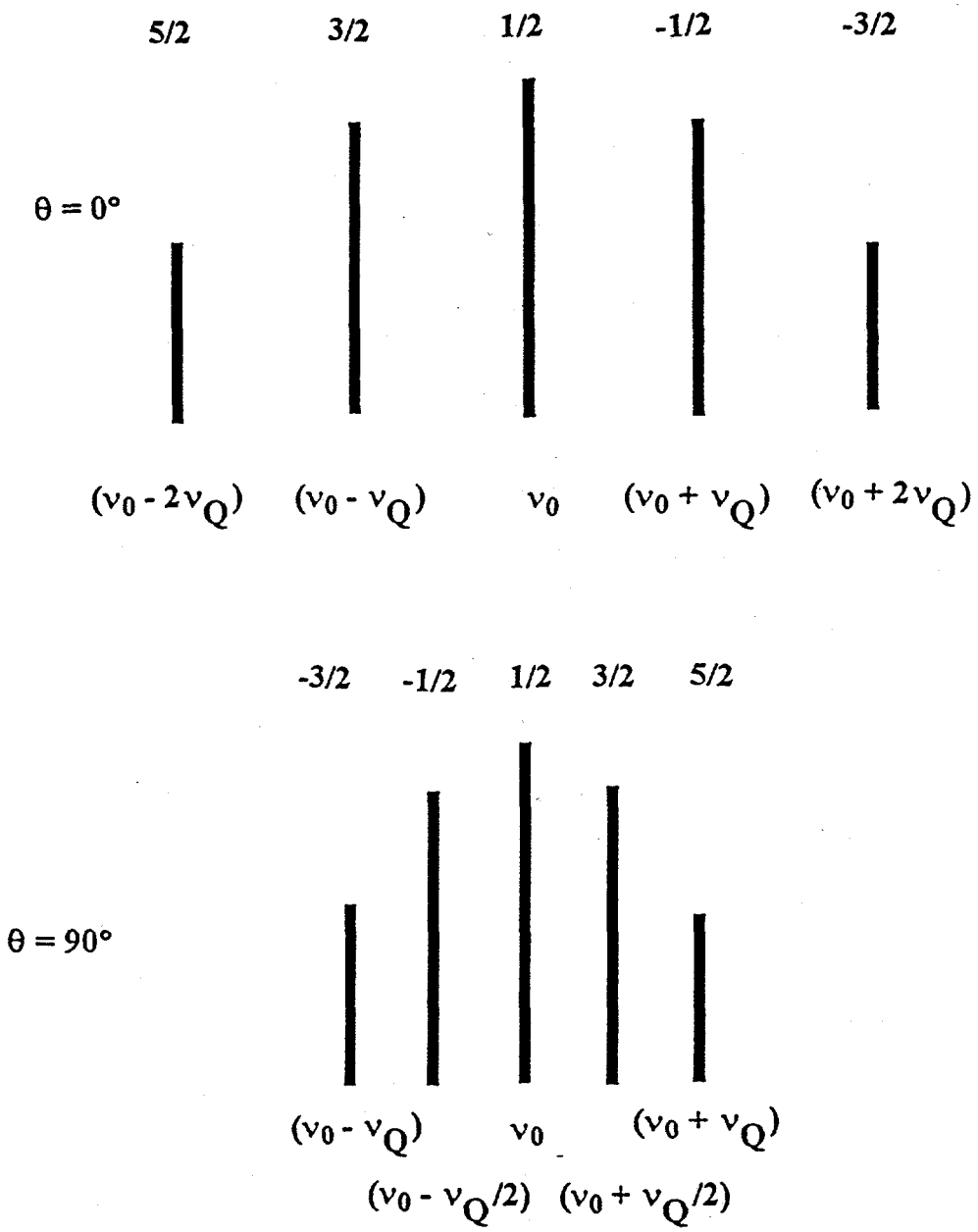

Fig. 3.2 Idealized single crystal NMR spectra and their angular dependence. Single grain spectra when $\theta = 0°$ and 90° for a quadrupolar nucleus of nuclear spin I = 5/2. The numbers, m, above the individual resonance lines indicate that the line arises from the $m \leftrightarrow m\text{-}1$ transition.

$$\nu = \nu_0\left(1 + K_{iso} + K_{an}\frac{(3\cos^2\theta - 1)}{2}\right) - \nu_Q\left(m - \frac{1}{2}\right)\frac{(3\cos^2\theta - 1)}{2} \qquad (3.34)$$

The first term is independent of m. If the Hamiltonian did not include quadrupole effects, all the resonance frequencies for m↔m-1 transitions would be the same. The m dependence occurs only in the quadrupole interaction, resulting in the $m \neq 1/2$ levels being shifted. Only the -1/2↔1/2 resonance frequency, called the central line, remains unshifted, all other levels being shifted in frequency either below ($m > 1/2$) or above ($m < 1/2$) the central line due to the quadrupole interaction. For this reason they are called quadrupole satellites. Eqn. (3.34) shows that the Knight shift interaction tensor shifts all transitions by the same amount. As is shown in Fig. 3.2 for a spin 5/2 nucleus in a single crystal oriented at $\theta = 0°$, one will have four satellite transitions located at $\pm\nu_Q$ and $\pm 2\nu_Q$ from the central line. As the orientation of the crystal is changed the satellite positions shift according to the angular term $\frac{3\cos^2\theta - 1}{2}$, and therefore the angular dependence of the NMR spectrum may be used to determine the principal axis system for a single crystal.

For a powder, all orientations of the principal axis system are present. However, as mentioned before, more grains are perpendicular to the static field than are parallel to it. The preference for $\theta = 90°$ results in singularities in the resulting spectrum, called a powder pattern. One such pattern is shown in Fig. 3.3 for I = 5/2. There is no angular dependence of the spectrum, and therefore one cannot obtain the orientation of the principal axis system. However, one may obtain the parameters ν_Q and η from the NMR powder pattern. If the quadrupole interaction is strong, it will determine the width of the central line as well as the breadth of the satellite background. For the satellites, the width of the line is given by [39]

$$\Delta\nu^{(1)} \approx \nu_Q(2I - 1) \qquad (3.35)$$

and for the central line the width is

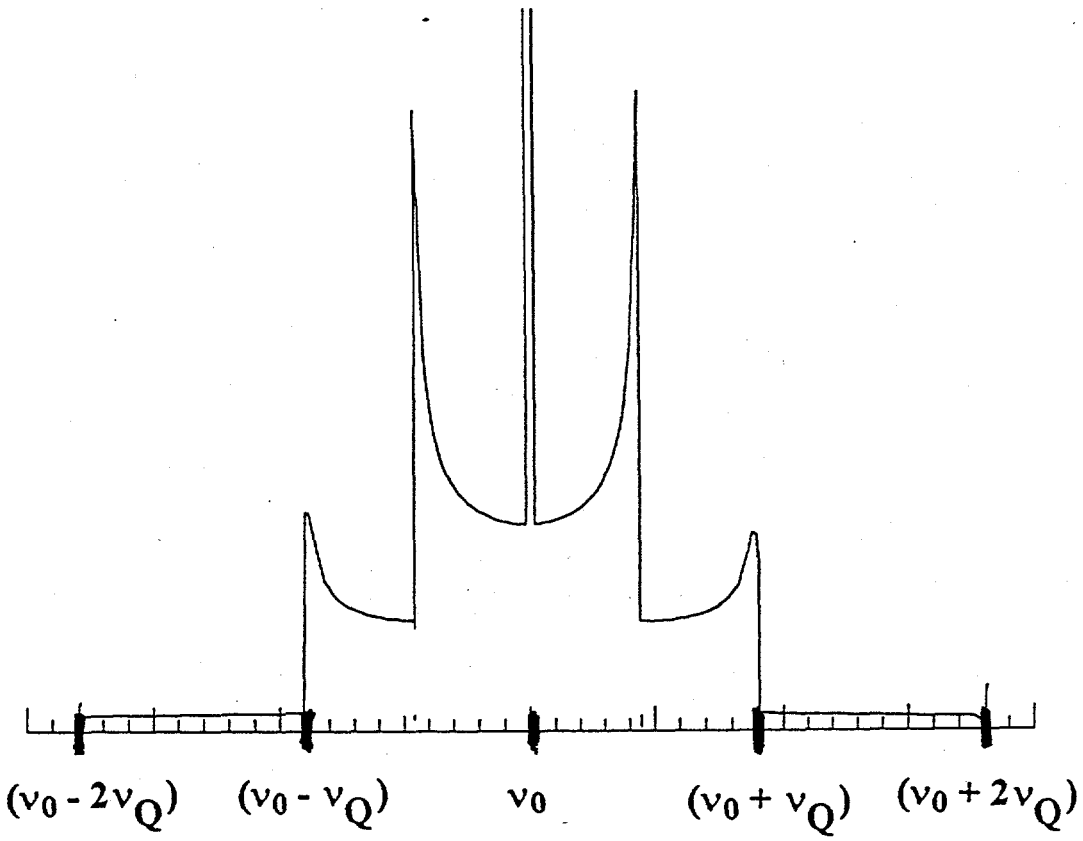

Fig. 3.3 NMR powder spectrum. For a single non-equivalent site in a powdered crystal sample, the distribution of grain directions results in a spectrum with distinct peaks. Pictured above is a powder pattern for an I = 5/2 quadrupolar nucleus, neglecting Knight shift effects, and taking $\eta = 0$.

$$\Delta\nu^{(2)} \approx \frac{25\nu_Q^{\,2}}{144\nu_0}(a-3/4) \qquad (3.36)$$

where a≡I(I+1).

The powder spectrum of Fig. 3.3 applies only when the structure of the solid for the resonant I = 5/2 nucleus has one nuclear site. In such cases, each nuclear site will be characterized by an EFG tensor having the same diagonal elements in its principal axis system. Thus all sites share the same values of ν_Q and η. If more than one non-equivalent site exists in the structure, ν_Q and η will not be the same for all sites. To determine the resulting composite powder pattern, one may sum the normalized powder patterns arising from unique values of ν_Q and η, if they are weighted by the number of such sites per unit cell. Fig. 3.4 illustrates how two non-equivalent sites for a nucleus with spin I = 5/2 gives rise to different powder patterns that are summed to get a composite pattern. For complicated structures with many non-equivalent sites, one must know the distributions of ν_Q and η.

E. Dynamic Properties: Nuclear Spin-Lattice Relaxation

We now wish to discuss how a spin system relaxes after being disturbed from thermal equilibrium by a sequence of RF pulses. This discussion will lead to expressions that will allow determination of the nuclear spin-lattice relaxation (NSLR) rate, important for studying the electronic density of states (DOS) in AlCuFe and AlCuRu quasicrystals. Since Al and Cu nuclei are of particular interest, we consider the case of a quadrupolar nucleus, in which the nuclear energy levels are not equally spaced.

1. Selective Irradiation: Initial Conditions

^{27}Al NMR spectra of AlCuFe and AlCuRu quasicrystals have quadrupole satellites extending continuously over ≈ 2 MHz. This makes it impossible to irradiate the entire s

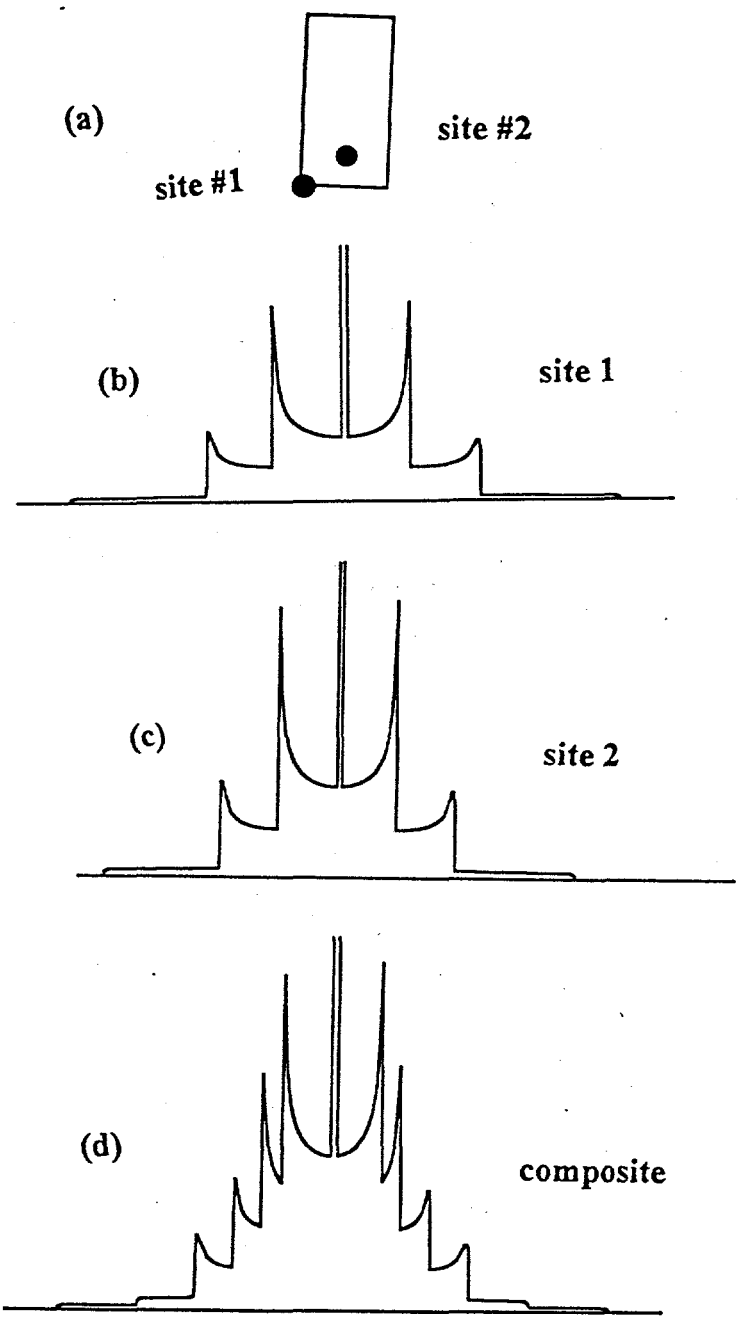

Fig. 3.4 Powder pattern for multiple non-equivalent sites. The two non-equivalent sites of (a) give rise to different individual powder patterns (b) and (c). The composite is formed by adding the two distributions of (b) and (c) weighted by the number of such sites in the unit cell.

spectrum uniformly and therefore saturate all energy levels simultaneously. For this reason, one must understand the effects of selectively irradiating a broad NMR line. Since the central line transitions has the largest intensity and therefore is easiest to detect experimentally, the focus here will be on the effects of the NSLR due to irradiation of the central line by "short" and "long" pulse sequences. In thermal equilibrium the nuclear spins distribute themselves over the various energy levels E_m according to the Boltzmann distribution $N/N_0 = e^{-E_m/k_BT}$, where T is the temperature of the thermal reservoir. Even at a relatively high magnetic field of $H_0 \approx 8$ T and relatively low temperature of 4 K, the ratio E_m / k_BT is on the order of 10^{-3}, making the "high temperature" expansion $N/N_0 \approx 1 - E_m / k_BT$ valid. Assuming the high temperature approximation, the populations of the quadrupole levels are depicted schematically in Fig. 3.5 for I = 5/2, on a highly expanded N/N_0 scale. Fig. 3.5 shows E_m versus N/N_0 in thermal equilibrium, and therefore the slope of the line through all the points is equal to $-k_BT$. One defines "spin temperature" T_s in terms of the slope $-k_B T_s$ between adjacent energy levels. Spin temperature give another way of thinking about the energy level populations when the system in not in equilibrium. Inducing transitions between adjacent levels decreases the population difference between them, making the slope $-k_B T_s$ larger. As the levels absorb energy, therefore, the spin temperature increases; saturating a pair of levels corresponds to $T_s = \infty$.

We now consider two ways to selectively irradiate the central line, and obtain the spin populations after irradiation in both cases. In the first case , a sequence of saturating pulses is applied for a duration $\tau << T_1$, where $T_1 = 1/2W_M$ is the spin-lattice relaxation time. In this case, the populations of the m = $\pm$ 1/2 are saturated and therefore correspond to a spin temperature $T_s = \infty$, but the pulses are not applied long enough to allow the satellite populations to come to equilibrium with the populations in the m = $\pm$ 1/2 levels. In the second case, the saturating pulses are applied for a time $\tau >> T_1$, thus allowing lattice

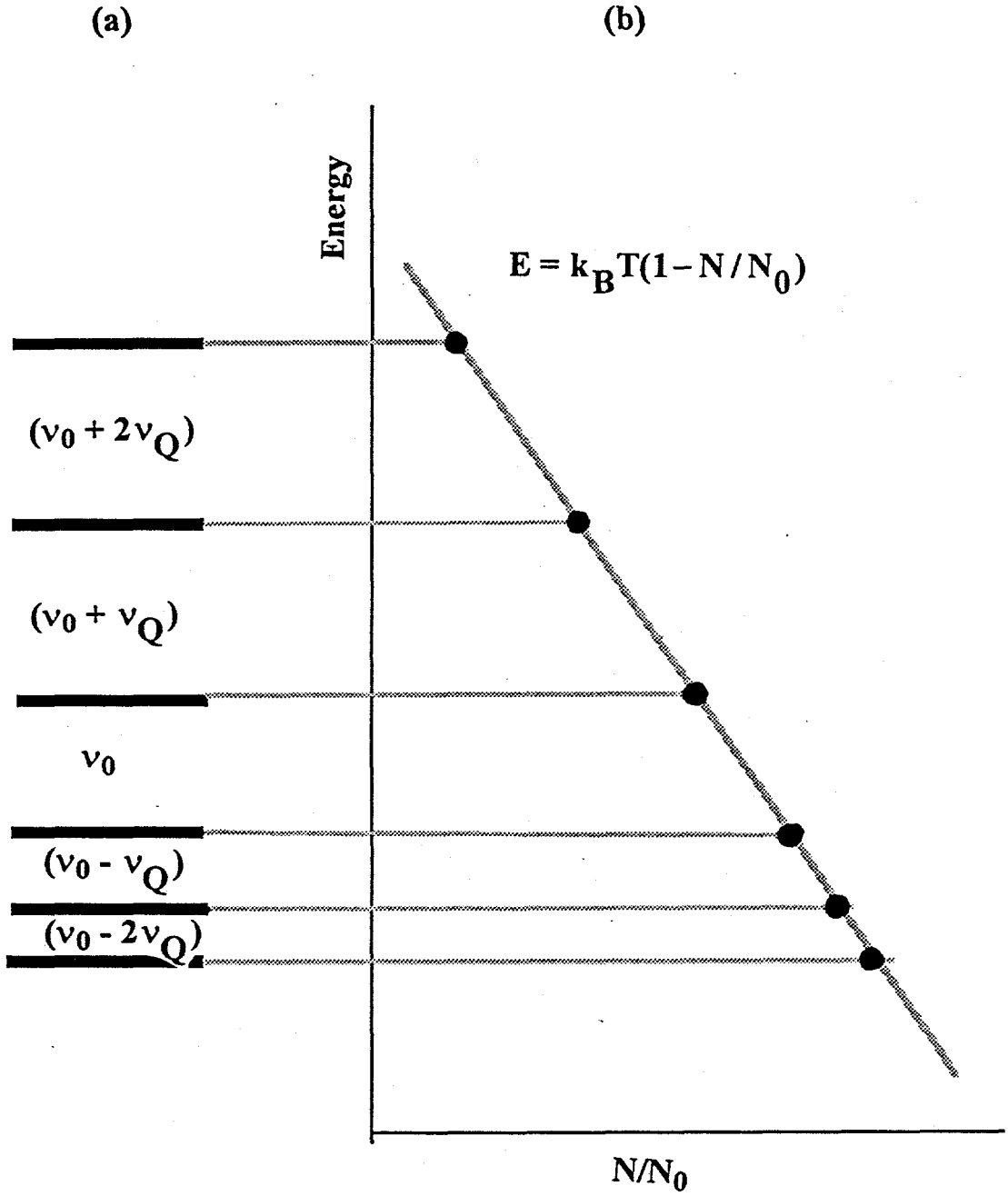

Fig. 3.5 Energy levels and relative nuclear spin populations for I = 5/2. (a) Energy levels for a quadrupolar nucleus with coupling frequency ν_Q and orientation $\theta = 0°$; (b) Nuclear energy E versus relative population N/N_0, where N_0 is the total number of spins in the system. This is linear to a good approximation.

relaxation to bring the satellites intoequilibrium with the m = ± 1/2 levels. The populations of the levels for each case are shown in Fig. 3.6, and the changes in the populations of each level are straightforward to determine. The relative change in population for level m may be defined

$$n_m(t) \equiv \frac{N_m(t) - N_m^0}{N_0} \tag{3.37}$$

and the normalized magnetization due to the m↔m-1 transition is

$$a_m \equiv n_m - n_{m-1} \tag{3.38}$$

The initial values $n_m(0)$ may be readily determined for each saturation condition by examining Fig.s 3.6 (a) and (b). The lightly shaded lines indicate the equilibrium population levels, and therefore $n_m(0)$ is the displacement from the dotted line in Fig. 3.6 which indicates the equilibrium levels. The values of $n_m(0)$ are given for I = 5/2 in Fig. 3.6, and determining the $a_m(0)$ is straightforward.

2. Solution of the Master Equation

After the spin system has been excited from equilibrium, NSLR processes return the populations to equilibrium by coupoing the nuclei to time varying electric and magnetic fields that induce transitions to lower energy levels. These time dependent fields induce ransitions from levels j to i with a rate W_{ij}, and the normalized level populations are given by the "master equation"

$$\dot{n}_i(t) = \sum_j \left(n_j(t) W_{ij} - n_i(t) W_{ji} \right) \tag{3.39}$$

To go further, one must assume a form for W_{ij} by postulating a relaxation mechanism or combination of relaxation mechanism. In metal alloys one of the primary sources of relaxation is through the hyperfine interaction of the nuclear moment with the electronic moment of the conduction electrons. This gives transition rates of the form [40]

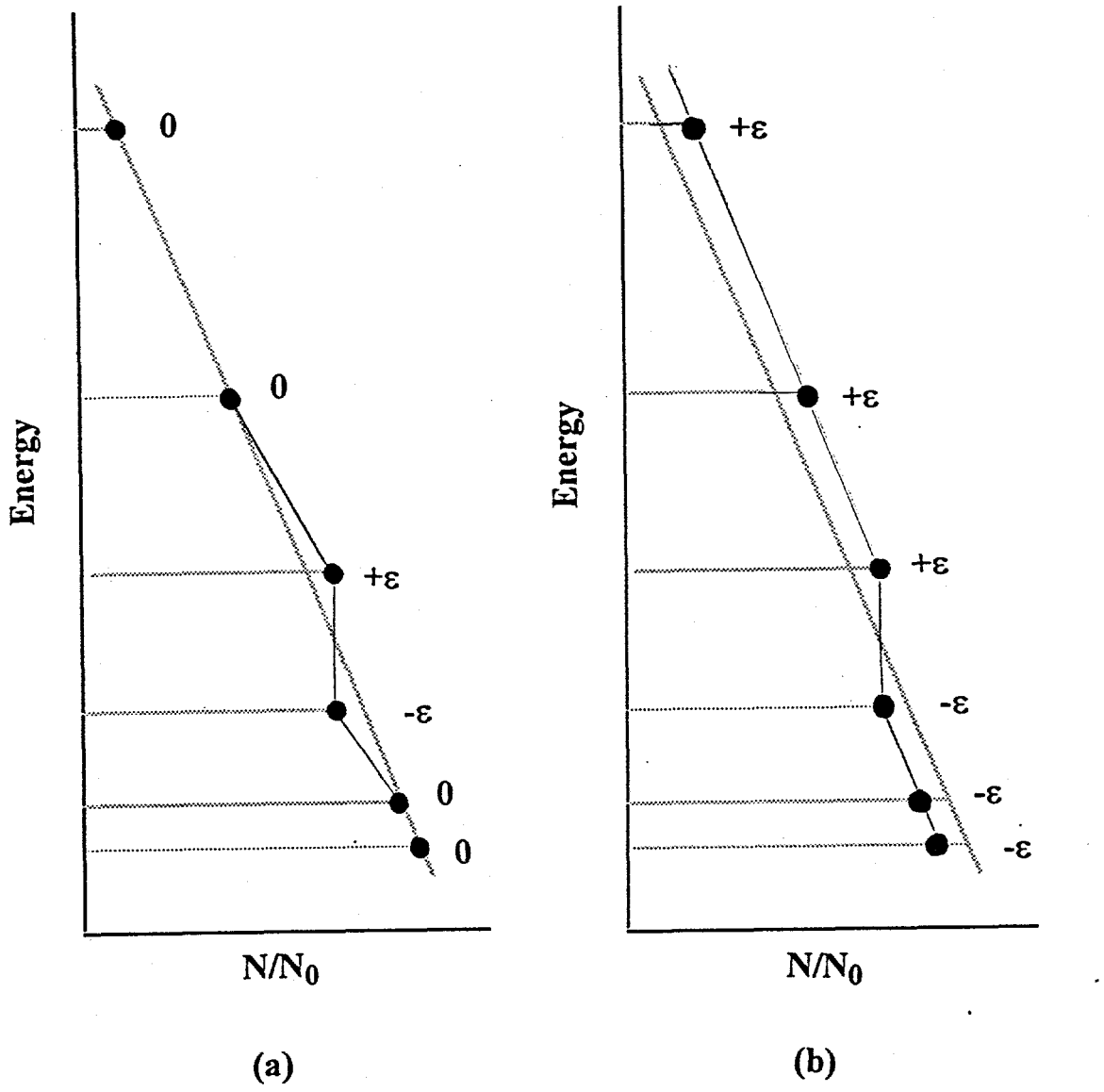

Fig. 3.6 Spin populations after selective irradiation for I = 5/2. Long and short pulse sequences result in different populations immediately after irradiation: (a) short pulse sequence ($\tau << T_1$); (b) long pulse sequence ($\tau >> T_1$). The quantity beside each point is $n_m(0) \equiv \frac{N_m(0) - N_m^0}{N_0}$, where $\varepsilon = {}^{h\nu_0}/_{2k_BT}$.

$$W_{n,m} = W_M(I \pm m)(I \mp m + 1)\delta_{m,n\pm1} \tag{3.40}$$

where [34]

$$W_M \propto k_B T \gamma_e^2 \gamma_n^2 \left\langle |\psi(0)|^2 \right\rangle_{FS} D_s^2(E_F) \tag{3.41}$$

gives the the dependence of W_M on the temperature T, the electronic and nuclear gyromagnetic ratios γ, the average over the Fermi surface of the s - electron proability function, and the s - band density of states squared. This allows one to write the master equation as

$$\dot{n}_i(t) = n_{i-1}(t)W_{i,i-1} + n_{i+1}(t)W_{i,i+1} - n_i(t)\left(W_{i-1,i} + W_{i+1,i}\right) \tag{3.42}$$

or in terms of the normalized magnetization

$$\dot{a}_i \equiv \dot{n}_i - \dot{n}_{i-1} = W_M\left\{a_{i-1}A_{i,i-1} + a_iA_{i,i} + a_{i+1}A_{i,i+1}\right\} \tag{3.43}$$

where [40 Narath]

$$\begin{aligned} A_{i,i+1} &\equiv \left[I(I+1) - i(i+1)\right] \\ A_{i,i} &\equiv -2\left[I(I+1) - i(i-1)\right] \\ A_{i,i-1} &\equiv \left[I(I+1) - (i-1)(i-2)\right] \end{aligned} \tag{3.44}$$

tThis is the equivalent of the matrix equation

$$\dot{\mathbf{a}} = \mathbf{A}\mathbf{a} \tag{3.45}$$

where a is a vector with 2I+1 components a_i, and A is a (2I+1)×(2I+1) matrix with components A_{ij}. may be solved in the standard way by picking solutions of the form $\mathbf{c}_i e^{-\lambda_i t}$. The master equation then becomes an eigenvalue problem, and the eigenvectors $\mathbf{c}_i$ and eigenvalues λ_i may be found. The most general solution for a(t) is a linear combination of the different modes $\mathbf{c}_i e^{-\lambda_i t}$ and may be written

$$\begin{aligned}\mathbf{a}(t) &= \alpha_1 \mathbf{c}_1 e^{-\lambda_1 t} + \alpha_2 \mathbf{c}_2 e^{-\lambda_2 t} + \ldots \\ &= \begin{pmatrix} \vdots & \vdots & \\ \mathbf{c}_1 & \mathbf{c}_2 & \cdots \\ \vdots & \vdots & \end{pmatrix} \begin{pmatrix} \alpha_1 e^{-\lambda_1 t} \\ \alpha_2 e^{-\lambda_2 t} \\ \vdots \end{pmatrix}\end{aligned} \tag{3.46}$$

Defining

$$\mathbf{C} \equiv \begin{pmatrix} \vdots & \vdots & \\ \mathbf{c}_1 & \mathbf{c}_2 & \cdots \\ \vdots & \vdots & \end{pmatrix}$$

$$\mathbf{D} \equiv \begin{pmatrix} e^{-\lambda_1 t} & & \mathbf{0} \\ & e^{-\lambda_2 t} & \\ \mathbf{0} & & \ddots \end{pmatrix} \tag{3.47}$$

$$\alpha \equiv \begin{pmatrix} \alpha_1 \\ \alpha_2 \\ \vdots \end{pmatrix}$$

one may write

$$\mathbf{a}(t) = \mathbf{C}\mathbf{D}\alpha \tag{3.48}$$

Since D(0) = 1 this implies

$$\mathbf{a}(0) = \mathbf{C}\alpha \tag{3.49}$$

and therefore

$$\boldsymbol{\alpha} = \mathbf{C}^{-1}\mathbf{a}(0) \tag{3.50}$$

The general solution is therefore

$$\mathbf{a}(t) = \mathbf{C}\mathbf{D}\mathbf{C}^{-1}\mathbf{a}(0) \tag{3.51}$$

3. Solutions: Case of Magnetic Relaxation and I = 3/2, 5/2

Therefore, for I = 3/2 and 5/2, once the initial conditions of saturation a(0) are known, the eigenvectors $\mathbf{c}_i$ and eigenvalues λ_i are known, a(t) may be found assuming magnetic relaxation. Since we are only interested in the relaxation of the central line, we only need calculate $a_{1/2}(t)$. These relations are given below for the conditions $\tau << T_1$ (1) and $\tau >> T_1$ (2).

I = 3/2

(1) $$a_{1/2} = 0.1e^{-2W_M t} + 0.9e^{-12W_M t} \tag{3.52}$$

(2) $$a_{1/2} = 0.4e^{-2W_M t} + 0.6e^{-12W_M t}$$

I = 5/2

(1) $$a_{1/2} = 0.029e^{-2W_M t} + 0.178e^{-12W_M t} + 0.794e^{-30W_M t} \tag{3.53}$$

(2) $$a_{1/2} = 0.257e^{-2W_M t} + 0.267e^{-12W_M t} + 0.476e^{-30W_M t}$$

CHAPTER 4. EXPERIMENTAL DETAILS

In this chapter we discuss the details of the NMR/NQR experiments performed in the study of the AlCuFe, AlCuRu, and AlPdMn alloys. In discussing sample preparation, different batches of the same sample stoichiometry are given different numbers to allow distinguishing between them.

A. Sample Preparation

1. Batch #1, #3 Samples

$Al_{85-x}Cu_xRu_{15}$, x=15,17,20 and $Al_{65}Cu_{23}Fe_{12}$ alloys were prepared by arc melting appropriate proportions of high purity (better than 99.9%) metals in an argon atmosphere. To insure complete mixing, each button was turned over and remelted twice. The buttons were then broken and examined by eye for homogeneous mixing of the metals. They were then remelted into ingots. The ingots were then sealed inside quartz tubes at 10^{-4} torr in preparation for heating. The quasicrystalline phases were prepared by heating both the AlCuRu and the AlCuFe ingots at 800 °C for 23 days. In order to obtain the C phase of the AlCuFe system [41], [42], [43], [44] one of the quasicrystalline ingots was further heated at 650 °C for 50 hours. For annealing, samples were placed into preheated furnaces, and cooled by removing from the furnace and allowing the ingot to come to room temperature. The final ingots were ground into powders for susceptibility and NMR measurements. Prior to the NMR measurements the quasicrystalline powder samples were checked with x-ray scans. The AlCuFe sample in the C phase shows peak broadening asymmetry consistent with the twinned rhombohedral phase [41], [42].

2. Batch #2 Sample

This $Al_{68}Cu_{17}Ru_{15}$ was prepared as described above. Annealing was performed in the following way: from a room temperature furnace the ingot was heated up to 500 C, where it was held for one day. Temperature was then increased to 600 C and held 6 hours, and then

heated to 800 C and held for 18 days. It was furnace cooled by simply shutting off the furnace power [45]. The approximately 7 gram ingot was cut for specific heat measurements, and Swenson [46] reports $\gamma = 0.216 \pm 0.003$ mJ/g-atK^2 and $\theta_D = 542$ K, in very good agreement with the values of Biggs et al. [31] ($\gamma = 0.23$ mJ/g-atK^2 and $\theta_D = 527$ K). This agreement made this sample a good candidate for a high temperature NMR study similar to that of Hill et al., who used an $Al_{65}Cu_{20}Ru_{15}$ sample provided by Biggs et al.

3. AlPdMn Single Grain and Powder

Single grain and powder samples of $Al_{70}Pd_{21.5}Mn_{8.5}$ quasicrystals were also prepared. The single grain sample was the same sample used in a previous x-ray study [24]. It was prepared by first growing single grain regions in an ingot using the Bridgman technique. A single grain was selected and then cut from the ingot after neutron diffraction was used to determine the single grain regions. This region was cut to the dimensions 0.1 x 0.28 x 0.5 inches with 2-fold axes perpendicular to the two largest faces. X-ray topography was then used to study the two largest surfaces, and the sample was flipped 180° to insure that both sides were perpendicular to 2-fold axes. The powder sample was prepared by arc melt drop casting and was better than 90% face-centered icosahedral (FCI) phase.

B. Experiments and Apparatus

NMR an NQR experiments were performed with a phase-coherent pulse spectrometer employing a programmable pulse sequencer [47], a double sideband RF switch [48], and an NMR receiver following the design of Adducci et al. [49], as shown schematically in Fig. 4.1.

1. Field and Frequency Sweeping

Both the ^{27}Al and ^{63,65}Cu nuclei investigated have $I > \frac{1}{2}$ and sizable quadrupole moments. As a result, the NMR spectrum displays a narrower field dependent central line ($+\frac{1}{2} \leftrightarrow -\frac{1}{2}$) transition and a field independent broader line arising from the distribution of satellite

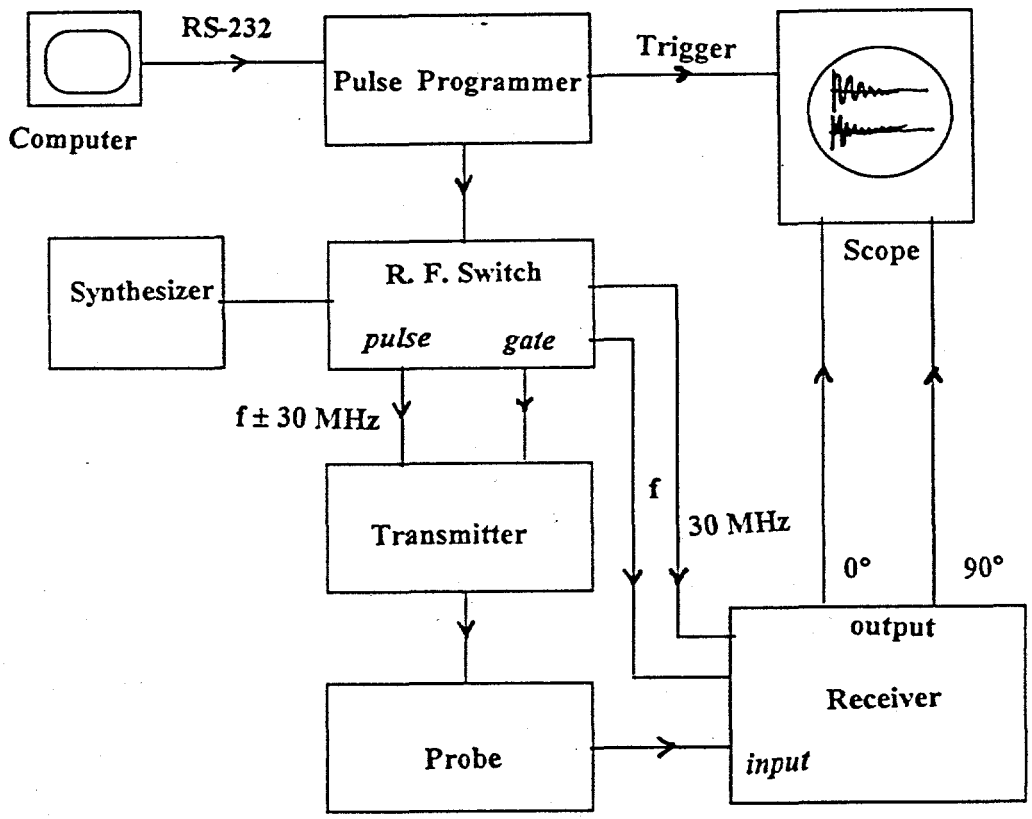

Fig. 4.1 Block diagram of an NQR-NMR pulse spectrometer.

$(\pm\frac{5}{2}\leftrightarrow\pm\frac{3}{2},\ \pm\frac{3}{2}\leftrightarrow\pm\frac{1}{2})$ transitions. At 8.2 T the full width at half maximum (FWHM) of the central line is 50 kHz for ^{27}Al and 200 kHz for ^{63}Cu. The RF field H_1 was about 50 G at these frequencies allowing one to uniformly irradiate the ^{27}Al central line and about a quarter of the ^{63}Cu central line. Thus the line shape of the central line can be obtained directly by FT of half of the echo signal only for ^{27}Al.

In order to obtain the central line spectrum at low field, where the line is broader, and the spectrum of the satellite distribution, we had to use either frequency swept or field swept scans. In both cases the echo signal was generated by a two pulse Hahn echo sequence. For field scans the echo signal was integrated by means of a boxcar integrator and the integrated signal was digitized and stored in a Nicolet 1170 signal averager while the external magnetic field was scanned slowly and continuously. Usually 100-200 scans were sufficient to obtain a good signal to noise ratio. For frequency scans the spectrum was obtained point by point by changing the irradiating frequency in steps that varied from 10 kHz in the central lines to 200 kHz in the satellite distribution. The NMR probe was retuned at each frequency. A silver RF coil was used to avoid spurious ^{63,65}Cu signals, and all calibrations were made by using the ^{27}Al resonance in a saturated aqueous $AlCl_3$ solution.

The schematic of Fig. 4.2 indicates the layout for the automatic field sweep apparatus for the low field magnets. A Nicolet 1170 signal averager, and Ames Laboratory DC linear amplifier [48] and a Varian external sweep adapter were used to slowly sweep the magnetic field. The receiver's boxcar integrator was used to integrate symmetrically through the echo signal, and the Nicolet 1170 was used to digitize the integrated signal and store the data as the field was advanced. All measurements were performed at 77 K using an Oxford system transfer tube, Oxford CF 1200 variable temperature cryostat, and a liquid nitrogen storage dewar. A small calibration probe containing a small sample of saturated aqueous $AlCl_3$

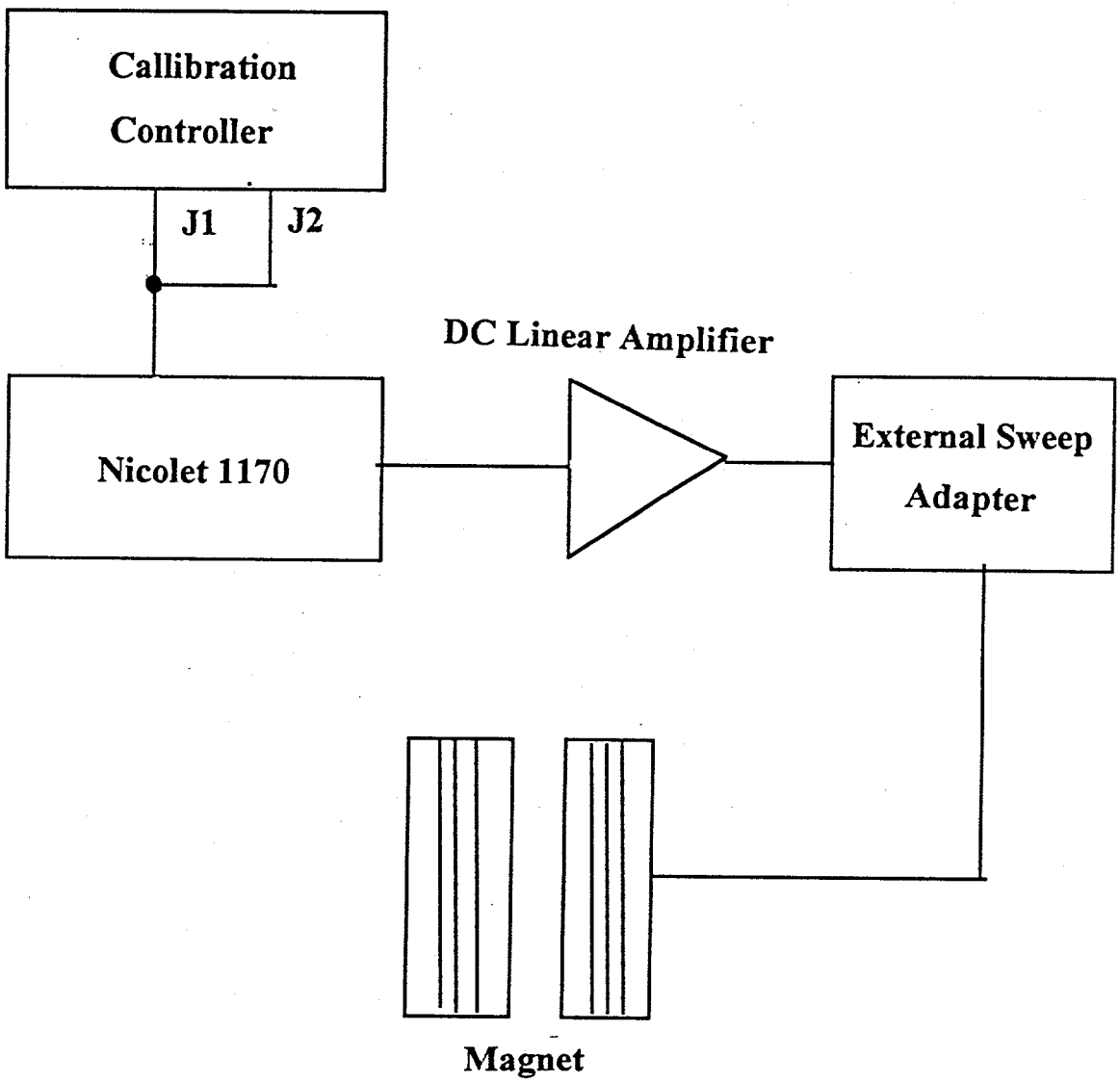

Fig. 4.2 Schematic diagram of automatic field sweep apparatus for iron core magnets.

solution was located at the level of the sample position outside the cryostat. The calibration probe was used to mark reference frequencies on the data over a range of 4 MHz.

2. NQR Measurements

The ^{27}Al NQR signal was detected at 4.2 K as an echo signal following a $\frac{\pi}{2}\Big|_{\{x,\bar{x}\}} - \frac{\pi}{2}\Big|_{y}$ pulse sequence with $\tau_{\pi/2} = 10$ μs and pulse separation 100 μs. Approximately 4 g of AlCuRu and $Al_{65}Cu_{23}Fe_{12}$ were used. The spectra were obtained by plotting the echo intensity vs. the frequency of irradiation with proper renormalization for variations of Q factor, and transmitter power. Several data points were taken near 4 MHz, and the data were averaged to obtain error bars. In addition , the intensities were divided by ν_R to correct for the Boltzmann factor. For ^{27}Al (I = 5/2) one expects two resonance lines [34]. The ±3/2 ↔ ±1/2 transition occurs at $\nu_1 = \nu_Q g(\eta)$, where $\nu_Q \equiv 3eQ\left|V_{zz}^{tot}\right|/20h$, eQ is the nuclear quadrupole moment, and the asymmetry parameter $\eta \equiv (V_{xx} - V_{yy})/V_{zz}$. The function $g(\eta)$ was tabulated in [36], and varies from 1 for $\eta = 0$ to 1.8 for $\eta = 1$. The $\pm 5/2 \leftrightarrow \pm 3/2$ transition occurs at $\nu_2 = 2\nu_Q f(\eta)$, and $f(\eta)$ varies from 1 at $\eta = 0$ to 0.88 at $\eta = 1$ [36]. The echo intensity at the lowest end of the frequency spectrum may have been slightly underestimated as a consequence of the decrease of the power output of the RF power amplifier. The NQR spectrum we report is ascribed to the $\pm 5/2 \leftrightarrow \pm 3/2$ transition of ^{27}Al, and the average ν_R from NQR agreed well with previous quadrupole perturbed NMR spectra in AlCuFe and AlCuRu [10]. Due to the extreme width of the NQR spectrum and to the very short $T_2 = 80$ μs, the signal-to-noise ratio was poor even at 4.2 K. In order to enhance the echo intensity, a weak D. C. magnetic field ($H_0 \approx 30$ G) was applied perpendicular to the axis of the NQR sample coil, by means of Helmholtz coils. The applied field was small enough that it did not affect the shape or width of the NQR spectrum, but was large enough to decouple the nuclear spins, making T_2 longer ($T_2 = 500$ μs) [50].

3. Medium Pressure NMR Experiment

Approximately 200 mg of $Al_{65}Cu_{20}Ru_{15}$ were sealed in compressible tubing (heat shrink tubing worked well), and a small silver solenoidal coil of diameter 0.5 cm was wound to fit the sample tube. The experiment was performed at the Washington University Physics Department, St. Louis, MO, where a titanium metal pressure cell was built for pressures on the order of 10^3 atmospheres. Fig. 4.3 shows a schematic layout of the pressure rig used to pressurize the sample chamber. Helium gas was used, along with a gas compressor, to increase the pressure to 2,000 atm., while the entire sample probe was immersed in a liquid nitrogen bath in an Oxford 8 T superconducting magnet. ^{27}Al NMR central line spectra were obtained by Fourier transforming the half-echo obtained from a Hahn echo sequence, where phase alternation was used to eliminate ringdown from the second pulse. ^{65}Cu spin-lattice relaxation time measurements were made by irradiation of the central line by 40 $\pi/2$ pulses preceeding a Hahn echo detection sequence. The relaxation data was fit using the relaxation law for long irradiation times to obtain the spin-lattice relaxation rate.

4. High Temperature NMR Measurements

1-2 g of $Al_{68}Cu_{17}Ru_{15}$ were sealed in a quartz tube under 1/2 atm. of argon gas at room temperature. The NMR detection coil was formed from uninsulated platinum wire, and temperatures were measured with an Oxford type E thermocouple placed near the sample coil.

The high temperature probe followed a design by Torgeson [51], and was able to approach temperatures of 700 K. A single pulse saturation technique and Hahn echo detection was used to obtain spin-lattice relaxation data, which was analyzed using the recovery law for short irradiation.

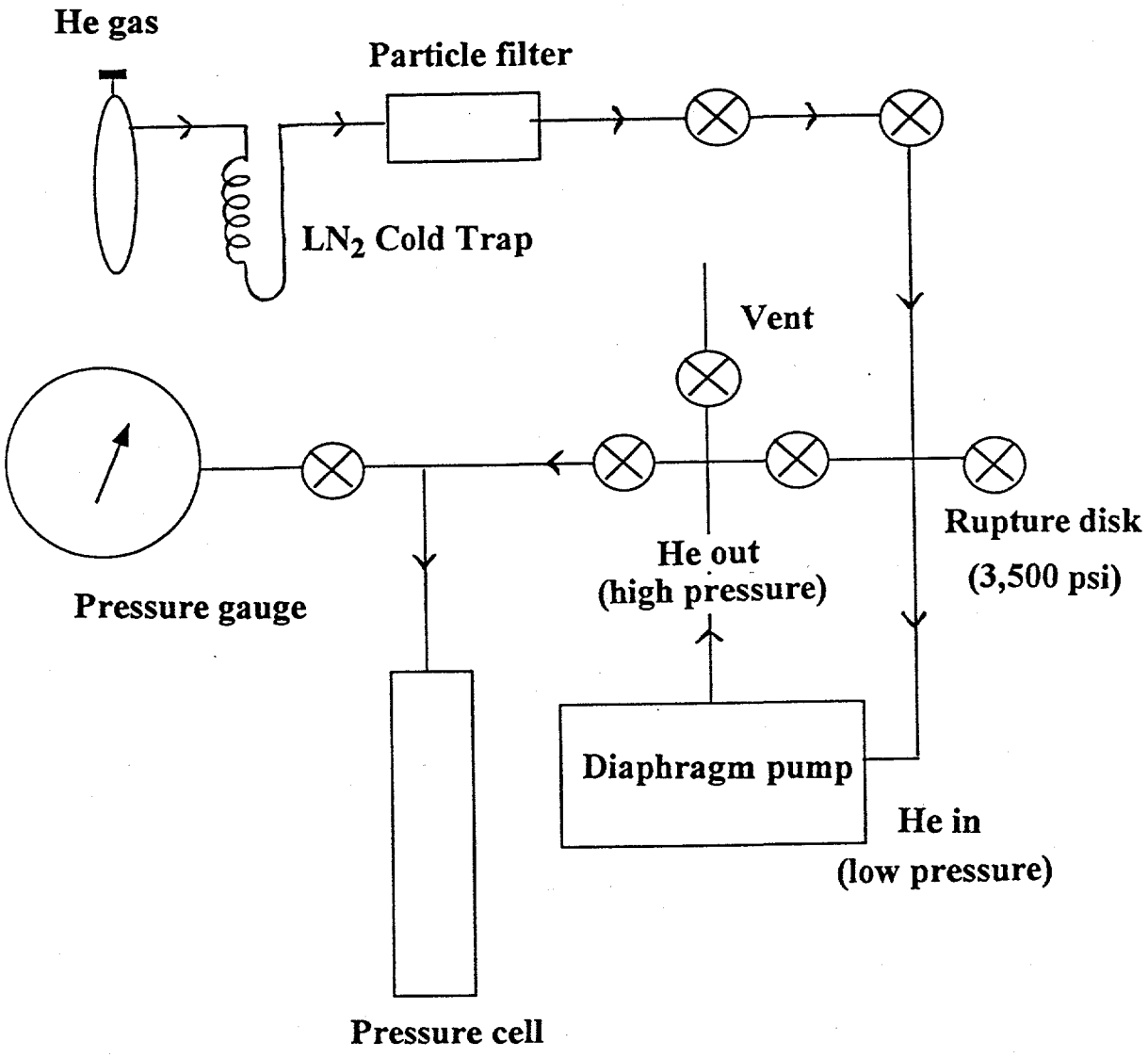

Fig. 4.3 Schematic diagram of the helium pressure rig used. The sample and detection coil were contained in the pressure cell, which was submerged in a liquid nitrogen bath, in a magnetic field of 8 T.

C. Data Analysis

1. Nuclear Spin-Lattice Relaxation

For quadrupolar nuclei, the recovery of the magnetization following a saturating RF pulse is not generally exponential. In order to extract the correct value for the relaxation transition probability, W, one has to know the dominant relaxation mechanism and the theoretical expression for the recovery law for a given initial saturation condition. For a magnetic relaxation mechanism, the recovery laws were derived in Chapter 3. Here W_m is the $\Delta m = \pm 1$ magnetic relaxation transition probability. For a quadrupolar relaxation mechanism two constants, W_1 and W_2, corresponding to the $\Delta m = \pm 1$ and $\Delta m = \pm 2$ allowed transitions respectively, have to be considered. In this case the analytical solution for the master equation is possible only for I=3/2 while for I=5/2 this can be done only in special cases (e.g. $W_1 = W_2$) [52].

Recovery laws for both purely quadrupolar and purely magnetic relaxation were tested to determine which resulted in better fits to the data. It was found that recovery laws for purely quadrupolar relaxation did not result in adequate fits, while the purely magnetic recovery curves did, as will be shown in Chapter 6.

The case of ^{63}Cu NSLR requires further discussion. As seen in Chapter 5, the ^{63}Cu resonance overlaps the ^{27}Al satellite transitions even at the highest field H=8.2 T. In order to derive the correct W_m pertaining to ^{63}Cu NSLR the following procedure was used: relaxation data were obtained both at the resonance frequency of ^{63}Cu and at the frequency symmetrically located with respect to the ^{27}Al central line frequency. Taking the difference of the two signals the recovery of the ^{63}Cu magnetization was obtained. The corrected and uncorrected W_m values were found to differ by only 10%, within the uncertainty of the measurements, indicating that the effect of overlap of ^{63}Cu is negligible and can be disregarded.

2. Computer Simulation of the Al NMR Line

An NMR line shape simulation program was used to generate simulated powder patterns, and the details of the code are presented in Appendix 1. NMR line shape simulations have been discussed by many authors [38], and applications to quasicrystalline materials have been reported [4], [9]. The need for such a program arises when many non-equivalent sites exist within the solid, thus washing out the distinct peaks seen in Chapter 3 for the case of a single non-equivalent site. By comparing a simulated NMR line, based on assumptions about the distributions of the EFG tensor components, with the data, and adjusting the assumed distributions until adequate fits are obtained, one may obtain reasonably accurate information about the underlying distribution of EFG components. A full discussion of the distributions found to result in good agreement will be given in Chapter 5.

CHAPTER 5. NMR AND NQR LINESHAPES AND STRUCTURAL PROPERTIES

We discuss the structural properties of quasicrystals that may be inferred from a study of the electric field gradient tensor at the sites of the resonant nuclei, through NMR and NQR.

A. Results

X-ray scans were performed on the batch #1 samples of AlCuFe and AlCuRu, as shown in Fig.s 5.1 and 5.2, and show high phase purity. The resolution limited diffraction peaks indicate that all batch #1 samples show a high degree of long-range order, consistent with previous studies [23].

1. ^{27}Al and ^{63,65}Cu NMR in Powder Samples

A typical high field NMR scan is shown in Fig. 5.3 (a). For all the batch #1 samples, the resonance peaks occur at nominally the same frequencies. In addition, the resonance frequencies ν of each line correspond to the transition frequencies $\nu = \gamma H_0$ for the central line of unshifted ^{27}Al and ^{63,65}Cu. Therefore, one may identify the resonances with their corresponding isotopes, as done in Fig. 5.3 (a). It should also be noted from the figure that, at this field of 8.2 T, the width of the ^{27}Al NMR central line is approximately 50 kHz, and that of the copper lines is 200 kHz. As mentioned in the previous chapter, the wide copper lines make studying them less attractive than the relatively intense and narrow aluminum line. For this reason, we will focus almost exclusively on the ^{27}Al resonance.

A study of the ^{27}Al line in all batch #1 samples over the temperature range from 10 K to 295 K show no change in line width nor any shift in the resonance frequency (Fig. 5.3b). The lack of temperature dependence is consistent with the diamagnetic character of the AlCuFe and AlCuRu samples (to be discussed in the next chapter), since the presence of localized moments typically makes the resonance frequency temperature dependent [39]. The NMR spectrum of the AlCuRu quasicrystal in Fig. 5.3a was obtained by using a sample in the form of a powder, and may therefore be compared with the NMR powder patterns

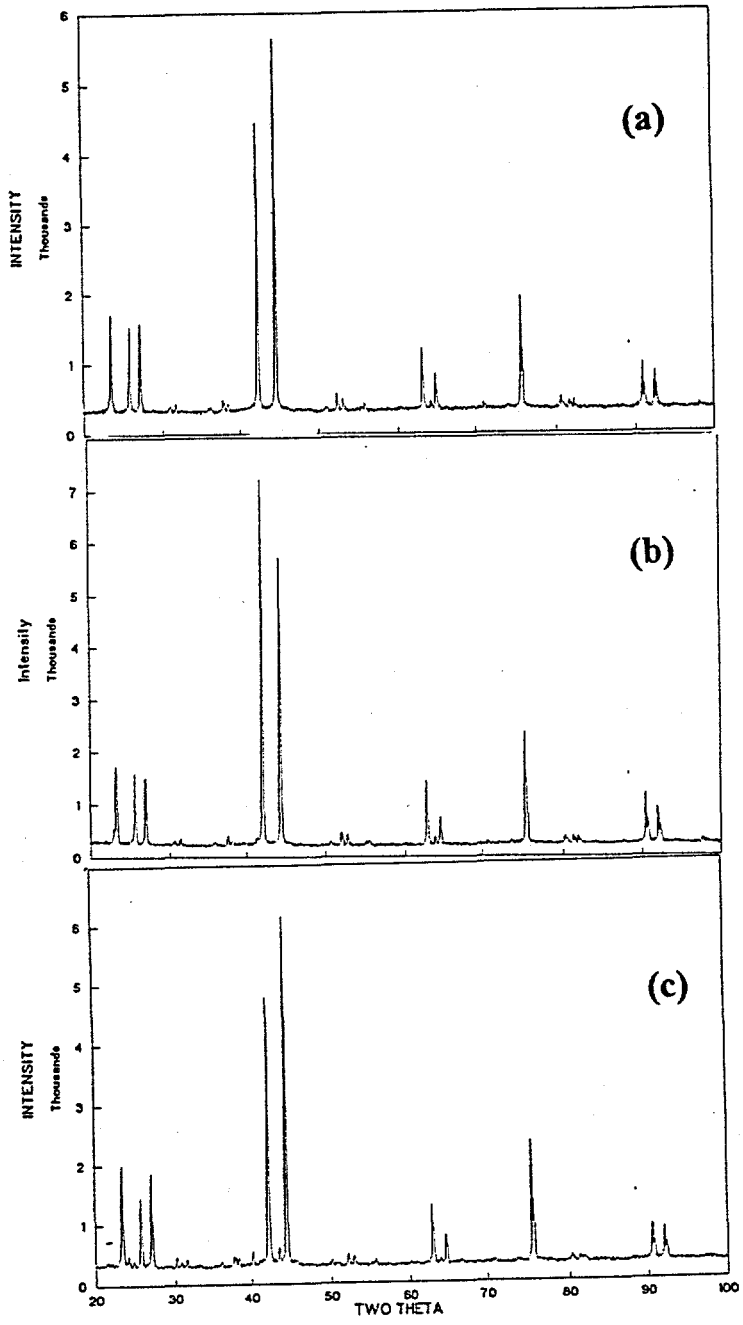

Fig. 5.1 X-ray scans for batch #1 AlCuRu quasicrystalline samples. (a) $Al_{65}Cu_{20}Ru_{15}$; (b) $Al_{68}Cu_{17}Ru_{15}$; (c) $Al_{70}Cu_{15}Ru_{15}$

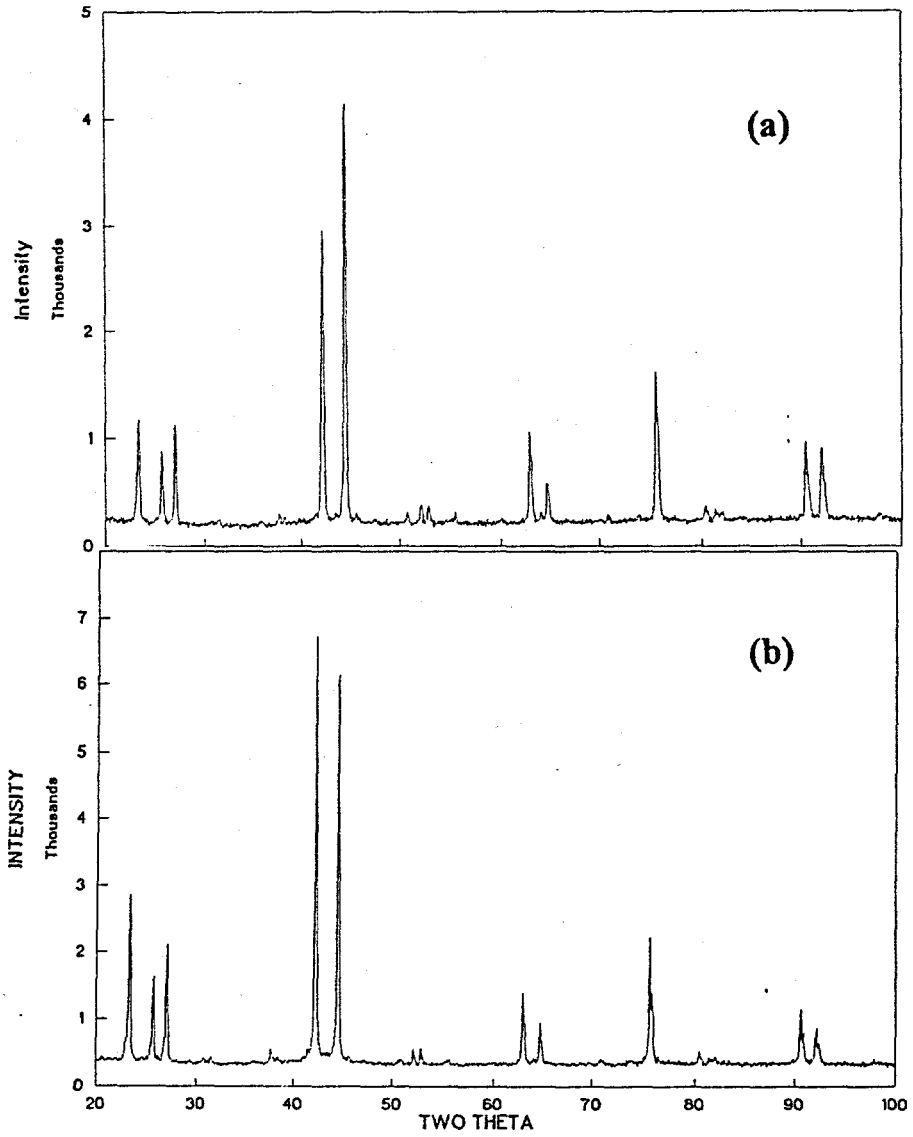

Fig. 5.2 X-ray scans for batch #1 AlCuFe samples. (a) $Al_{65}Cu_{23}Fe_{12}$ quasicrystalline phase; (b) $Al_{65}Cu_{23}Fe_{12}$ crystalline approximant.

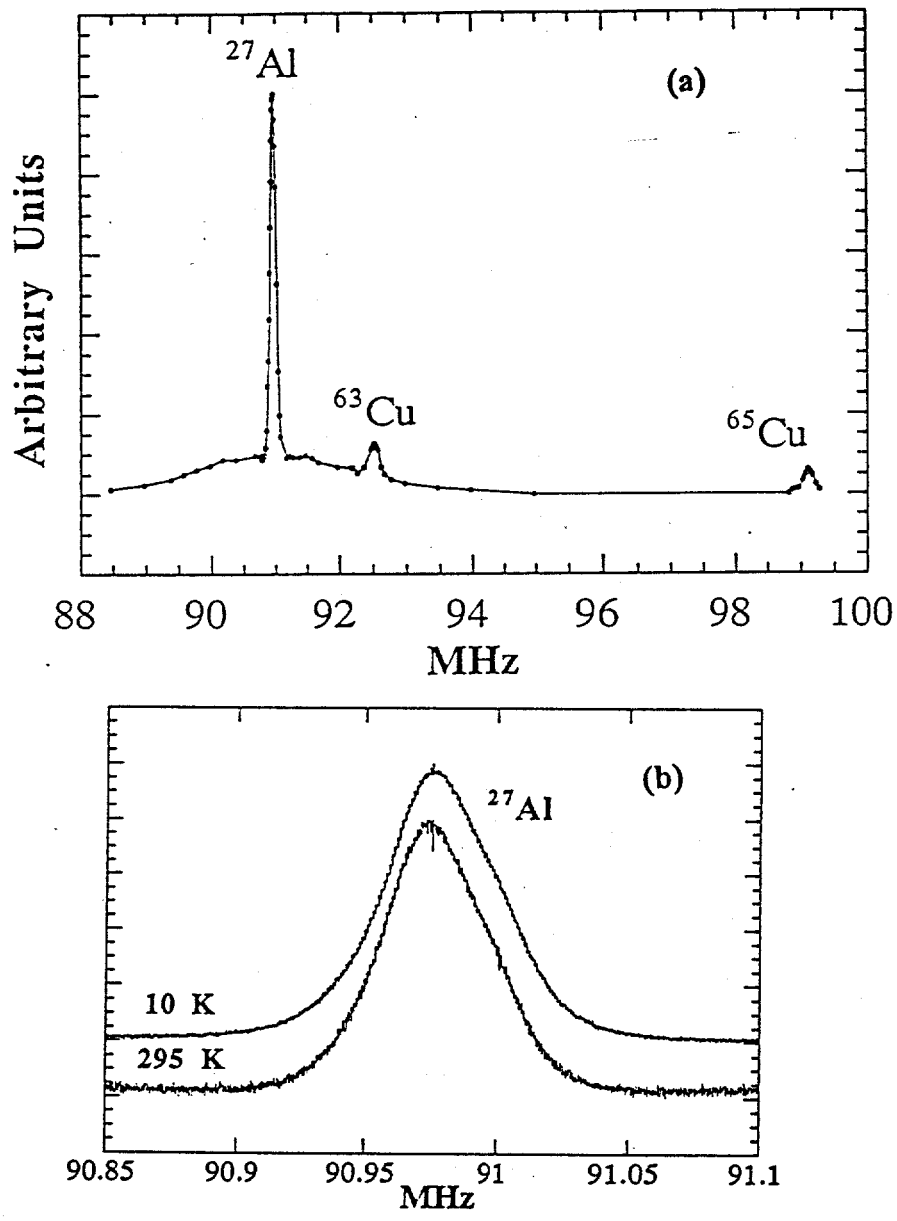

Fig. 5.3 (a) Typical NMR frequency scan for batch #1 samples. Above scan is for $Al_{65}Cu_{20}Ru_{15}$, and was taken at 8.2 T and 77 K. The scan shows a narrow ^{27}Al central line, a wide ^{27}Al satellite background, and ^{63,65}Cu central line resonances. Spectrum was obtained by plotting spin-echo height as a function of carrier frequency. (b) ^{27}Al central lines at 8.2 T , shown for 10 K and 295 K, by taking the Fourier transform of a half echo, using a Hahn echo sequence.

expected for a quadrupolar nucleus in a single non-cubic site (Fig. 3.3). The pattern for a single non-cubic site displays a distinct structure, which is not evident in the quasicrystal powder pattern, and which suggests that there exist distributions in the Hamiltonian parameters that determine the shape of the NMR line. These parameters are the Knight shift and electric field gradient tensor components ν_Q, η, K_{iso}, K_{an}, and ε. To determine, therefore, if the spectra are qualitatively consistent with powder spectra of quadrupolar nuclei, the ^{27}Al spectra were studied under three different resonance conditions in all the batch #1 samples. From Chapter 3, when the width of the central line is dominated by the second order quadrupole interaction, one expects the central line to scale with field as 1/H, and the distribution of the first order satellites to be field independent. Fig.s 5.4 through 5.8 are the result of NMR measurements made at 77 K for 12 MHz, 24 MHz, and 8.2 T, and one may readily verify that the broad background intensity is the same at each resonance condition. In addition, the ^{27}Al central line behaves qualitatively as expected for a line with strong quadrupole effects, its width increasing as the resonance frequency decreases. What remains in question is the distribution of NMR parameters that leads to such an effective washing out of the NMR line structure otherwise expected.

As discussed in Chapter 3, the "strength" of the quadrupole interaction for a given nucleus may be indicated by the quadrupole coupling frequency ν_Q, and may be measured approximately by the frequency spread of the quadrupole satellites. For nuclear spin I = 5/2, Fig. 3.3 indicates that the satellites cover $4\nu_Q$ in frequency, and taking this as roughly 6 MHz from the data of Fig. 5.4-5.8c, one gets an estimate for ν_Q of $\approx$ 6/4 MHz $\approx$ 2 MHz for the aluminum nuclei.

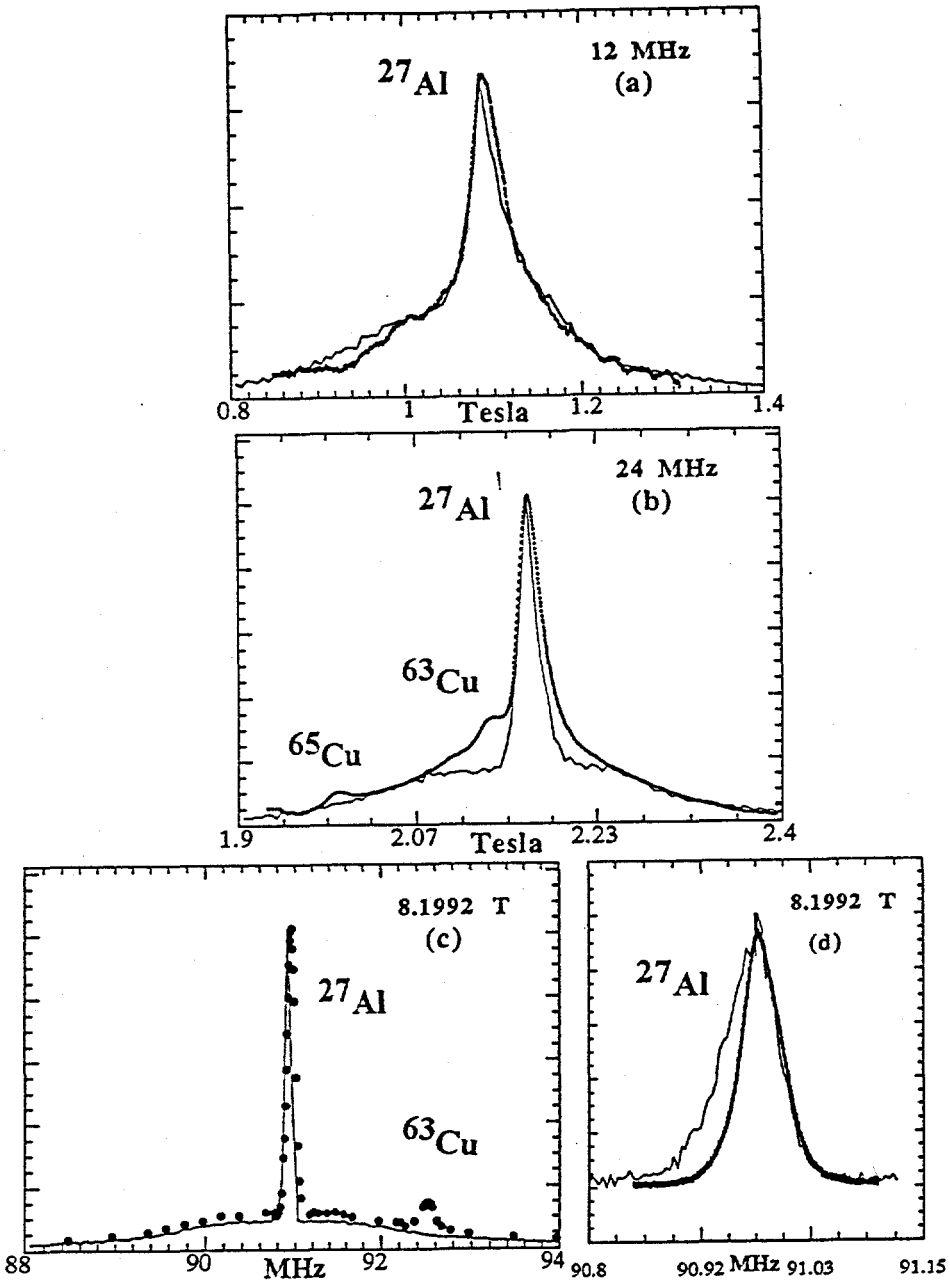

Fig. 5.4 Data and simulation for ^{27}Al NMR line in $Al_{65}Cu_{20}Ru_{15}$ at 77 K and three different resonance conditions. The heavy line is the data, the light line is the simulation. The parameters used in the simulation are: $\overline{\nu_Q}$=2.2 MHz; $\sigma = \overline{\nu_Q}/3$; η=0,0.1,0.2,...,0.5. (a) field scan at 12 MHz; (b) field scan at 24 MHz; (c) frequency scan at 8.2 T; (d) comparison of central line Fourier transform spectrum at 8.2 T with simulation.

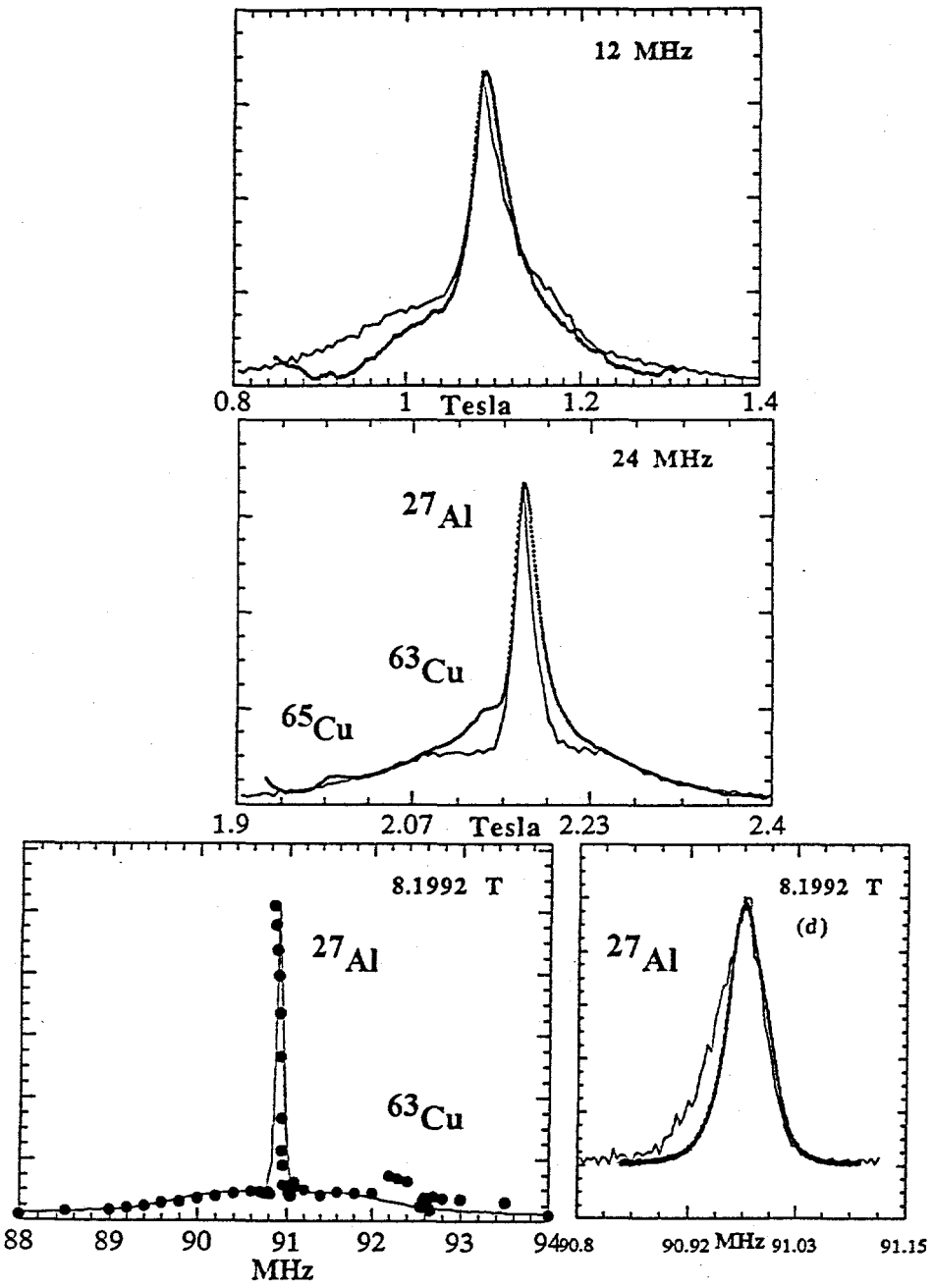

Fig. 5.5 Data and simulation for ^{27}Al NMR line in $Al_{68}Cu_{17}Ru_{15}$ at 77 K and three different resonance conditions. The heavy line is the data, the light line is the simulation. The parameters used in the simulation are: $\overline{\nu_Q}$=2.1 MHz; $\sigma = \overline{\nu_Q}/3$; η=0,0.1,0.2,...,0.5. (a) field scan at 12 MHz; (b) field scan at 24 MHz; (c) frequency scan at 8.2 T; (d) comparison of central line Fourier transform spectrum at 8.2 T with simulation.

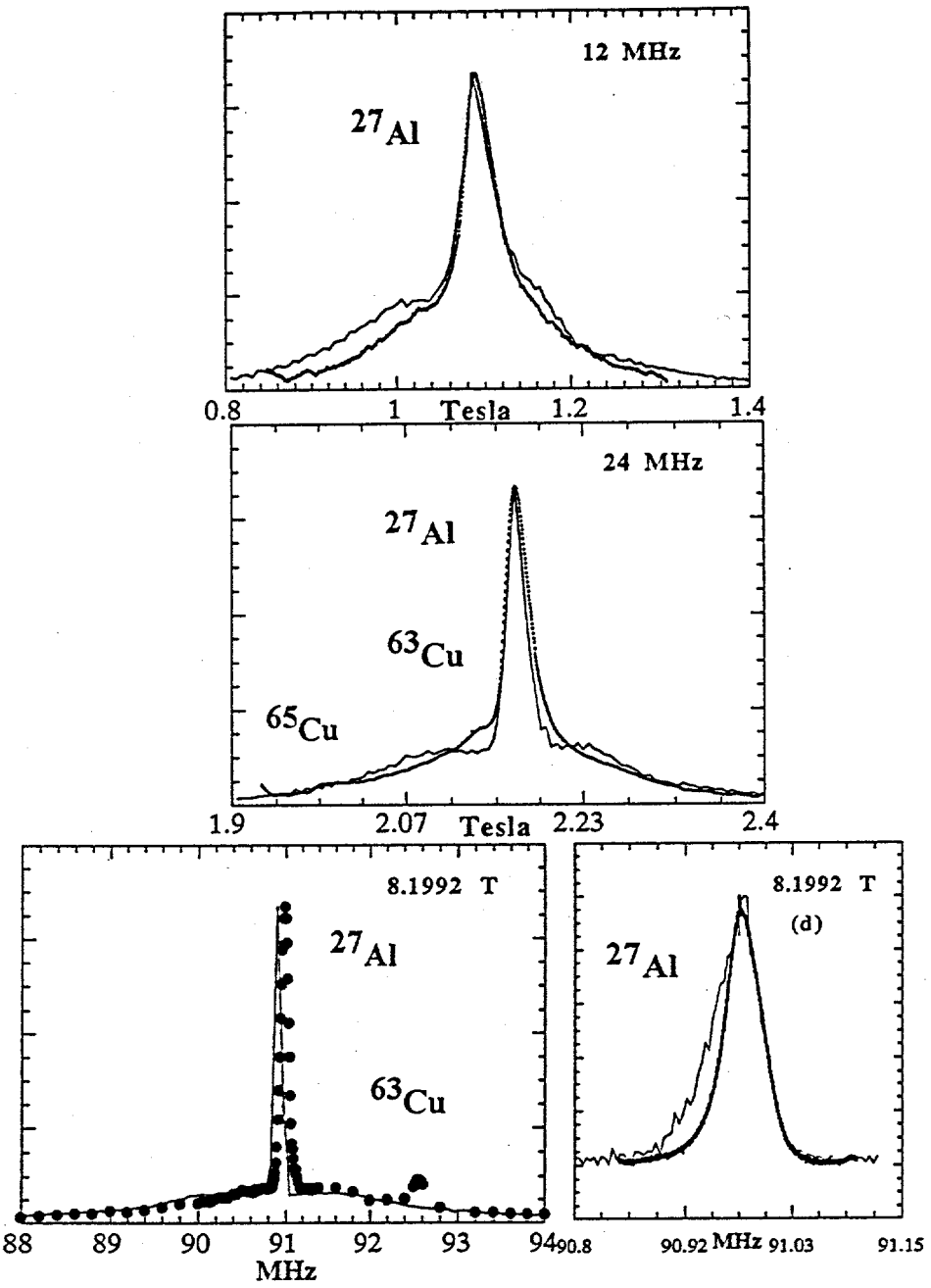

Fig. 5.6 Data and simulation for ^{27}Al NMR line in $Al_{70}Cu_{15}Ru_{15}$ at 77 K and three different resonance conditions. The heavy line is the data, the light line is the simulation. The parameters used in the simulation are: $\overline{\nu_Q}$=2.1 MHz; $\sigma = \overline{\nu_Q}/3$; η=0,0.1,0.2,...,0.5. (a) field scan at 12 MHz; (b) field scan at 24 MHz; (c) frequency scan at 8.2 T; (d) comparison of central line Fourier transform spectrum at 8.2 T with simulation.

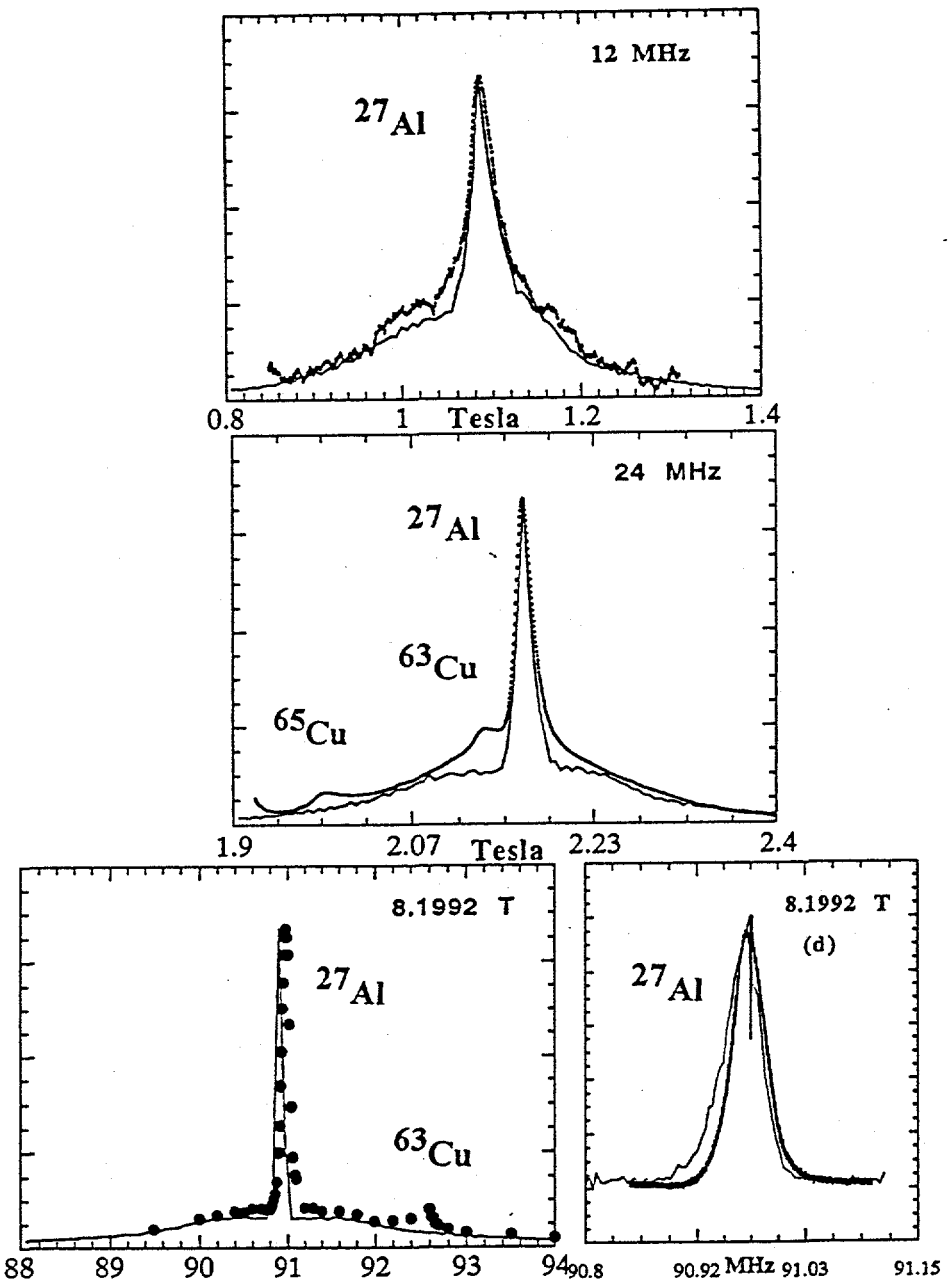

Fig. 5.7 Data and simulation for ^{27}Al NMR line in $Al_{65}Cu_{23}Fe_{12}$ crystalline approximant at 77 K and three different resonance conditions. The heavy line is the data, the light line is the simulation. The parameters used in the simulation are: $\overline{\nu_Q}$=1.9 MHz; $\sigma = \overline{\nu_Q}/3$; η=0,0.1,0.2,...,0.5. (a) field scan at 12 MHz; (b) field scan at 24 MHz; (c) frequency scan at 8.2 T; (d) comparison of central line Fourier transform spectrum at 8.2 T with simulation.

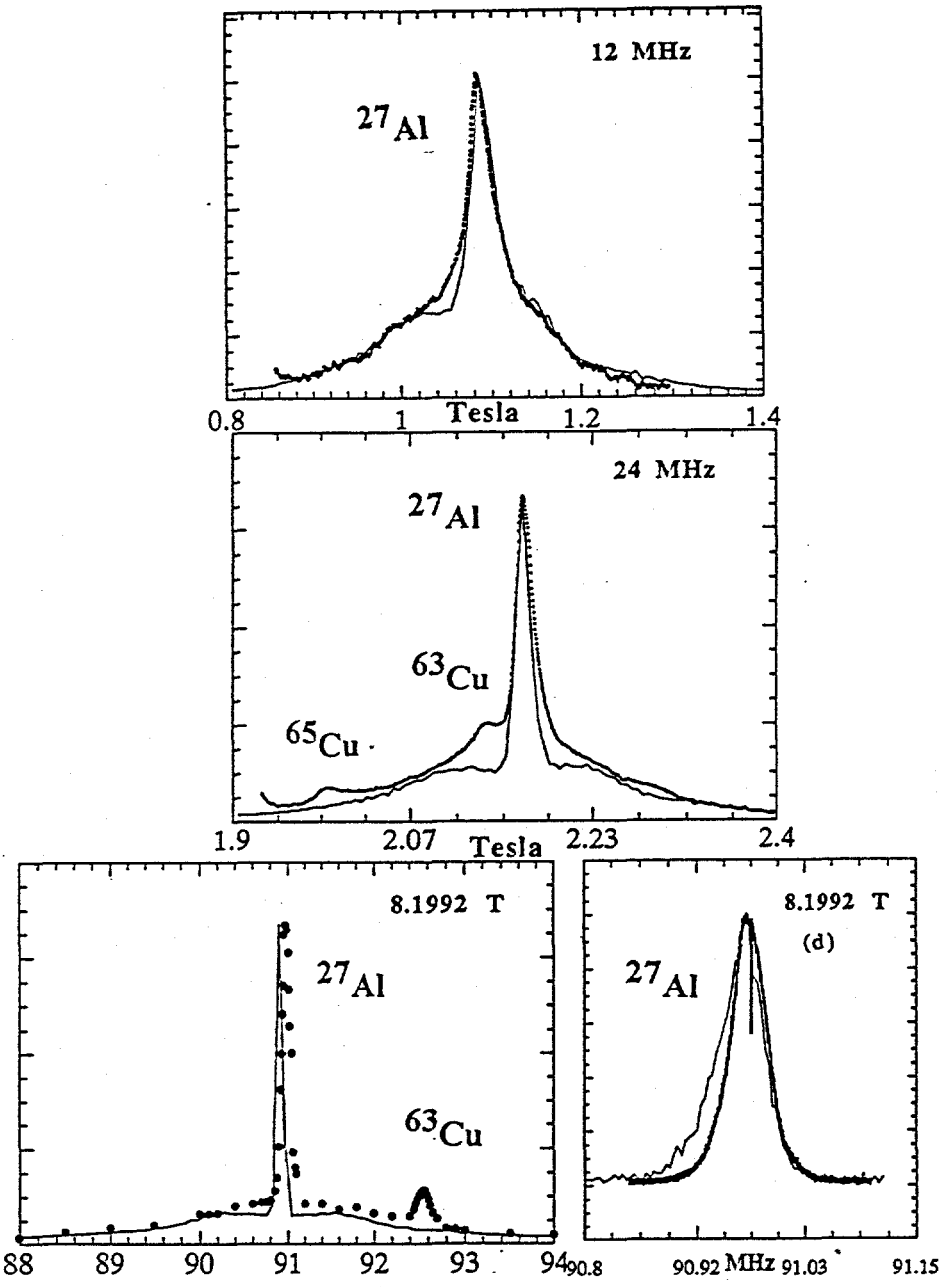

Fig. 5.8 Data and simulation for ^{27}Al NMR line in $Al_{65}Cu_{23}Fe_{12}$ quasicrystal at 77 K and three different resonance conditions. The heavy line is the data, the light line is the simulation. The parameters used in the simulation are: $\overline{\nu_Q}$=1.8 MHz; $\sigma = \overline{\nu_Q}/3$; η=0,0.1,0.2,...,0.5. (a) field scan at 12 MHz; (b) field scan at 24 MHz; (c) frequency scan at 8.2 T; (d) comparison of central line Fourier transform spectrum at 8.2 T with simulation.

2. ^{27}Al NQR

^{27}Al NQR data for batch #1 samples are shown in Fig. 5.9. As discussed previously, an I = 5/2 nucleus such as aluminum should have a $\pm 5/2 \leftrightarrow \pm 3/2$ transition at a frequency given approximately by $2\nu_Q$, which in this case of the batch #1 samples should be $\approx$ 4 MHz. The detection of an NQR signal at this frequency is confirmation that the quadrupole interaction is dominant in determining the energy levels of the nuclei. That the spectra in 5.9(a) and (b) are very similar is an indication that the distributions of electric field gradient tensor components within the two alloys are much alike. That the NQR spectrum is several megahertz wide indicates a distribution of electric field gradient tensors, due either to defects and/or impurities, or to a distribution of non-equivalent sites.

3. ^{27}Al NMR in AlPdMn single grain

The measurements discussed have all been on powder samples, primarily out of convenience: powders increase the filling factor of the sample coil, and the surface area to volume ratio, leading to improved signal to noise ratio. The drawback, however, is a loss of information concerning the EFG principal axis system axis orientations at the nuclear site, important in understanding the nature of the local environment. A single grain sample would provide this information, but must be large enough to make NMR measurements feasible. For quasicrystals, AlCuFe forms single grains on a length scale of $\approx$ 100 μm, to small for NMR measurements. However, recent work by Kycia et al. has led to AlPdMn single grains with dimensions on the order of centimeters [24].

^{27}Al NMR spectra in a single grain AlPdMn sample were studied as a function of the angle α between the between the 2-fold symmetry axis orientation and the static magnetic field. The purpose was to determine the directions of the EFG principal axes, and Fig.s 5.10(a) and (b) show the spectra at three different α values for a single grain $Al_{70}Pd_{21.5}Mn_{8.5}$. Unlike what one sees in a single crystal, where the satellites shift as the orientation of the

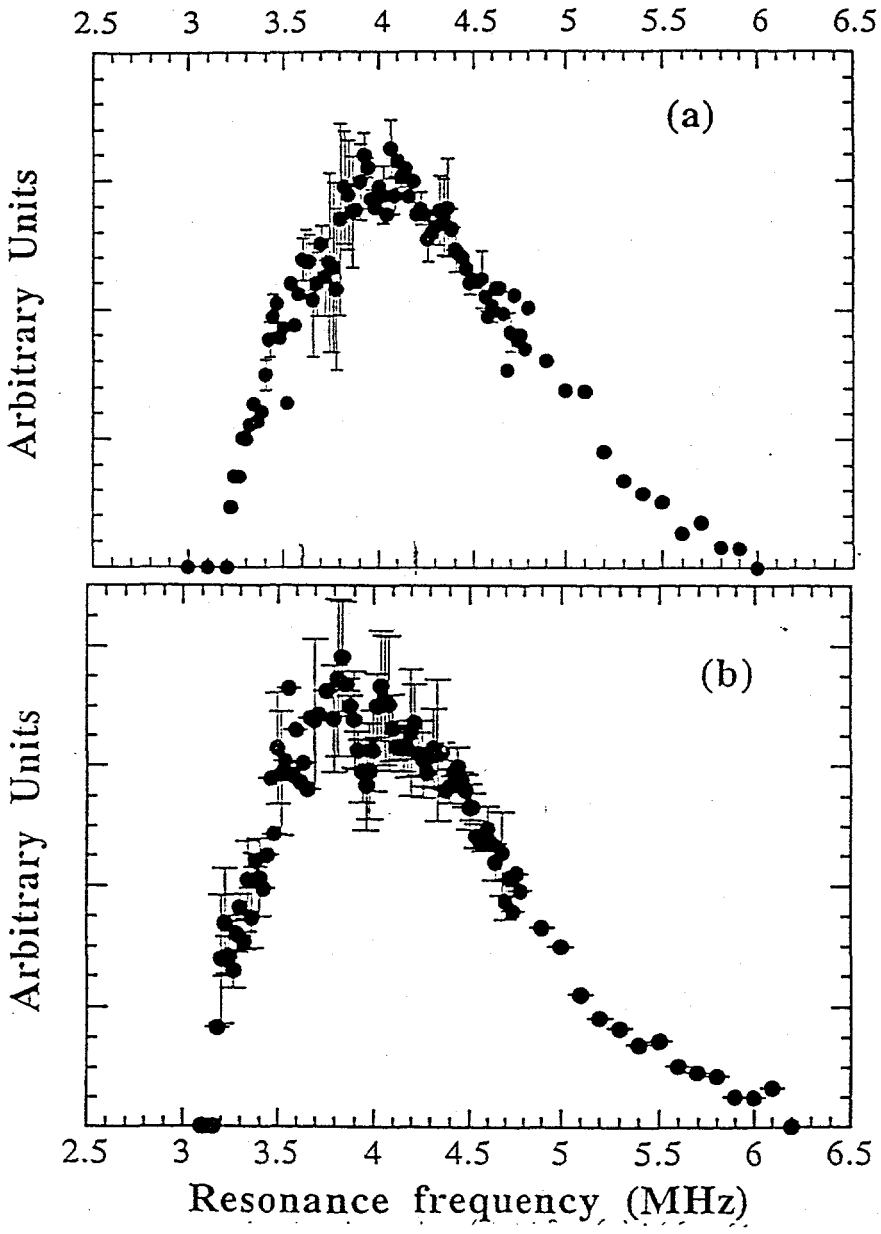

Fig. 5.9 ^{27}Al NQR spectra for two quasicrystals: (a) $Al_{70}Cu_{15}Ru_{15}$; (b) $Al_{65}Cu_{23}Fe_{12}$ at 4.2 K. Vertical axes were rescaled by ν_R to correct for the Boltzmann distribution.

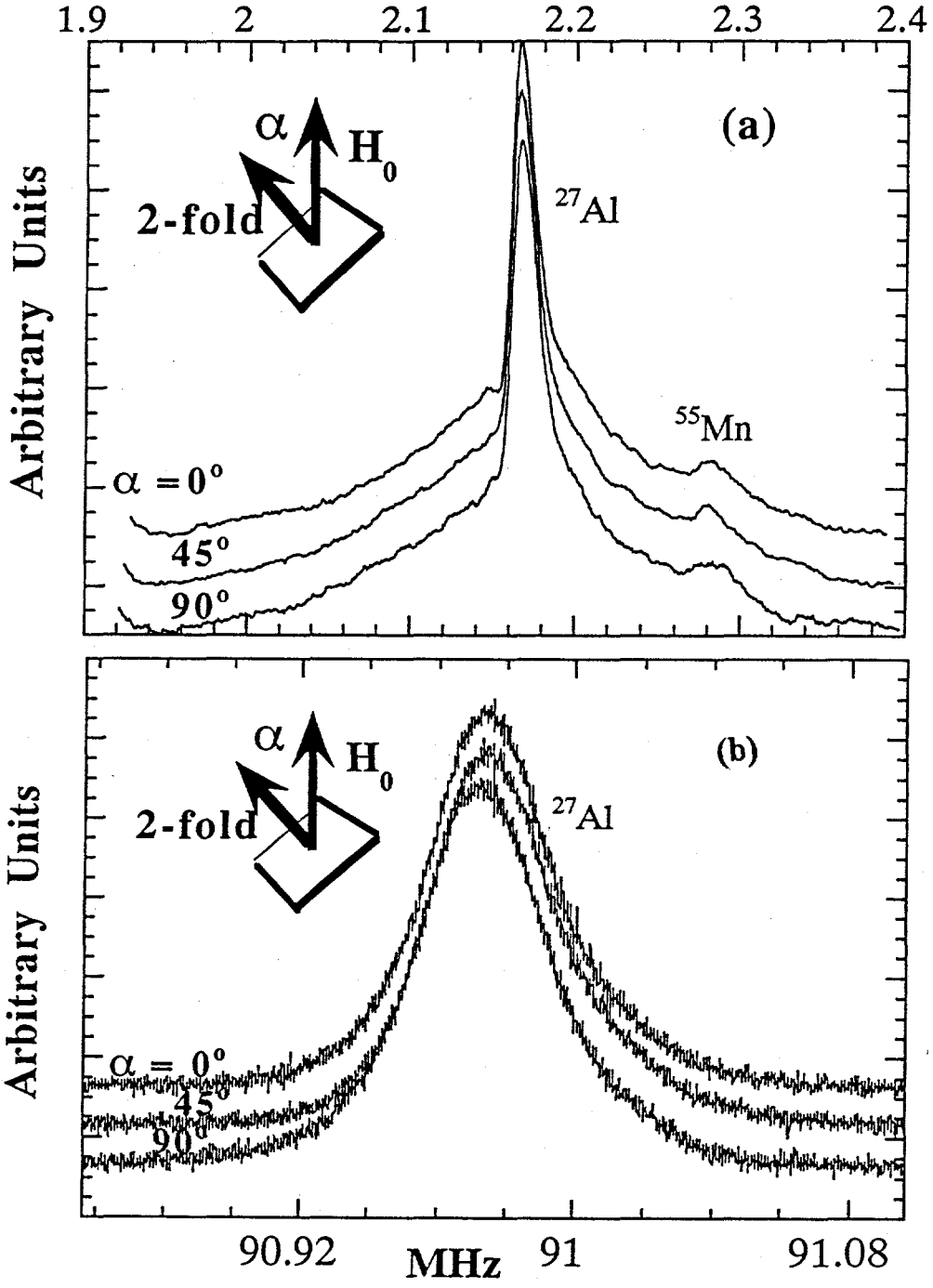

Fig. 5.10 ^{27}Al NMR spectra of $Al_{70}Pd_{21.5}Mn_{8.5}$ single grain sample taken at 77 K: (a) carrier frequency is 24 MHz; central line and quadrupole satellites for $\alpha = 0°$, 45°, 90° ; (b) static field is 8.2 T; central line by Fourier transforming a half echo for $\alpha = 0°$, 45°, 90°.

crystal changes with respect to the static field (see Fig. 3.2), no shift in the satellites of the single grain quasicrystal occurs. No change occurs in the resonance frequency of the central line either, as seen in the 8.2 T, Fourier transform spectra of the central lines of Fig. 5.10(b), which might be expected since, for nuclei with a strong quadruple interaction, the energy levels of the central line are also orientation dependent.

Finally, Fig. 5.11 shows a comparison between the single grain sample and a powder sample of AlPdMn of nominally the same composition. There is only a slight difference between the spectra, which we attribute to differences in purity and preparation. The comparison is in striking contrast with that of ordinary crystals (see Fig. 3.2 and 3.3). The spectra suggest a distribution in the directions of the EFG principal axes in the single grain sample which rivals that of a powder.

B. Analysis and Interpretation of Experimental Results

We proceed to discuss the above data in terms of the distributions of ν_Q, η, K_{iso}, K_{an}, and ε.

1. Quadrupole Interactions and Knight shift from ^{27}Al NMR line Simulation

Several previous NMR investigations indicated a distribution of local environments [4 - 10], and those of Warren [4] and Drews [9] have reported studies of the underlying distribution of quadrupole interactions using NMR lineshape simulation programs. The specifics of such routines are discussed in Appendix 1 and Chapter 4; conceptually, their purpose is to calculate a composite NMR powder pattern due to a distribution of non-equivalent sites (see Fig. 3.4, for example). The usefulness of a model distribution may then be judged based on how well the simulation and data agree. However, Warren comments that fit parameters determined in this way should only be taken as indicative, due to the large

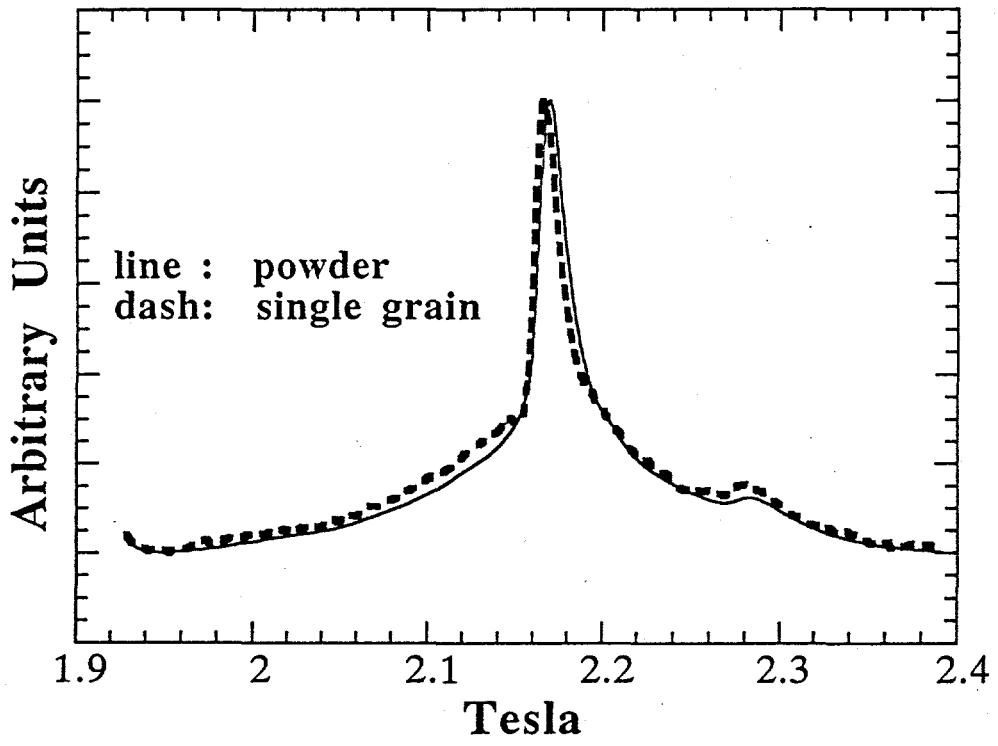

Fig. 5.11 ^{27}Al NMR spectra of $Al_{70}Pd_{21.5}Mn_{8.5}$ single grain and powder sample of the same nominal composition. Data were taken at 24 MHz, 77 K, and the single grain was oriented at $\alpha = 0°$

number of fit parameters involved. Drews et al. extend the method of Warren, placing a more stringent criterion on the acceptability of a proposed model distribution by requiring that the distributions yield acceptable agreement with data at three resonance conditions. The resonance conditions chosen by Drews et al. were imposed by fixed carrier frequencies of 11.10 MHz, 17.80 MHz, and 46.69 MHz.

Measurements at high field or frequency are important for accurate NMR line simulations when quadrupolar are being studied, because the second order quadrupole interaction results in a narrowing of the central line. The line position is therefore better determined under such conditions, making apparent the need for a field study of the NMR line to span a wide range of fields, with the highest upper limit possible.

For this reason, our investigation includes spectra obtained at fixed carrier frequencies of 12 MHz, 24 MHz, and a fixed field of 8.2 T, which corresponds to a unshifted ^{27}Al resonance frequency of 90.96 MHz. This increase in the upper-limiting field allowed us to reduce to aluminum linewidth to 50 kHz, making Fourier transform spectroscopy possible, resulting in much greater precision in determining the line position, and a more stringent criterion than used by Drews to determine the acceptability of a model distribution.
What is now to be determined is the nature of the distribution of the local environments, via the distribution of the EFG tensor parameters $\nu_Q \propto V_{zz}$ and η. Of primary importance is: (1) whether the distribution of ν_Q and η is continuous or discrete, i.e. whether the structure of the quasilattice is such that nuclei find a few non-equivalent sites with ν_Q values that may be resolved; and (2) whether the non-equivalent sites occur in the structure with the same probability, i.e. with a uniform distribution. Drews et al. based their simulations on the assumption that each non-equivalent site occurs with the same probability, and they tested both discrete and quasicontinuous distributions in their study of quasicrystalline $Al_{63}Cu_{24.5}Fe_{12.5}$. They reported better fits to the data with the discrete distribution, and Fig.

5.12 shows their NMR simulations at three resonance frequencies. That Drews et al. reported difficulty obtaining fits to all three data sets, as is evident in Fig. 5.12(a), is qualitatively consistent with the NQR data of Fig. 5.9. There one sees that the $\pm 5/2 \leftrightarrow \pm 3/2$ transition, which may be thought of as the distribution of $2\nu_Q$ values to a fair approximation (see Chapter 3), appears neither to be uniform, as Drews assumed, nor to exhibit any fine structure that might be interpreted as a discrete ν_Q component. On the contrary, from the NQR data a non-uniform distribution of quadrupole resonance frequencies is unmistakable, implying that not all such frequencies are equally probable.

We used the NMR lineshape simulation program to test model distribution of the parameters ν_Q, η, K_{iso}, K_{an}, and ε in the light of the above discussion, and found that one could obtain reasonably good fits at all resonance conditions. First we discuss the distributions of η and ν_Q, and then the distributions of K_{iso}, K_{an}, and ε.

We chose a distribution of ν_Q values qualitatively consistent with the NQR distribution, specifically a quasicontinuous gaussian distribution given by

$$h(\nu_Q) = \frac{1}{\sigma\sqrt{2\pi}} e^{-\frac{(\nu_Q - \overline{\nu_Q})^2}{2\sigma^2}} \qquad (5.1)$$

where $\overline{\nu_Q}$ is the mean value of the distribution. The distribution was modeled by 60 equally spaced values of ν_Q over the range from $\overline{\nu_Q}$-5σ to $\overline{\nu_Q}$+5σ. The distribution of η values was taken to be uniform, and, to reduce the number of loops required in the simulation program, only the η values 0, 0.1, 0.2, ..., 1.0 were allowed.

Regarding the distribution of Knight shift tensor components, we assumed only K_{iso} had appreciable magnitude. The justification for this is as follows. The anisotropic part of the Knight shift K_{an} has the effect of broadening the NMR line proportionally with the resonance frequency ν_R, and arises from non-s band electrons near the Fermi energy [35]. When both

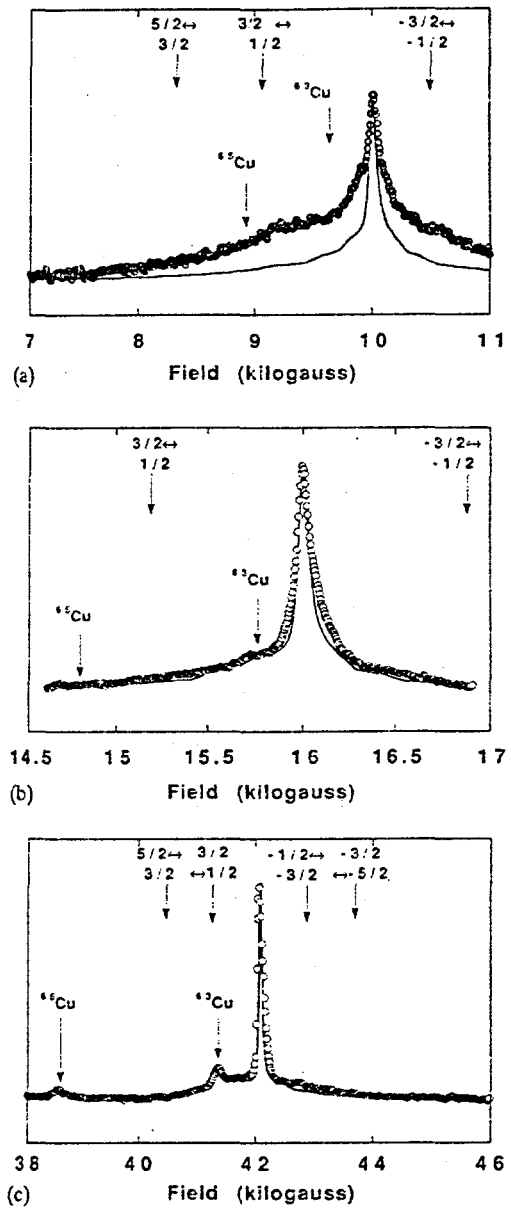

Fig. 5.12 Data (circles) and simulations (solid lines) for ^{27}Al in $Al_{63}Cu_{24.5}Fe_{12.5}$, taken from Drews et al. ref. [9]. Simulations were generated based on values $\eta = 0.75$ and $\nu_Q = 0.3, 0.6, 0.9, \ldots, 1.8$ MHz at (a) 11.10 MHz and 77 K; (b) 17.80 MHz and 77 K; (c) 46.69 MHz and 50 K.

quadrupole and Knight shift effects exist simultaneously, the two mechanisms compete, and the total line width of the ^{27}Al central line may be described by [53]

$$\Delta = \frac{a}{\nu_R^2} + b\nu_R \qquad (5.2)$$

where the exact values of the constants a and b will depend upon the distributions of the quadrupole coupling constants ν_Q, and the Knight shift tensor components K_{an} respectively, assuming the intrinsic dipolar width to be negligible. The above equation does not assume any particular symmetry for the nuclear sites. The experimental results are shown in Fig. 5.13, for all the batch #1 samples, in a plot of Δ/ν_R vs. $1/\nu_R^2$. Although only three points are available for comparison, one can see that the above equation is in agreement with the experimental points. The main point is that the intercept b is very nearly at the origin, leading to the conclusion that the mean value of the anisotropic Knight shift is negligibly small. For this reason, in the simulation we may neglect ε and K_{an}, reducing the Knight shift parameters to K_{iso}.

Based on the above model, the lineshape simulations were obtained by first determining the mean value and second moment of the ν_Q distribution by trial and error. It was found that when the second moment satisfied $\sigma/\overline{\nu_Q} \approx 1/3$, the NMR line simulation became featureless like the data. In addition, the η values 0, 0.1, 0.2, ..., 0.5 seemed to work slightly better than simulations for η = 0.5, 0.6, ... , 1.0, though the difference was not dramatic.

Having found good agreement when the above distributions were used, we used the NMR line simulations to extract $\overline{\nu_Q}$ and K_{iso}. A library of simulations at 12, 24 MHz and 8.2 T for different values of $\overline{\nu_Q}$ were compiled. These simulations were then compared to spectra to determine a $\overline{\nu_Q}$ that worked at all fields. To obtain the isotropic Knight shift K_{iso} using the NMR line simulations, we made two successive approximations where, as a first approximation, K_{iso} was set equal to zero. The simulation for the Al central line was then generated for a static field of 8.2 T, and the simulation was compared to Al FT spectra at 8.2

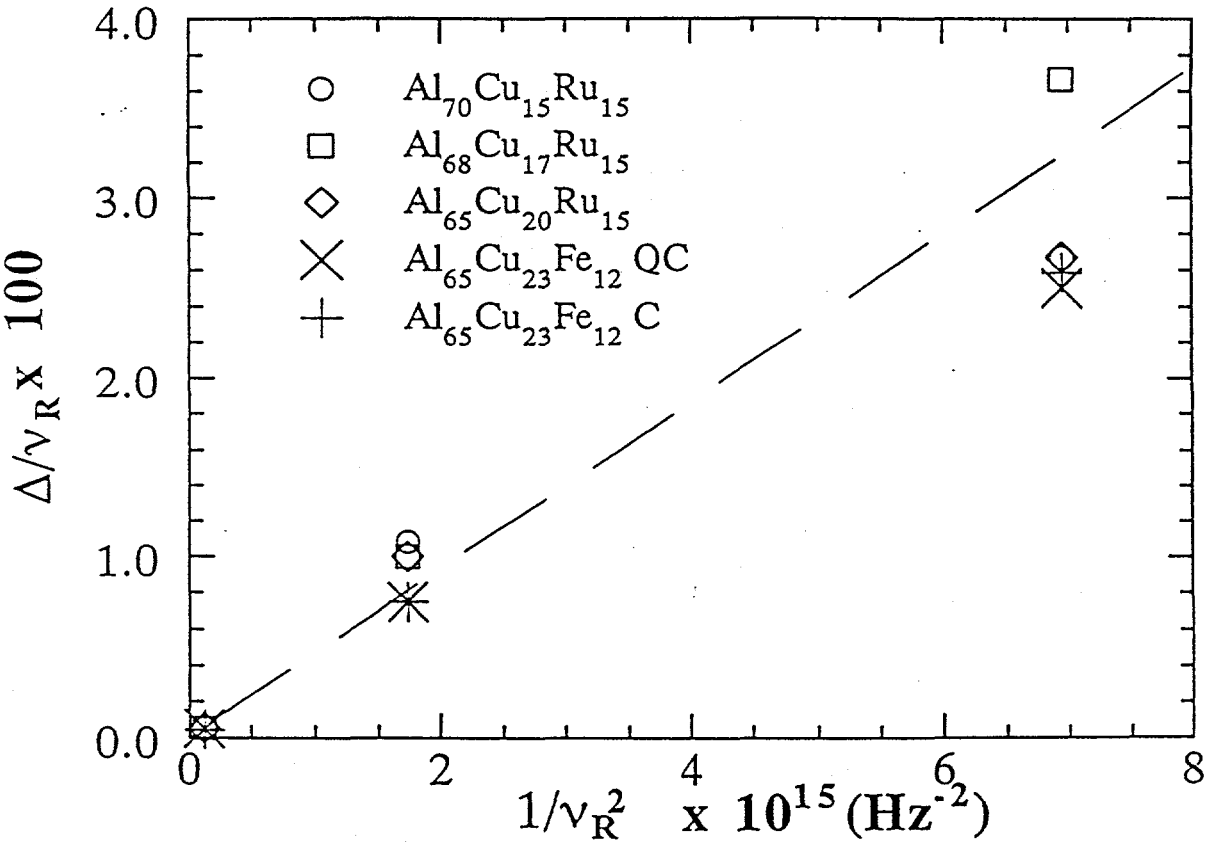

Fig. 5.13 Δ / ν_R vs. $1/\nu_R^2$ for ^{27}Al in the batch #1 AlCuFe and AlCuRu samples, where Δ is the FWHM taken from the data of Fig.s 5.4 - 5.8.

Table 5.1 ^{27}Al K_{iso} and $\overline{\nu_Q}$ values for batch #1 samples, determined by an NMR lineshape simulation routine applied to data in Fig. 5.4 - 5.8

Sample	$\overline{\nu_Q}$ (MHz)	K_{iso} (%)
$Al_{70}Cu_{15}Ru_{15}$	2.1±0.1	0.026±0.004
$Al_{68}Cu_{17}Ru_{15}$	2.1±0.1	0.024±0.004
$Al_{65}Cu_{20}Ru_{15}$	2.2±0.1	0.024±0.004
AlCuFe C	1.9±0.1	0.016±0.004
AlCuFe QC	1.8±0.1	0.016±0.004

Tesla. By shifting the simulation $\Delta\nu$ until it lay upon the data peak, we obtained for the second approximation the value $K_{iso}=\Delta\nu/\nu$, where ν is the center of the data peak. The values of $\overline{\nu_Q}$ and K_{iso} for AlCuFe and AlCuRu are given in Table 5.1 The uncertainty of $\overline{\nu_Q}$ was determined by noting the minimum amount by which $\overline{\nu_Q}$ in the NMR lineshape simulation need be changed to get a perceptible difference in the simulated line width, and the uncertainty of K_{iso} was determined by the uncertainty of the spectrum maximum of the Fourier transform spectrum of Fig. 5.4 - 5.8(d).

The results of the fits are presented in Fig. 5.4 - 5.8, where the simulated line is represented by a solid line, and the data given by filled circles. The reasonably good fits at all resonance conditions are therefore indication that a gaussian distribution of ν_Q is a reasonable approximation to the actual distribution, given approximately by the NQR spectrum. However, the fits do show occasional divergences from the data, particularly in the satellites. We attribute these differences to the fact that the real distribution of ν_Q is not actually a gaussian: the intensity of the NQR spectrum appears to decrease with frequency

less rapidly than one would expect for a gaussian, and the NQR spectrum appears somewhat asymmetric. It is believed that these minor differences between the simulated and actual distributions induce no significant error in the average parameters K_{iso} and $\overline{\nu_Q}$ of Table 5.1

2. Quadrupole Interactions from the ^{27}Al NQR Lineshape

Having discussed the nature of the underlying electric field gradient distribution, we now discuss the structural aspects of quasicrystals that might result in the NQR spectrum of Fig. 5.9.

The most striking aspect of the AlCuFe and AlCuRu NQR spectra are that their widths are much larger than what one expects from strains, defects, or substitutional impurities. This may be seen by comparing the underlying distributions of the total electric field gradient V_{zz}^{tot} in quasicrystals with those of other crystalline systems. We assume that to a good approximation the NQR resonance frequency ν_R is proportional to the total electric field gradient V_{zz}^{tot} (Chapter 3), and therefore that the distribution of V_{zz}^{tot} underlying the measured distribution of ν_R may be characterized by the ratio $\sigma/\overline{\nu_R}$, where σ is the NQR spectrum half-width at half-maximum, and $\overline{\nu_R}$ is the mean resonance frequency.

For the ^{27}Al NQR spectra of Fig. 5.9, one finds that $\sigma/\overline{\nu_R} \approx 1/5$. We choose for comparison various nuclei in metallic systems where defects and impurities are known to contribute significantly to the NQR line width. For the metals indium and rhenium, one finds $\sigma/\overline{\nu_R} \approx 1/26$ for ^{187}Re NQR [50], and $\sigma/\overline{\nu_R} \approx 1/63$ for ^{115}In NQR [54]. Examples in alloys systems are numerous, and we choose for comparison the NQR spectra in two high temperature superconductors, which are well known to be poor metals and highly disordered structurally. For ^{63}Cu NQR in $YBa_2(Cu_{1-x}M_x)_3O_7$, for the case of slight doping with Zn or Ni, one finds that the ratio is only $\sigma/\overline{\nu_R} \approx 1/79$ [55], and that, for ^{139}La NQR measurements in Sr doped La_2CuO_4, the ratio is $\sigma/\overline{\nu_R} \approx 1/40$ [56].

Efforts to obtain a direct comparison through ^{27}Al NQR were complicated by the lack of such reports in the literature. Though reports of ^{27}Al NQR are rare, MacLaughlin [57] reports that the $\pm 5/2 \leftrightarrow \pm 3/2$ ^{27}Al NQR spectrum in Gd doped $LaAl_2$ Laves phases, due to the non-cubic aluminum sites in the structure, occurs at 1.48 MHz and has a full width at half maximum that depends upon the Gd concentration x, the small static magnetic field H_0 ($\leq$ 150 G) as

$$2\sigma = 2(A + Bx + CH_0) \qquad (5.3)$$

where A = 13 ± 3 kHz, B = 1 ± 0.4 kHz/at.%, and C = 1.4 ± 0.6 kHz/G [57]. If one takes 2 σ as indicative of the ^{27}Al NQR intrinsic line width due to defects and strains, one may then make direct comparison of this line with the NQR line of the quasicrystals. Calculating 2σ under the conditions of the NQR experiment of Fig. 5.9, where one has x = 0 and H_0 = 30 G, one finds $2\sigma \approx 100$ kHz, which is much less than the FWHM of 1.5 MHz of the Fig. 5.9 NQR data.

Therefore, the above comparisons suggest that the width of the broad NQR spectrum in the stable icosahedral quasicrystals cannot be explained by the presence of lattice defects, strains, or impurities. This raises the question of whether the structure of the quasilattice itself might result in the wide distribution of electric field gradients, through a multiplicity of non-equivalent sites.

3. Electric Field Gradient Model Calculation and the Problem of the Atomic Positions

We approached this problem through a simulation of the NQR data based on a structural model for the quasicrystal. NQR investigations, in systems where ionic positions and charges are well known, typically present analysis of the NQR spectrum through a calculation of the electric field gradients at the nuclear sites. For quasicrystals, this procedure is complicated by the fact that the atomic positions are not known. However, one may gain further insight into the quasicrystalline NQR data by calculating the distributions of V_{zz}^{tot} and η for the ^{27}Al sites

in a crystalline approximant, and then calculating the distribution of quadrupole resonance frequencies ν_R.

As discussed previously, the crystalline approximants are crystals whose local order, and therefore atomic positions, closely approximate those of the quasicrystal. Such structures are themselves quite complicated. The atomic positions of an AlCuFe 1/1 approximant have recently been discussed by Cockayne et al. [58], and contains 128 atoms in its unit cell. We chose this structure as a reasonable approximation to the actual local structure within AlCuFe and AlCuRu quasicrystals.

The characteristics of the approximant we used are as follows: the structure is a 1/1 approximant with stoichiometry $Al_{80}Cu_{32}Fe_{16}$, cubic symmetry, 128 atoms/cell, and lattice constant a = 12.30 Å. The atomic positions may be determined for all 128 atoms in the unit cell from the atomic positions of the non-equivalent sites given in Table 5.2, and Appendix 2 describes in detail how the coordinates were calculated. The main structural feature is a

Table 5.2 Atomic positions for a structural model of an AlCuFe(Ru) approximant. Coordinates are in units of the lattice parameter a = 12.30 Å. Taken from Cockayne et al. ref. [58]

	Site	*x*	*y*	*z*
Fe	4(a)	0.843	0.843	0.843
Fe	12(b)	0.540	0.348	0.672
Al	4(a)	0.049	0.549	0.951
Al	12(b)	0.030	0.541	0.346
Al	12(b)	0.226	0.857	0.475
Al	12(b)	0.247	0.850	0.833
Al	12(b)	0.732	0.029	0.159
Cu	4(a)	0.336	0.336	0.336
Cu	12(b)	0.036	0.836	0.150
Al	4(a)	0.543	0.043	0.457
Cu	12(b)	0.554	0.022	0.858
Al	12(b)	0.732	0.343	0.336
Al	12(b)	0.230	0.533	0.635
Cu	4(a)	0.348	0.848	0.652

network of Bergmann clusters (see Fig. 5.14), consisting of a central copper atom surrounded by an approximately icosahedral shell of 9 aluminum and 3 iron atoms, and a larger, approximately dodecahedral shell of 13 copper and 7 aluminum atoms. Each cluster is joined to six other clusters through a sharing of a pair of copper atoms in the dodecahedral shell.

In order to calculate the quadrupole resonance frequencies of the NQR spectra based on a given structural model, one must determine the electric field gradient at the sites of the resonant nucleus. In metallic systems, the electric field gradient has contributions that arise from the ions within the structure of the lattice, denoted V_{zz}^{lat}, as well as from the valence or conduction band electrons, denoted V_{zz}^{el}. As a result, one may write the total electric field gradient at the nuclear site as [59], [60]

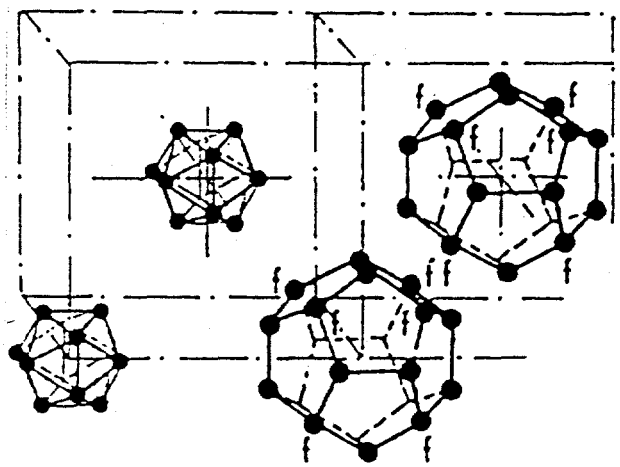

Fig. 5.14 The structure of the approximant is based on clusters with inner icosahedral, and outer dodecahedral shells. The atomic decoration is described in the text.

$$V_{zz}^{tot} = V_{zz}^{latt}(1-\gamma_\infty) + V_{zz}^{el} \qquad (5.4)$$

The factor $(1-\gamma_\infty)$, the Sternheimer anti-shielding factor, is an enhancement factor that arises from the distortion of the spherical, inner-electronic shells of the atom by the electric field gradients of the lattice ions. Since the inner shell electrons are the charges closest to the nucleus, this effect results in significant enhancement of the lattice gradient at the nuclear site. The lattice term may be determined in a point charge model for the ionic charges. Calculating the total gradient V_{zz}^{tot} from first principles, therefore, requires knowledge not only of the atomic positions, but also of the valence band wave functions. For quasicrystals, the lack of a unit cell makes band structure calculations difficult [3 DiVincenzo], and therefore complicates a first principles theoretical approach to modeling the NQR spectrum. To circumvent the difficulties inherent in a first principles approach, we proceeded to obtain the electronic contribution V_{zz}^{el} semi-empirically, based on knowledge of the calculated V_{zz}^{latt} in the point charge approximation, and on the V_{zz}^{tot} determined from the NQR data of Fig. 5.9. Based on the value of the electronic contribution, quadrupole resonance frequencies were then calculated. The details are as follows:

(1) In many metals and alloy systems, the electronic contribution to the gradient is normally 2-3 times larger than the lattice contribution, and of opposite sign [60]. For this reason, we chose to write the total electric field gradient

$$\left|V_{zz}^{tot}\right| = \left|V_{zz}^{el}\right| - \left|V_{zz}^{latt}\right|(1-\gamma_\infty) \qquad (5.6)$$

The NQR resonance frequency ν_R for $\pm 5/2 \leftrightarrow \pm 3/2$ transitions could then be written (Chapter 3)

$$\nu_R = 2\nu_Q g(\eta) \qquad (5.7)$$

where, $\nu_Q \equiv 3eQ\left|V_{zz}^{tot}\right|/20h$, and where for ^{27}Al nuclei $Q = 0.14\times10^{-24}$ cm^2, and $(1-\gamma_\infty) =$ 3.3. An expression for the average ν_R, $\overline{\nu_R}$, obtained from the NQR spectrum could then be written as a sum of lattice and electronic contributions

$$\overline{\nu_R} = \overline{\nu_R^{el}} - \overline{\nu_R^{latt}}(1-\gamma_\infty) \tag{5.8}$$

where $\overline{\nu_R^{latt}} = 3eQ\overline{|V_{zz}^{latt}|}/20h$. Therefore, once $\overline{\nu_R^{latt}}$ is known from calculations based on a structural model, and $\overline{\nu_R}$ is determined directly from the intensity distribution $I(\nu_R)$ of the NQR spectrum of Fig 5.9 by

$$\overline{\nu_R} = \frac{\int \nu_R I(\nu_R) d\nu_R}{\int I(\nu_R) d\nu_R} \tag{5.9}$$

the term $\overline{\nu_R^{el}}$ may be directly determined.

(2) To calculate the lattice contribution $\overline{\nu_R^{latt}}$ we calculated the distribution of ν_R^{latt} based Cockayne's structural model and an ion point charge approximation (see also Appendix 2). To eliminate boundary effects in the electric field gradient calculation, the original cubic unit cell of 128 atoms and lattice constant a = 12.3 Å was duplicated and then translated to create a set of 27 identical cells, with the cell of interest at the center. The electric field gradient tensor, given by

$$V_{ij}^{latt} = \sum_k \frac{eZ_k}{r_k^3}\left(\frac{3x_i x_j}{r_k^2} - \delta_{ij}\right)$$

where x_i are the components of the displacement vector between the Al nucleus at which the electric field gradient is to be calculated, and the ions of the lattice with charge Z_k, was then calculated at each Al site in the central cell. The summation was performed over ions within a sphere of radius R < a, and for a particular charge assignment for the Al, Cu, and Fe(Ru) ions. The electric field gradient tensor components were diagonalized to yield the largest component V_{zz}^{latt}, $\eta \equiv \frac{V_{xx}^{latt} - V_{yy}^{latt}}{V_{zz}^{latt}}$, and the angle θ between the z-axis of the EFG principal axis system and the z'-axis of the unit cell reference frame defined in the model for the approximant.

While it is reasonable to assume that the valence assignments for Al and Cu are the same as normally found in metals, namely Al^{3+} and Cu^{1+}, the valence assignment for the transition

metal is less certain due to the uncertain d-shell band structure in the alloy. For this reason, we performed calculations assuming three different valences of the Fe(Ru) ion: 1+, 2+, and 3+. The distributions of V_{zz}^{latt}, η, and θ are shown in Fig.s 5.16, 5.17, and 5.18 respectively. One may notice that the overall distribution and means values of V_{zz}^{latt} are not extremely sensitive to the Fe(Ru) valence, though the details of the distribution are. We therefore chose one the three valence assignments for further analysis, specifically Al^{3+}, Cu^{1+}, $Fe(Ru)^{1+}$.

The bin widths in the V_{zz}^{latt} histogram reflect the uncertainty in the electric field gradient calculation. Since the electric field gradient is calculated out to only the fifth nearest neighbor shell, and the contribution due to the nth shell falls off as 1/r, we estimated the uncertainty to be about 15% of $500e/a^3$, the contribution due to the first coordination shell.

(3) We obtained the semi-empirical value of $\overline{\nu_R^{el}}$ based on the NQR data of Fig. 5.9(a). We found $\overline{\nu_R} = 4.31$ MHz, and $\overline{\nu_R^{latt}}(1-\gamma_\infty) = 1.05$ MHz based on the distribution of Fig. 5.16(a), giving

$$\overline{\nu_R^{el}} = \overline{\nu_R} + \overline{\nu_R^{latt}}(1-\gamma_\infty) = 5.36\ \text{MHz} \tag{5.10}$$

(4) Using the above value for $\overline{\nu_R^{el}}$, and assuming $\nu_R^{el} = \overline{\nu_R^{el}}$, one may write eqn. (5.7) as

$$\nu_R = 5.36\ \text{MHz} - \frac{3eQ}{10h}\left|V_{zz}^{latt}\right|(1-\gamma_\infty)g(\eta) \tag{5.11}$$

where all quantities, η and V_{zz}^{latt}, are known and presented in Fig.s 5.16 and 5.17. Based eqn. (5.11), we calculated the distribution of ν_R, and compared it directly to the NQR data, as shown in Fig. 5.19.

Having discussed the details of the electric field gradient calculation, we observe that semi-empirical value $\nu_R^{el} = 5.36$ MHz corresponds to an electric field gradient of $V_{zz}^{el} = 1.77 \times 10^{15}\ \text{esu-cm}^{-3}$, which is of the order of magnitude expected for the electric field gradient generated by a 3p-wave at the Al site. In fact, for a single 3p-electron in an atom one has [36]:

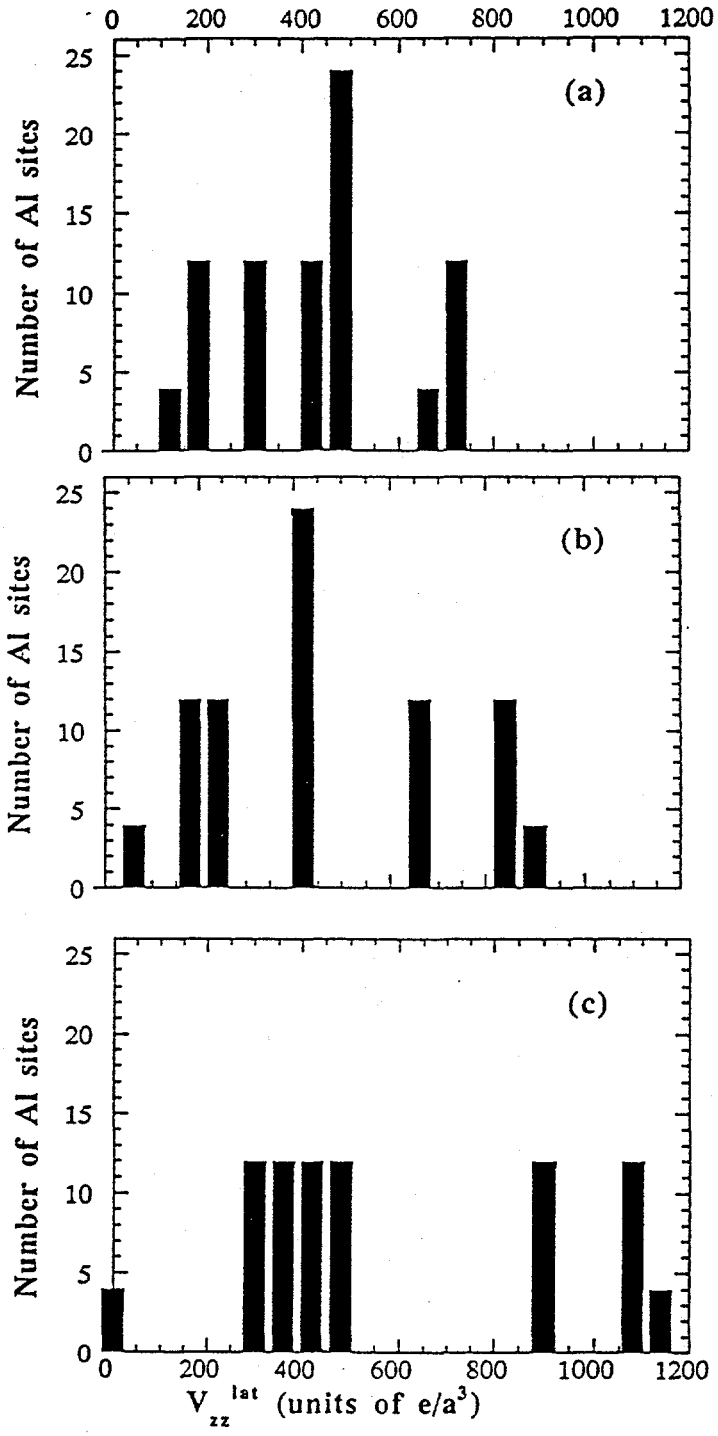

Fig. 5.16 Histogram of $\overline{V_{zz}^{latt}}$ for Al sites, in units of e/a^3, where a = 12.3 Å. The bin sizes are $60e/a^3$. The Al, Cu, and Fe(Ru) ions were taken respectively to have the charges: (a) 3, 1, 1; (b) 3, 1, 2; (c) 3, 1, 3.

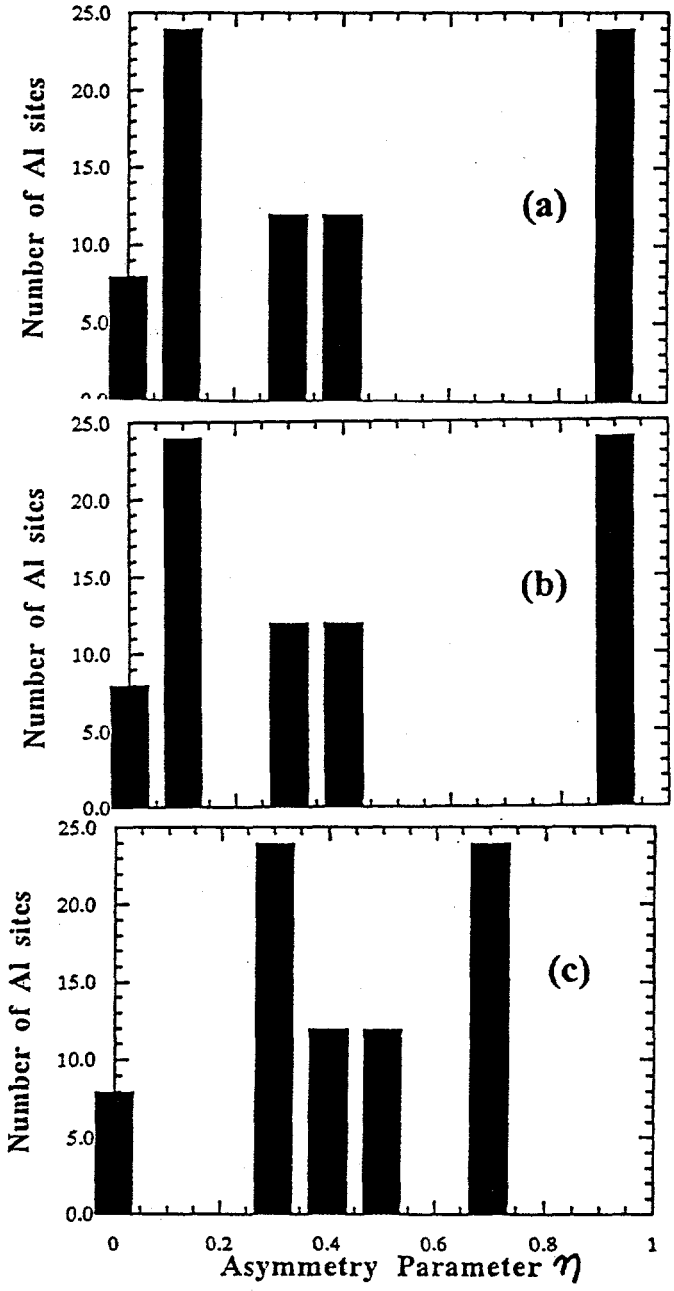

Fig. 5.17 Histogram of η for Al sites. The Al, Cu, and Fe(Ru) ions were taken respectively to have the charges: (a) 3, 1, 1; (b) 3, 1, 2; (c) 3, 1, 3.

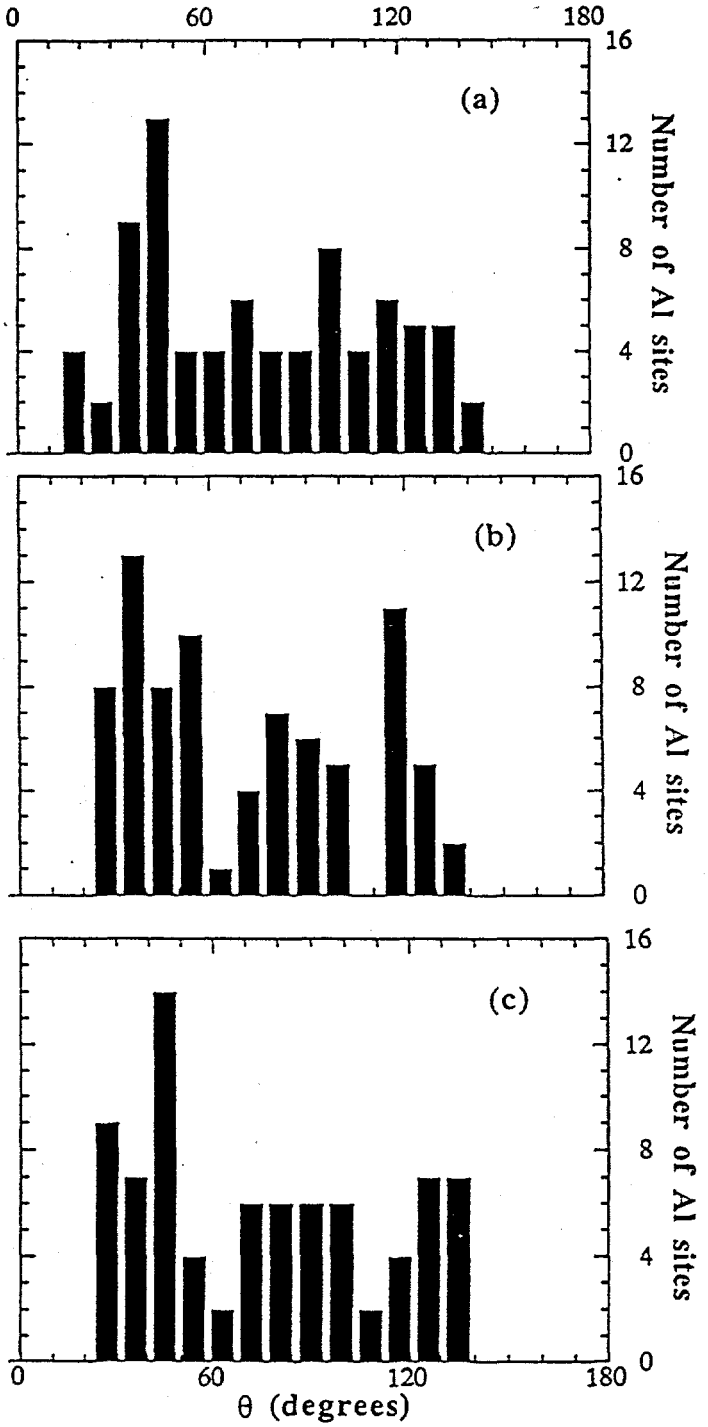

Fig. 5.18 Histogram of θ for Al sites. The Al, Cu, and Fe(Ru) ions were taken respectively to have the charges: (a) 3, 1, 1; (b) 3, 1, 2; (c) 3, 1, 3.

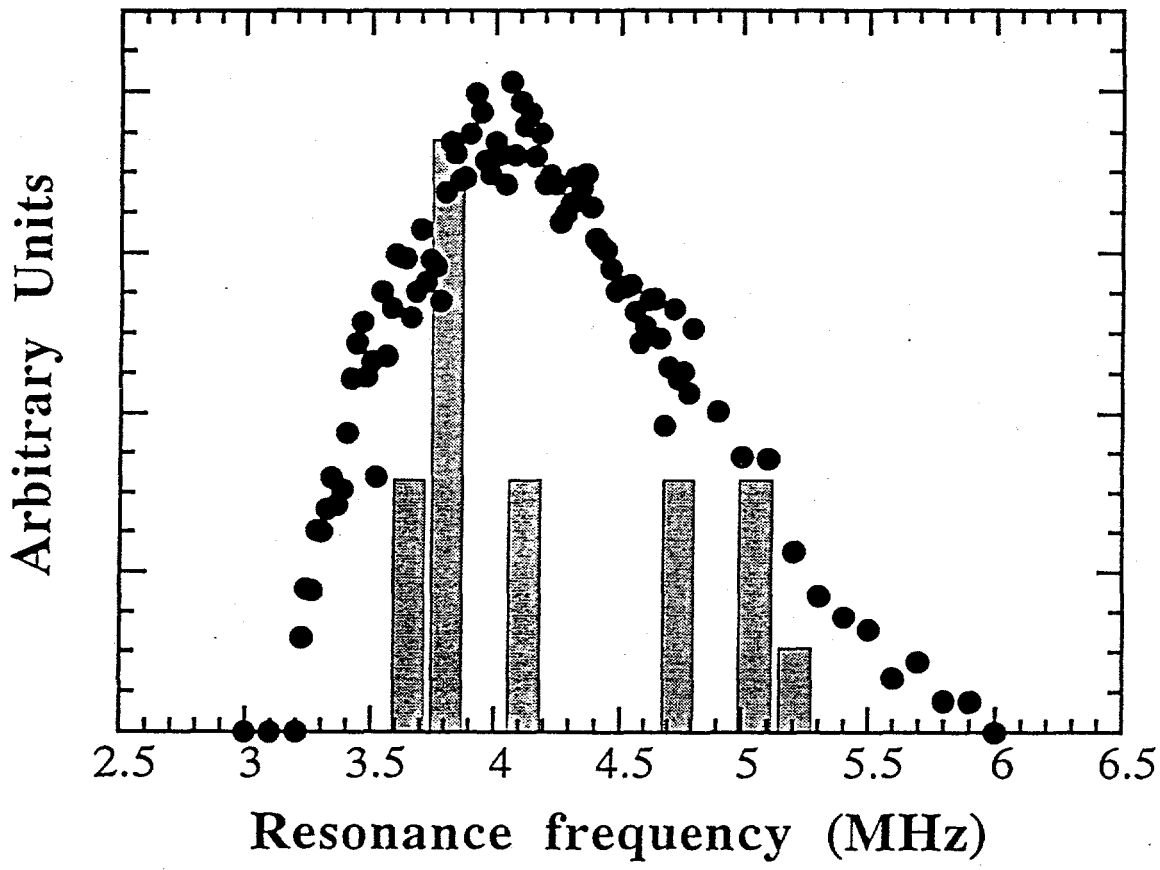

Fig. 5.19 Comparison of $\left|V_{zz}^{latt}\right|$ histogram for Al, Cu, and Fe(Ru) charges 3, 1, 1, based on Eqn. (5.11), superimposed on the NQR spectrum for $Al_{70}Cu_{15}Ru_{15}$. The heights of the histogram bars were rescaled to get the maximum of the histogram to agree with the experimental value. The different η values for the non-equivalent sites have been taken into account through the function $g(\eta)$ (see Chapter 3).

$$V_{zz}^{el} = \frac{4e}{5}\left\langle \frac{1}{r^3} \right\rangle \qquad (5.12)$$

By using $<1/r^3>=1.28/a_0^3$ (a_0=0.529 Å) as obtained from the hyperfine structure of optical spectra of Al neutral atoms [61] one has $V_{zz}^{el} = 3.3 \times 10^{15}$ esu - cm^{-3}. It is encouraging that the apparent spacial localization of the Al 3p-electrons is consistent with the poor metallic character of these quasicrystals.experimental value.

We now emphasize the main point of the above calculation: the above model assumes that the total electric field gradient at a nuclear site is determined primarily by the electronic contribution, and that the width of the NQR spectrum is determined by the distribution of V_{zz}^{latt} through the distribution of local environments. That the widths of the simulated and experimental NQR spectra of Fig. 5.19 are similar lends support to this picture.
However, the structural model of Cockayne, which we applied to the above calculation, does not result in a continuous distribution of ν_R values. Since the model has only 8 non-equivalent Al sites in its unit cell, this is perhaps an indication that, for modeling the NQR spectra of quasicrystalline structures, a higher order crystalline approximant is needed to obtain a simulated spectrum that appears continuous.

One may estimate the minimum number of non-equivalent Al sites in AlCuFe and AlCuRu quasicrystals, based on reasonable assumptions about the intrinsic linewidths for each non-equivalent site. We assumed that two mechanisms contributed to the intrinsic NQR linewidths: dipolar broadening due to interactions between nearest neighbors of like and unlike nuclei, and quadrupolar broadening due to defects and strains.

The dipolar contributions may be approximated by the Van Vleck second moment for powder lines, given by [35]

$$\overline{\Delta\omega^2} = \tfrac{3}{5}\gamma^4\hbar^2 I(I+1)\sum_k \frac{1}{r_{jk}^6} \qquad \text{(like nuclei)} \qquad (5.13)$$

$$\overline{\Delta\omega^2} = \tfrac{4}{15}\gamma_I^2\gamma_S^2\hbar^2 S(S+1)\sum_k \frac{1}{r_{jk}^6} \qquad \text{(unlike nuclei)} \qquad (5.14)$$

where γ_I and γ_S refer to the gyromagnetic ratios of the unlike spins I and S, and the summation is taken over all nearest neighbors k. Since the summation terms fall off as $1/r^6$, the summation is essentially determined by the first nearest neighbor distance. In addition, the larger nuclear spin I of Al will make I(I+1) for the Al-Al interactions more than twice as large as S(S+1) for the Al-Cu interactions. Therefore, one may neglect interactions from unlike nuclei. The Al-Al distances in Cockayne's structural model [58] average 2.5 Å, and one finds an average of 3 - 4 nearest neighbors. From eqn. (5.13) one finds a dipolar linewidth given by $2\sigma = \sqrt{\overline{\Delta\omega^2}} / 2\pi \approx 2$ kHz.

The intrinsic linewidth due to strain and defect induced quadrupolar broadening depends on the concentration of defects C, the average distance from the resonant nucleus to the defect d, and the nuclear properties of the resonant nucleus [59]. Assuming C and d of the cubic $LaAl_2$ Laves phases to be similar to the corresponding values in quasicrystals, one may use the ^{27}Al NQR linewidth of 100 kHz [57] found in these materials as and estimate of the intrinsic linewidth due to defects and strains.

By comparison of the dipolar and defect induced linewidths, one can see that the dipolar effects are negligible.

To place a lower limit on the number of non-equivalent aluminum sites, one notices that the lack of any resolvable fine structure in the NQR spectra of Fig. 5.9 indicates that the intrinsic linewidth due to each non-equivalent aluminum site is larger than the difference in frequency between neighboring resonance lines. Though setting a criterion for the resolvability of the component NQR lines is somewhat arbitrary, we took as a reasonable upper limit on the average separation between component NQR resonances the value $\delta/2$, where δ is the FWHM of the intrinsic linewidth due to defects and strains. Dividing the full frequency range of the distribution, Δ, by the separation between adjacent NQR resonance

lines, one gets an estimate on the number of component resonance lines n, and therefore the number of non-equivalent sites:

$$n \geq \frac{\Delta}{\delta/2} \tag{5.16}$$

For $\Delta = 2.5$ MHz from Fig. 5.9, and $\delta = 100$ kHz as discussed above, one gets $n \geq 50$ non-equivalent Al sites.

4. Distribution of EFG Principal Axis Orientations from ^{27}Al NMR in AlPdMn Single Grain

As mentioned earlier, the NMR spectra of the AlPdMn sample show no angular dependence in either the central lines or the satellites. This is qualitatively consistent with the distribution of electric field gradient principal axis orientations for Al sites in the AlCuFe(Ru) 1/1 approximant, shown in Fig. 5.18. The figure indicates that there exist several orientations for the principal axis systems at the aluminum sites. Intuitively, one only expects an angular dependence of the NMR line to be observed if a large fraction of the nuclei posses the same principal axes, thus favoring a particular direction. When no direction is favored, as indicated in Fig. 5.18, one expects no angular dependence of the NMR line.

We stress that a wide distribution of electric field gradient components, ν_Q and η, without a distribution of principal axes, is not sufficient to explain the lack of angular dependence, through a "washing out" of the structure of the powder pattern that might obscure shifts in the resonance frequencies. To test this possibility, we simulated the ^{27}Al NMR spectrum of the single grain assuming a distribution of ν_Q similar to that used for simulations in the AlCuFe and AlCuRu systems, and assuming only a fixed principal axis orientation with probability 1 (see Appendix 1). Fig. 5.20 shows that the shape of the simulated single grain NMR spectrum is markedly different from the single grain AlPdMn data taken at 24 MHz, seen in Fig.s 5.10 and 5.11. The simulation shows that the structure of the satellites is

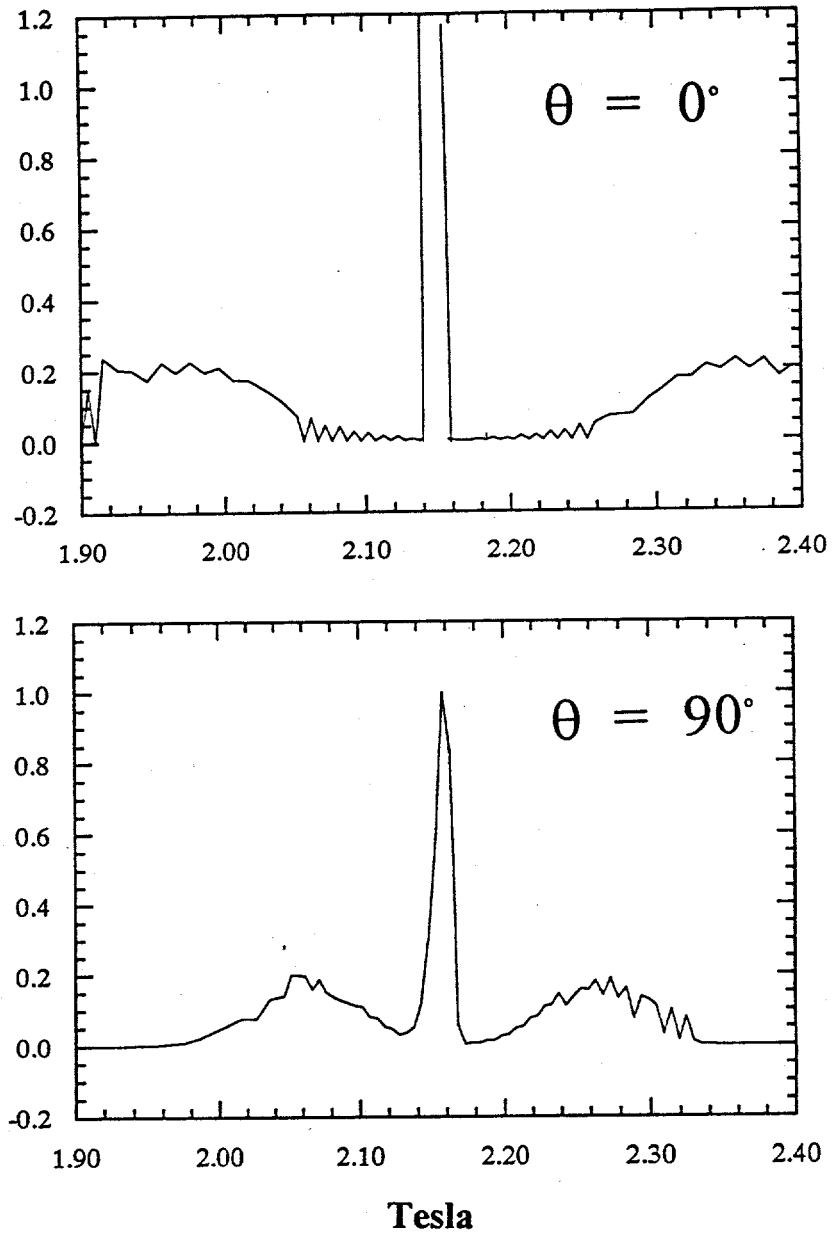

Fig. 5.20 Simulation for estimating shift in the ^{27}Al central line and satellites in the AlPdMn single grain quasicrystal. Parameters used in the simulation are: $\overline{\nu_Q}$=2.1 MHz; $\sigma = \overline{\nu_Q}/3$; asymmetry parameter values η=0 and a single principal axis system. The simulated spectrum is a field scan at 24 MHz for θ=0° and 90°, where θ is the angle between the principal axis system z-axis and the external field $\mathbf{H_0}$.

smoothed out by the gaussian distribution of ν_Q, resulting in gaussian broadening of the individual satellites, and that for orientations of the principal axis system with the magnetic field of $\theta = 0°$ and 90°, the shift in the satellite resonances is readily detectable. Both these results are inconsistent with the data.

That the AlPdMn powder and single grain spectra are nearly identical (Fig. 5.11) again suggests that the very structure of the quasilattice in the single grain, despite the well defined symmetry axes determined by the high degree of long-range positional order, creates a distribution of local electric field gradient principal axes that rivals that of a powder.

5. ^{63}Cu NMR and Local Symmetry at the Cu Site

A priori, one expects the copper central lines to be determined primarily by the second order quadrupole interaction, since the larger Z of copper compared to aluminum makes it even more sensitive to distortions of the inner electronic shells by the electric field gradients of the lattice ions [34]. However, the field dependence of the copper central lines has been difficult to verify, due to the weak ^{63,65}Cu signal at the lowest resonance condition, and to the overlapping of the copper central lines with the aluminum satellites (Fig. 5.4-5.8).

One may still proceed to analyze the copper NMR lines by studying the data at the lowest frequency at which the copper lines are still detectable, where, due to the $1/\nu$ dependence of the second order quadrupole interaction, the quadrupole effects are maximized. Thus we examine the NMR spectra at 24 MHz shown in Fig.s 5.4 - 5.8 (b).

One should note that, if both aluminum and copper lines are determined primarily by the second order quadrupole interactions, the ratio of their central line widths will be the same for all resonance conditions. From Chapter 3 the width of the central line, Δ, assuming a dominance of quadrupole effects, is given by $\Delta = (a - \frac{3}{4})\overline{\nu_Q}^2 / \nu_0$, and the ratio for aluminum and copper central linewidths is

$$\frac{^{63}\Delta}{^{27}\Delta} = \frac{3}{8}\left(\frac{\overline{^{63}\nu_Q}}{\overline{^{27}\nu_Q}}\right)^2 \tag{5.17}$$

where $a \equiv I(I+1)$ is 15/4 for copper and 35/4 for aluminum, and where $\overline{\nu_Q}$ is an average quadrupole coupling frequency. The above ratio is therefore field independent. From the NMR data of Fig.s 5.4 - 5.8, one finds $^{63}\Delta/^{27}\Delta \approx 3-4$ at 8.2 T, and $^{63}\Delta/^{27}\Delta \approx 1-2$ at 24 MHz. We considered this to be reasonably consistent with the field independence of the above equation, and attributed the variation to difficulty in separating the Al and Cu central linewidths at 24 MHz. Taking the 8.2 T value $^{63}\Delta/^{27}\Delta \approx 3$ and $\overline{^{27}\nu_Q} = 2.1$ MHz

$$\overline{^{63}\nu_Q} \approx 3\overline{^{27}\nu_Q} = 6.3 \text{ MHz} \tag{5.18}$$

If one takes the value $^{63}\Delta/^{27}\Delta \approx 1-2$, on the other hand, one finds $\overline{^{63}\nu_Q} \approx 3$ - 5 MHz, suggesting the copper $\pm 3/2 \leftrightarrow \pm 1/2$ NQR resonances should be detectable within the $\pm 5/2 \leftrightarrow \pm 3/2$ NQR spectra of Fig. 5.9. However, the lack of additional peaks in Fig. 5.9 may be taken as indication that $\overline{^{63}\nu_Q}$ is not in the range of 3 - 5 MHz.

One may then compare the average electric field gradients at the nuclear sites for Al and Cu, to determine if the chemical ordering of the quasilattice yields similar local environments for the two nuclei. Note that for ^{63}Cu,

$$\overline{^{63}\nu_Q} = \frac{e}{2h}{}^{63}Q\left|\overline{^{63}V_{zz}^{tot}}\right|,$$

and for ^{27}Al,

$$\overline{^{27}\nu_Q} = \frac{3e}{20h}{}^{27}Q\left|\overline{^{27}V_{zz}^{tot}}\right|,$$

and therefore

$$\frac{\overline{^{63}\nu_Q}}{\overline{^{27}\nu_Q}} = \frac{10}{3}\frac{^{63}Q}{^{27}Q}\frac{\left|\overline{^{63}V_{zz}^{tot}}\right|}{\left|\overline{^{27}V_{zz}^{tot}}\right|} \tag{5.19}$$

where $\left|V_{zz}^{tot}\right| = \left|V_{zz}^{el}\right| - \left|V_{zz}^{latt}\right|(1-\gamma_\infty)$. As mentioned previously, for many nuclei in a wide variety of metals and alloys, the ratio of the electronic to the lattice contributions of the total electric field gradient is 3 - 4 [60]. From the NQR data of AlCuFe and AlCuRu, one finds a ratio ≈ 5

for the aluminum nucleus. Assuming the copper nuclei exhibit nearly the same behavior, one may write eqn. (5.19) as

$$\frac{\overline{{}^{63}\nu_Q}}{\overline{{}^{27}\nu_Q}} = \frac{10}{3}\frac{{}^{63}Q}{{}^{27}Q}\frac{(1-{}^{63}\gamma_\infty)}{(1-{}^{27}\gamma_\infty)}\frac{\left|\overline{{}^{63}V_{zz}^{latt}}\right|}{\left|\overline{{}^{27}V_{zz}^{latt}}\right|} \tag{5.20}$$

Calculating the ratio of the gradients using $\overline{{}^{27}\nu_Q} = 2.1$ MHz, $\overline{{}^{63}\nu_Q} = 6.3$ MHz, ${}^{27}Q = 0.140 \times 10^{-24}\,cm^2$, ${}^{63}Q = 0.209 \times 10^{-24}\,cm^2$, $(1-{}^{27}\gamma_\infty) = 3.3$, $(1-{}^{63}\gamma_\infty) = 16$, one finds

$$\left|\overline{{}^{63}V_{zz}^{latt}}\right| = 0.1\left|\overline{{}^{27}V_{zz}^{latt}}\right| \tag{5.20b}$$

This would indicate that the average gradient at the copper sites due to lattice charges is much smaller than that of aluminum. Before comparing this unexpected result with a theoretical estimate of $\left|V_{zz}^{latt}\right|$ at the copper sites, we want to be sure that the copper NMR signal measured is representative of all copper nuclei in the sample, and not of merely a small fraction.

To do this, we studied the areas under the copper and aluminum central lines at 24 MHz. The area under the NMR line may be calculated by eqn. (3.4), which gives the area under the full resonance line, including the quadrupole satellites. Because the area under the full resonance line could be determined experimentally for copper, we proceeded to analyze the central lines by correcting eqn. (3.4) to give the area under the central line only. The magnetic dipole transition matrix element, I(I+1) - m(m-1), gives the intensities for the m $\leftrightarrow$ m-1 transitions, and results in line intensities for copper in the ratios 3 : 4 : 3, and for aluminum of 5 : 8 : 9 : 8 : 5. On the basis of these ratios, the central line contributes 40% of the total line intensity in copper, and 26% for aluminum. Using eqn. (3.3), one may then write for the ratio of the areas under the central lines, denoted by A,

$$\frac{{}^{63}A + {}^{65}A}{{}^{27}A} = \frac{\frac{2}{3}\left({}^{63}\gamma\right)^3 + \frac{1}{3}\left({}^{65}\gamma\right)^3}{\left({}^{27}\gamma\right)^3}\frac{\frac{3}{2}\left(\frac{3}{2}+1\right)}{\frac{5}{2}\left(\frac{5}{2}+1\right)}\frac{0.40}{0.26}\frac{{}^{Cu}N}{{}^{Al}N} \tag{5.21}$$

where N is the total number of copper or aluminum nuclei. For the alloys $Al_{85-x}Cu_xRu_{15}$ x = 15, 17, 20, and $Al_{65}Cu_{23}Fe_{12}$, eqn. (5.21) gives values of

$\frac{^{Cu}A}{^{Al}A_{Theory}} \equiv \frac{^{63}A+^{65}A}{^{27}A} \approx 0.15\text{-}0.21$, 0.24 respectively. To determine the integrated line intensities ^{27}A, ^{63}A, ^{65}A we measured the areas beneath the central lines and above the Al satellite background in all field scan spectra at 24 MHz. For both the AlCuRu and AlCuFe systems we obtained $\frac{^{Cu}A}{^{Al}A_{Exp}} \equiv \frac{^{63}A+^{65}A}{^{27}A} \approx 0.15 \pm 0.04$. The resulting agreement between theory and experiment indicates that a large fraction of the copper nuclei do indeed experience lower gradients on average than aluminum.

To compare the result of eqn. (5.20b) with a theoretic calculation, we performed a simulation of $\left|V_{zz}^{latt}\right|$ at the copper sites in the AlCuFe 1/1 approximant model discussed previously, to determine the distribution of gradients. The simulation was performed as described earlier for aluminum NQR, but this time was performed for the copper sites. Fig. 5.21 gives the $\left|V_{zz}^{latt}\right|$ histograms for three charge configurations of Fe(Ru), and one finds the mean values of the aluminum (from data of Fig. 5.16) and copper lattice gradients to be such that $\left|\overline{^{63}V_{zz}^{latt}}\right| \approx 0.8\left|\overline{^{27}V_{zz}^{latt}}\right|$.

The discrepancy between the result of eqn. (5.20b) and the electric field gradient model calculation is almost one order of magnitude, and appears to be outside experimental uncertainty even considering the uncertainties in studying the copper NMR line. One is therefore lead to the conclusion that the assumptions inherent in eqn. (5.20b) are not all valid. There are two primary assumptions that require re - examination. The first assumption is that the semi - empirical ratio $\left|V_{zz}^{el}\right| / (1-\gamma_\infty)\left|V_{zz}^{latt}\right| \approx 5$ determined for aluminum applies to copper as well, an assumption applied to a lack of copper NQR spectra through which one could obtain such a result. We note that if this ratio were ≈ 2 for copper, as is reasonable according to [60 Vianden], one finds

$$\left|\overline{^{63}V_{zz}^{latt}}\right| = 0.5\left|\overline{^{27}V_{zz}^{latt}}\right|$$

in reasonable agreement with the computed ratio of 0.8. The fact that $\left|V_{zz}^{el}\right|$ for ^{63}Cu is a smaller fraction of the lattice contribution than for ^{27}Al would then imply that the wave function of the valence/conduction electrons around the copper ions is much more s - like than for aluminum. The second assumption is that the Sternheimer antishielding factor $(1-\gamma_\infty)$, values of which have been found in the non - interacting electron approximation [59 Cohen], is 3.3 for Al^{3+} and 16 Cu^{+}, giving a ratio $(1-{}^{63}\gamma_\infty)/(1-{}^{27}\gamma_\infty) = 4.8$. The accuracy of these vales is difficult to determine [59]. We note that a value of the copper $(1-\gamma_\infty)$ that is 30% lower than our assumed value of 16, combined with the above ratio ≈ 2 for the electronic and lattice gradients of copper, gives

$$\left|\overline{{}^{63}V_{zz}^{latt}}\right| = 0.7\left|\overline{{}^{27}V_{zz}^{latt}}\right|$$

in reasonable agreement with the simulation results.

Further work on ^{63}Cu NMR - NQR is needed to clarify this issue. This work should focus on NMR measurements taken at 5 T, a field value intermediate to those of our study and at which the copper lines will be easily detectable, and NQR measurements above 6 MHz, to check for a copper $\pm 3/2 \leftrightarrow \pm 1/2$ NQR line.

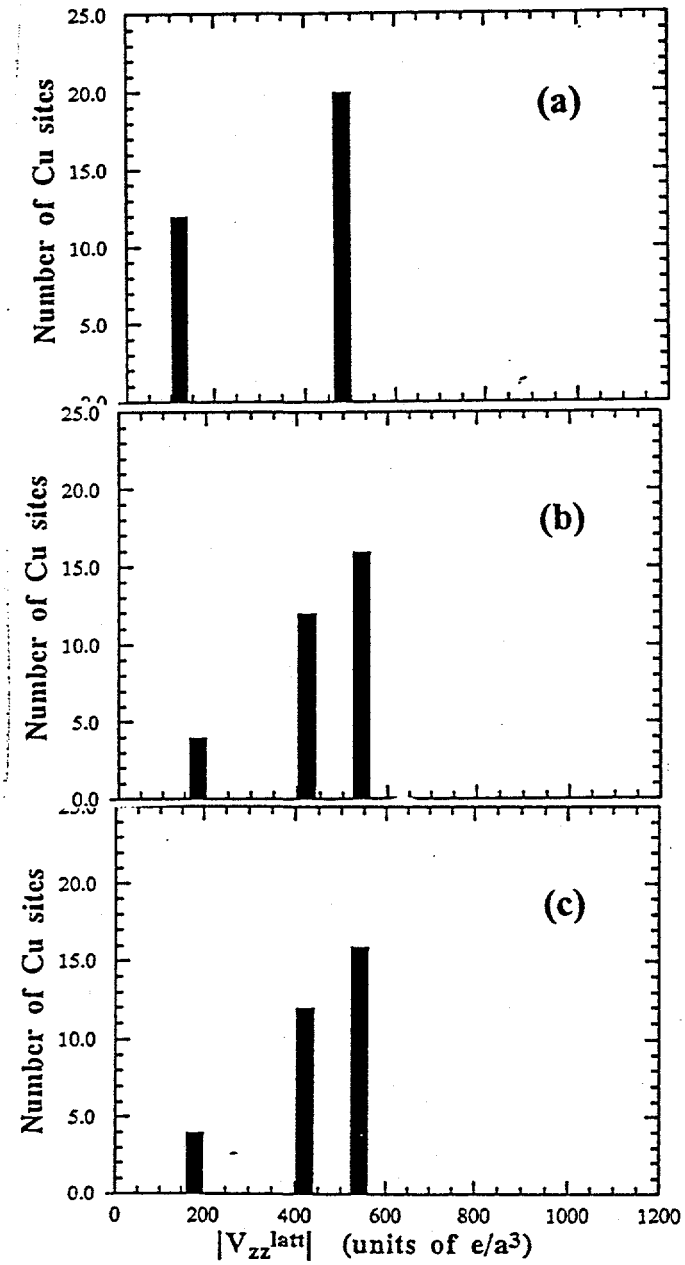

Fig. 5.21 Histogram of $\overline{V_{zz}^{latt}}$ for Cu sites, in units of e/a^3, where a = 12.3 Å. The bin sizes are $60e/a^3$. The Al, Cu, and Fe(Ru) ions were taken respectively to have the charges: (a) 3, 1, 1; (b) 3, 1, 2; (c) 3, 1, 3.

CHAPTER 6. KNIGHT SHIFT, RELAXATION TIME, MAGNETIC SUSCEPTIBILITY, AND THE ELECTRONIC STRUCTURE

In this chapter, we discuss the electronic properties of AlCuFe and AlCuRu quasicrystals through studies of magnetic susceptibility, Knight shift values, and nuclear spin-lattice relaxation times. In particular, we discuss an AlCuRu compositional, and medium pressure study of the NMR parameters, in the light of Biggs et al.'s hypothesis of pseudogap fine structure, and compare with conclusions from a high-temperature study by Hill et al.

A. Results

The magnetic susceptibilities of all three AlCuRu quasicrystals of the batch #1 quasicrystals were measured by Ostensen [62] as a function of temperature, and are presented in Fig. 6.1. One can see that the temperature independent contribution to the susceptibilities for all three samples are diamagnetic and the same to within experimental uncertainty, as given in Table 6.1.

^{27}Al Knight shifts K_{iso} were measured in the AlCuFe and AlCuRu batch #1 samples from analysis of the NMR lineshape data given in Fig. 5.4 - 5.8, and the results are given in Table 5.1. The anisotropic Knight shift, K_{an}, was also discussed in Chapter 5 and found to be zero within experimental uncertainty.

Fig. 6.2 shows the nuclear spin-lattice relaxation data for the ^{27}Al, ^{63}Cu, ^{65}Cu nuclei in a typical batch #1 sample. The solid lines represent fits to the relaxation laws, discussed in Chapter 3 for the case of magnetic dipole relaxation, and given by eqns. (3.52) and (3.53). From this procedure, we obtained the fit parameter W_M, from which the spin-lattice relaxation rate $2W_M$ may be determined. The high quality of the fit indicates that spin-lattice relaxation is dominated by magnetic, rather than quadrupolar, relaxation mechanisms. The relaxation laws for quadrupolar relaxation were also applied, but found to yield inadequate fits. The values W_M are summarized in Table 6.2 for two temperatures.

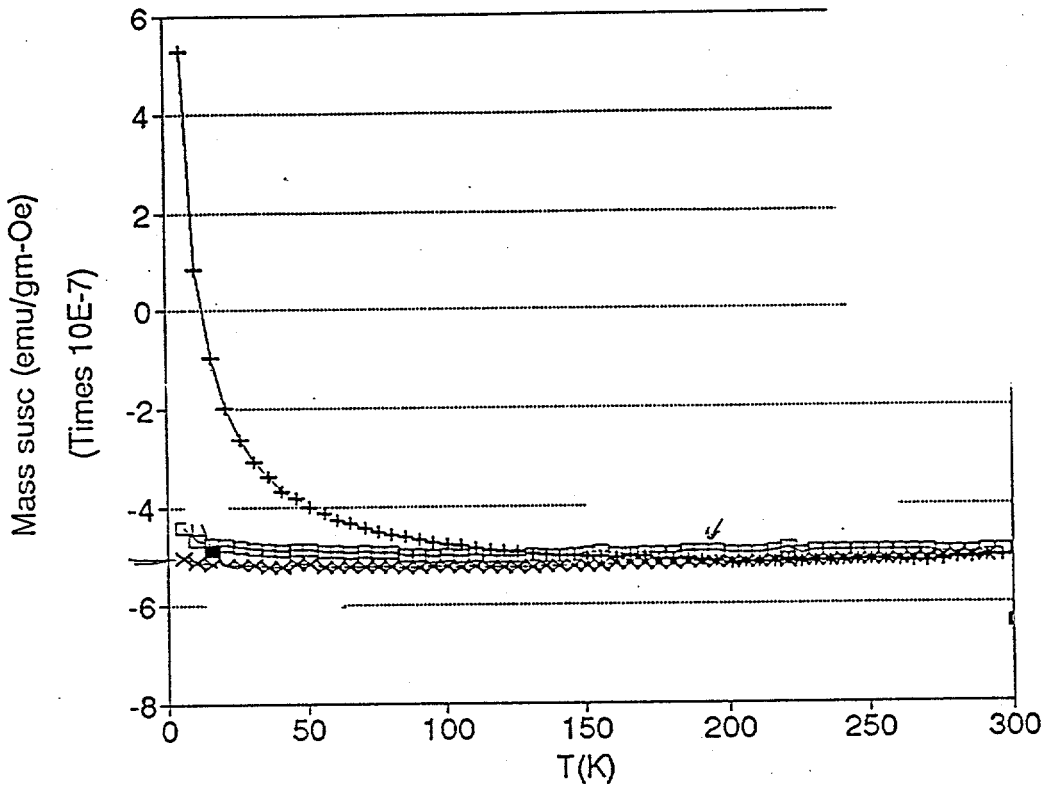

Fig. 6.1 Magnetic susceptibility measurements in $Al_{70}Cu_{15}Ru_{15}$ (×), $Al_{68}Cu_{17}Ru_{15}$ (+), $Al_{65}Cu_{20}Ru_{15}$(open square) for batch #1 samples.

Table 6.1 Total (χ_0), core (χ_{core}) and Pauli (χ_P) molar susceptibilities for $Al_{70}Cu_{15}Ru_{15}$, $Al_{68}Cu_{17}Ru_{15}$, $Al_{65}Cu_{20}Ru_{15}$ batch #1 samples.

x	χ_0 (emu/mol) x10^6	χ_{dia} (emu/mol) x10^6	χ_P (emu/mol) x10^6
15	-24	-28	5
17	-24	-28	5
20	-24	-28	5

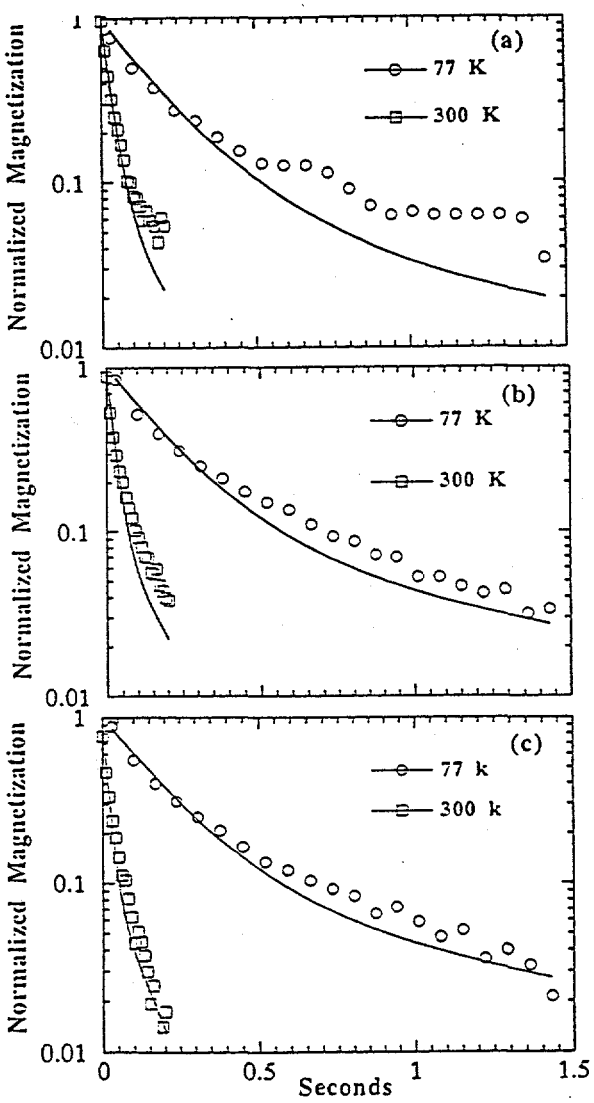

Fig. 6.2 Semi-log plot of the recovery of the normalized nuclear magnetization, $\frac{M(\infty)-M(t)}{M(\infty)}$ following a "short" saturating RF pulse sequence in $Al_{65}Cu_{20}Ru_{15}$ at 8.2 T and at two different temperatures: (a) ^{27}Al central line relaxation; (b) ^{63}Cu central line relaxation; (c) ^{65}Cu central line relaxation. The full solid curves are theoretical fits by using eqns. (3.53.1) and (3.52.1) for ^{27}Al and $^{63,65}Cu$ respectively. The values of W_M obtained from least squares fits are given in Table 6.2.

Table 6.2 Fit parameters W_M for the batch #1 samples obtained by fitting ^{27}Al, ^{63}Cu, and ^{65}Cu relaxation data to recovery laws of eqns. (3.52.1) and (3.53.1). Spin-lattice relaxation rate is given by $2W_M$.

	Sample	^{27}Wm (Hz)	^{63}Wm (Hz)	^{65}Wm (Hz)	^{63}Wm/^{65}Wm
77 K	15	0.25 ± 0.02	0.51 ± 0.02	0.52 ± 0.02	0.97 ± 0.08
	17	0.20 ± 0.01	0.45 ± 0.02	0.42 ± 0.01	1.08 ± 0.07
	20	0.21 ± 0.01	0.46 ± 0.02	0.46 ± 0.01	1.00 ± 0.07
	C	0.20 ± 0.01	0.34 ± 0.02	0.40 ± 0.02	0.86 ± 0.09
	QC	0.19 ± 0.01	0.46 ± 0.02	0.43 ± 0.01	1.07 ± 0.07
300 K	15	1.57 ± 0.05	4.0 ± 0.2	4.8 ± 0.3	0.84 ± 0.09
	17	1.59 ± 0.04	3.7 ± 0.2	4.4 ± 0.3	0.84 ± 0.09
	20	1.38 ± 0.04	3.8 ± 0.2	5.0 ± 0.4	0.8 ± 0.1
	C	0.94 ± 0.04	3.0 ± 0.2	3.9 ± 0.2	0.8 ± 0.1
	QC	0.70 ± 0.04	2.3 ± 0.1	2.4 ± 0.1	0.95 ± 0.06

Fig. 6.3 shows the dependence of $2W_M$ for ^{27}Al as a function of temperature for the $Al_{68}Cu_{17}Ru_{15}$ and $Al_{65}Cu_{20}Ru_{15}$ samples, the two compositions reported by Biggs et al. to have γ values that differed by a factor of two (Chapter 2), and for the crystalline and quasicrystalline phases of AlCuFe. The data show no measurable dependence of $2W_M$ on the composition of the alloy (Fig. 6.3(a)), or on the long-range order (Fig. 6.3(b)). In the case of AlCuFe, the temperature dependence of $2W_M$ is linear up to room temperature, as expected for a relaxation mechanism due to conduction electrons, whereas both AlCuRu samples show deviation from the linear extrapolation of the low temperature data.

In order to further study the nature of the relaxation rate at high temperature, we performed $2W_M$ measurements above 300 K in a high purity (see Fig. 6.4) $Al_{68}Cu_{17}Ru_{15}$ sample (batch #2) reported by Swenson [46] to have specific heat properties in very good agreement with those of Biggs et al. Fig. 6.5 shows our data on a semi-log scale, compared with data taken by Hill et al. for Biggs' $Al_{65}Cu_{20}Ru_{15}$ sample. There is no difference within experimental uncertainty between the temperature data of the two samples, and above 300 K the data shows marked deviation from linear behavior.

As an alternative to a compositional study (see Chapter 2), where one has the additional complication of attempting to maintain consistent levels of sample quality, we performed a study pressure study of the NMR properties on a $Al_{65}Cu_{20}Ru_{15}$ sample (batch #3) of high phase purity (see Fig. 6.6). ^{27}Al and ^{65}Cu Knight shifts and relaxation times were studied as a function of pressure up to 2,000 atm., the maximum value attainable with the helium gas compression system used. Fig. 6.7 shows the ^{27}Al central lines at several helium gas pressures. As described later, based on Biggs et al.'s interpretation of the γ variation in AlCuRu and the dominance of s-band terms in the Knight shift, we looked for a shift of the ^{27}Al line on the order of the half width of the line. Fig. 6.7 shows no measurable shift of the line over the pressure range we achieved. In addition, the relaxation rates $2W_M$ shown in

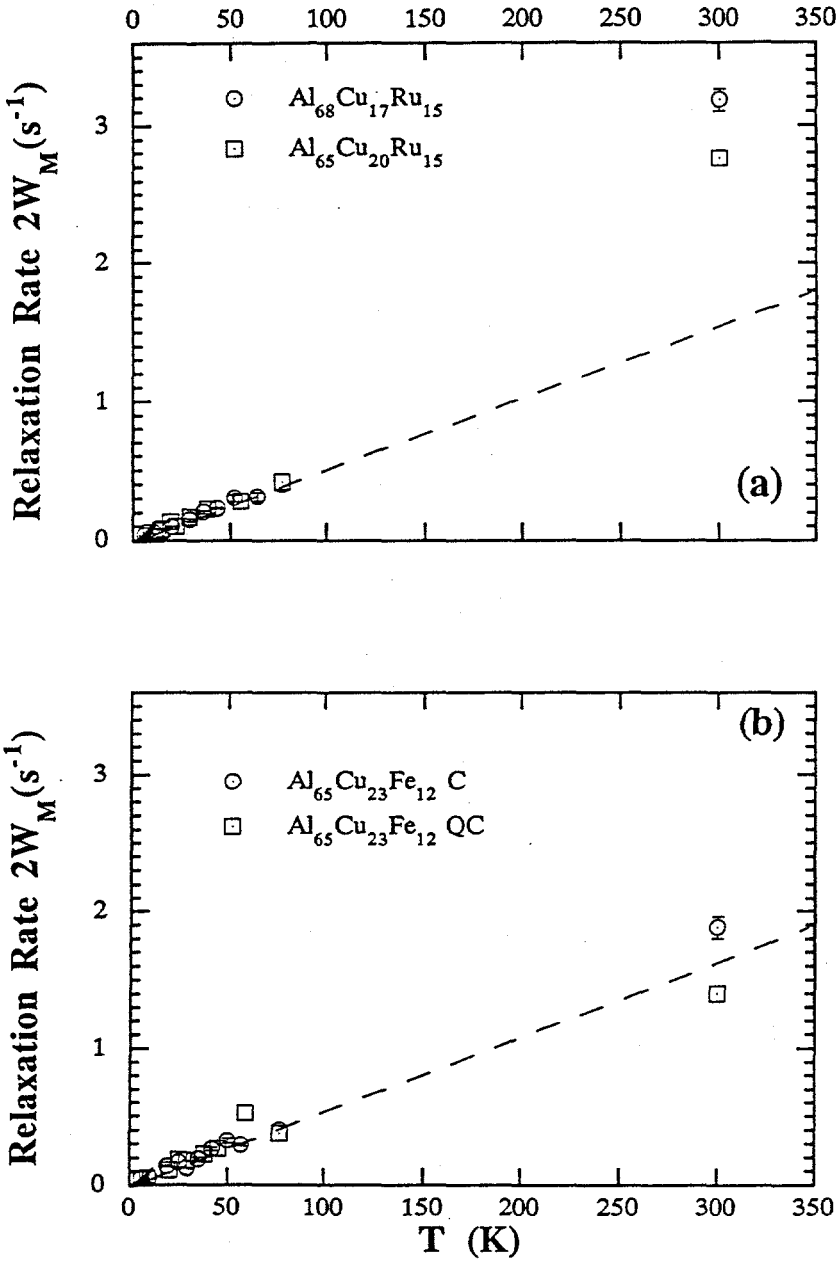

Fig. 6.3 ^{27}Al spin-lattice relaxation rates versus temperature for batch #1 samples (a) AlCuRu samples quasicrystals; (b) AlCuFe crystalline approximant and quasicrystalline samples.

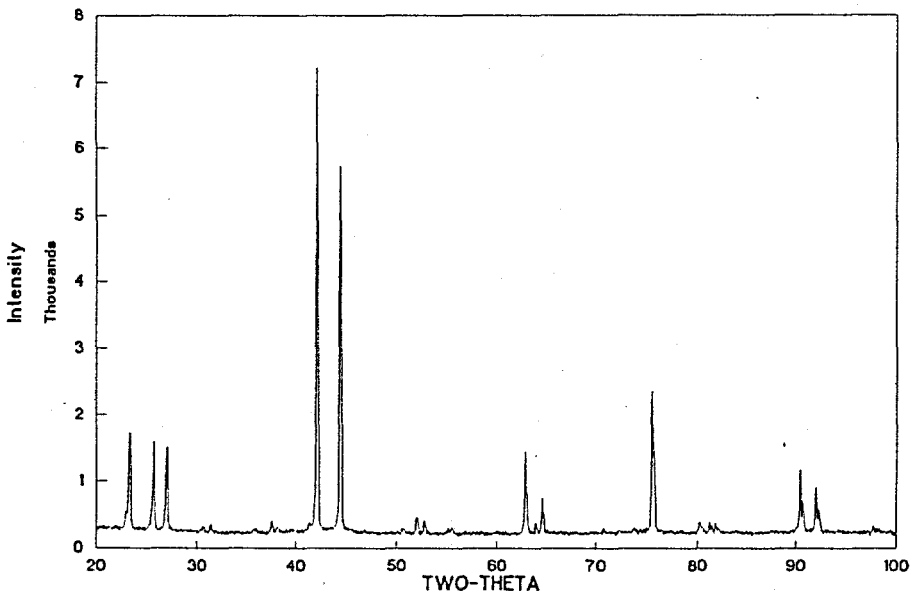

Fig. 6.4 X-ray scan of $Al_{68}Cu_{17}Ru_{15}$ batch #2 sample used for high temperature NMR measurements.

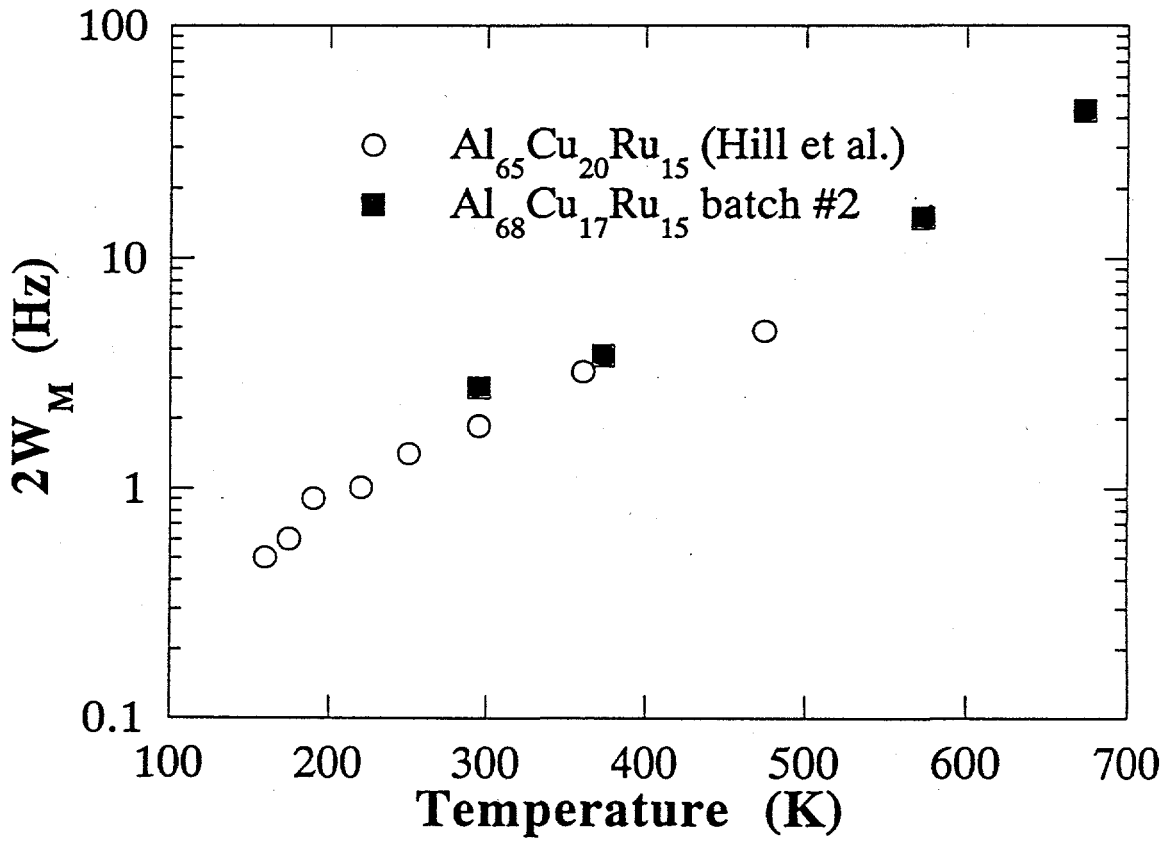

Fig. 6.5 ^{27}Al spin-lattice relaxation rates for $Al_{68}Cu_{17}Ru_{15}$ (batch #2) and $Al_{65}Cu_{20}Ru_{15}$ (taken from Hill et al. ref. [15]) samples at high temperature.

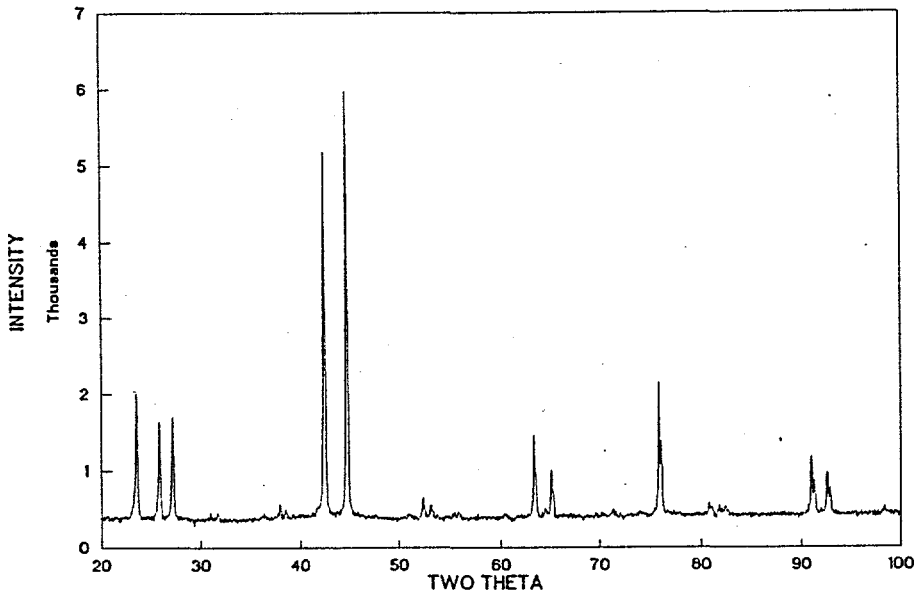

Fig. 6.6 X-ray scan of $Al_{65}Cu_{20}Ru_{15}$ batch #3 sample used for medium pressure NMR measurements.

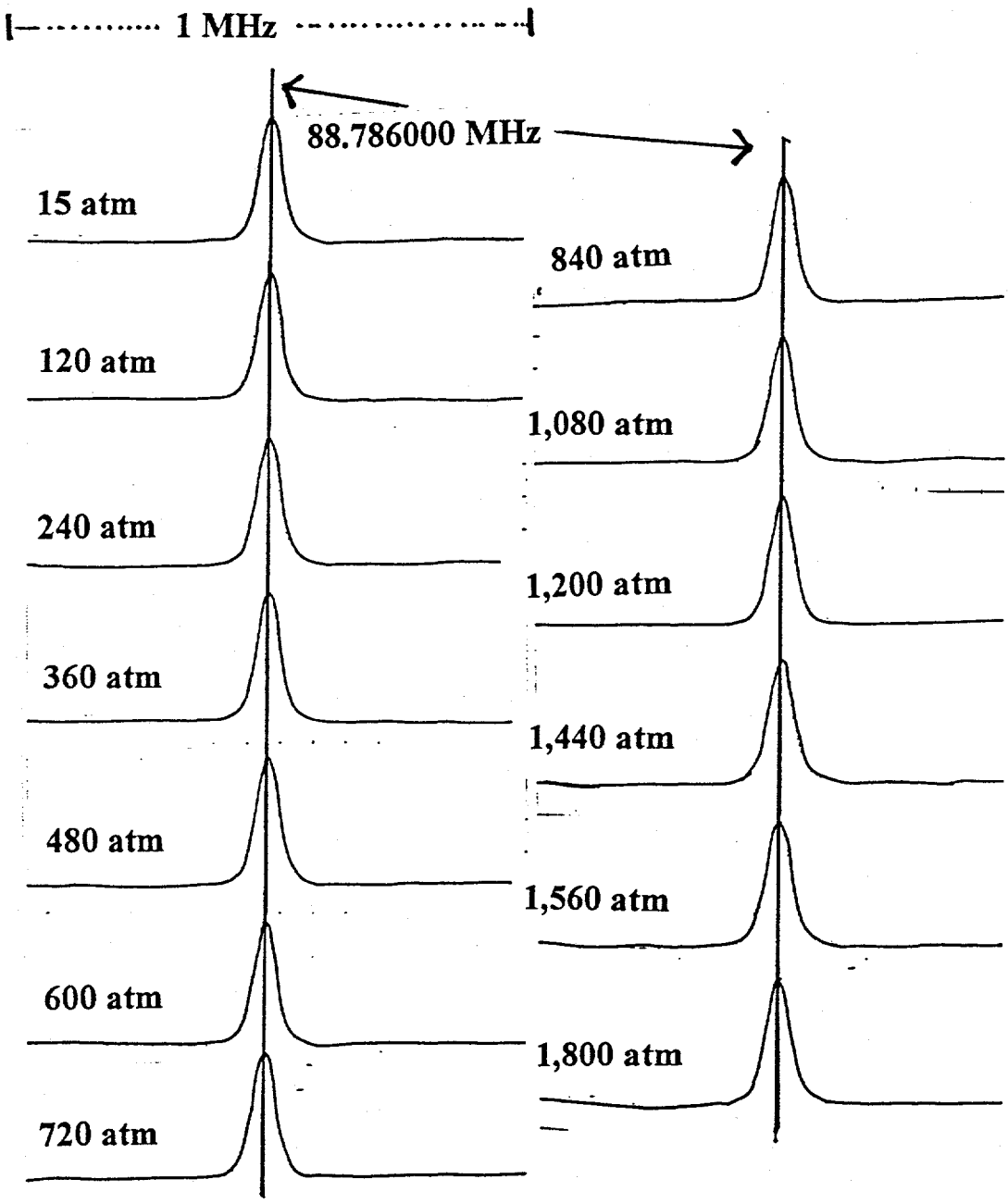

Fig. 6.7 ^{27}Al central line Fourier transform spectra taken in the $Al_{65}Cu_{20}Ru_{15}$ batch #3 sample at 77 K and H_0 = 8.0 T as a function of helium gas pressure using Hahn echo detection.

Fig. 6.8, which should be even more sensitive to changes of the DOS than the position of the ^{27}Al central line, show no change with pressure within the uncertainty of the data. We emphasize that before the data can be interpreted, one must discuss how the Fermi energy changes with pressure in AlCuRu quasicrystals.

B. Analysis and Interpretation of Experimental Results

1. Magnetic susceptibility

The magnetic susceptibilities for the AlCuRu samples were analyzed to obtain the Pauli susceptibility, χ_P, which in a nearly free electron model is proportional to the DOS at the Fermi level.

The total experimental susceptibility χ_{exp} may be separated into temperature dependent and independent parts

$$\chi_{exp} = \chi_0 + \chi(T) \tag{6.1}$$

where the temperature independent part χ_0 may be written

$$\chi_0 = \chi_P + \chi_{core} + \chi_{cond} \tag{6.2}$$

and the temperature dependent Curie-Weiss term is given by

$$\chi(T) = \frac{C}{T-\theta} \tag{6.3}$$

The values χ_0 are shown in Table 6.1 and are the same to within experimental uncertainty. The C values for each AlCuRu sample were on the order of 10^{-5} - 10^{-6} emu K/g, implying a concentration of local moments of $\approx 10^{-3}$ at% [16 Kittel]. As this is consistent with the 99.99% purity level of the elemental constituents used in making the alloys, we attribute these moments to small concentrations of magnetic impurities in the sample.

In the nearly free electron model, one may write the Pauli susceptibility as

$$\chi_P = \tfrac{3}{2}(\chi_0 - \chi_{core}) \tag{6.4}$$

The values of χ_{core} have been estimated in the elements for several ionization states of the atom, through relativistic Hartee-Fock calculations [39]. For an alloy system

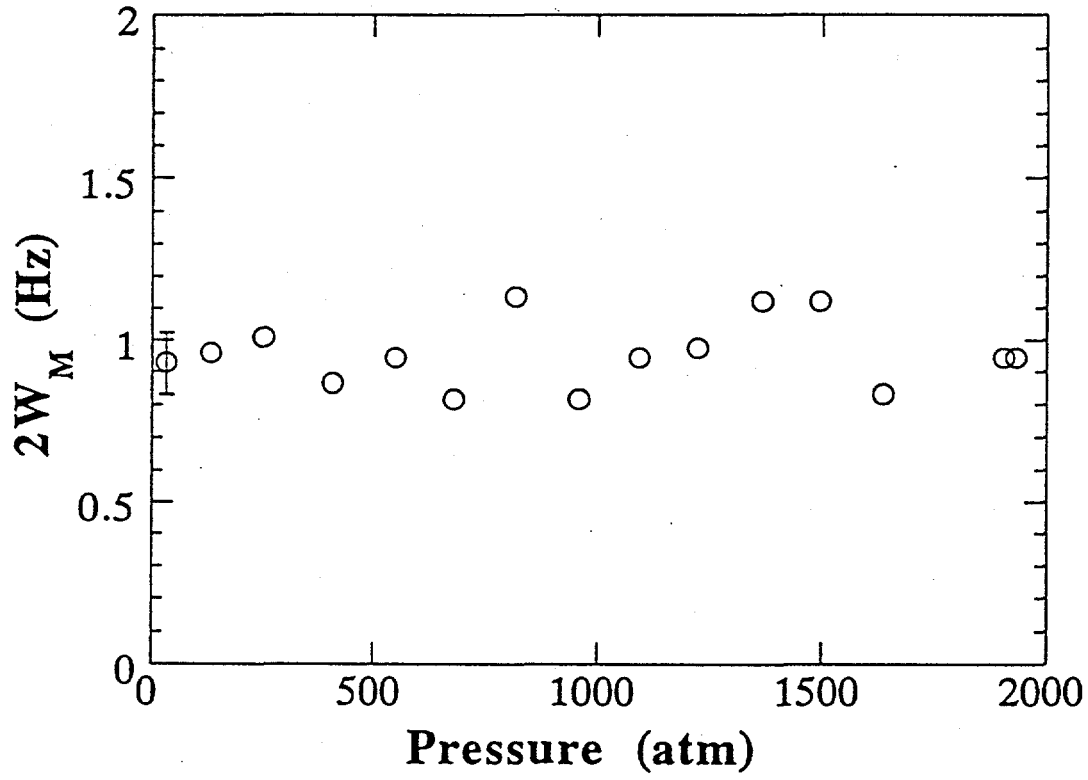

Fig. 6.8 ^{65}Cu spin-lattice relaxation rate $2W_M$ taken in $Al_{65}Cu_{20}Ru_{15}$ batch #3 sample at 77 K and $H_0 = 8.0$ T, as a function of helium gas pressure. Saturation was achieved by 40 $\pi/2$ pulses, consistent with the long saturation condition of recovery law eqn. (3.52.2).

$A_xB_yC_z$, the total diamagnetic contribution from all ions may be estimated by the weighted sum

$$\chi_{core} = \frac{\left(x\chi_{core}(A) + y\chi_{core}(B) + z\chi_{core}(C)\right)}{x+y+z} \qquad (6.5)$$

where $\chi_{core}(A)$ is the diamagnetic contribution from ion A. We assumed non-ionized atomic configurations, consistent with the very low density of conduction electron states in these materials, and give the values of χ_{core} based on eqn. (6.5), and χ_P based on eqn. (6.4), in Table 6.1.

We caution, however, that the χ_P magnitudes obtained in this way are highly approximate, due to uncertainties in the calculations of the $\chi_{core}(A)$, the approximate nature of eqn. (6.5), and the uncertain ionization states within the quasicrystal. If one takes the ionization states Al^{3+}, Cu^{1+}, Ru^{1+} used previously in the model for the electric field gradient, one obtains values for χ_P which are negative, and therefore unacceptable. We interpreted this as an indication that the χ_P values of Table 6.1 should be taken only as approximate upper limits to the Pauli susceptibility.

2. NMR Results

The deviation of the ^{27}Al spin-lattice relaxation rates at room temperature from a linear extrapolation of the data at low temperature in the AlCuRu alloys (Fig. 6.3) indicates the presence of an additional relaxation mechanism at high temperatures. The low temperature behavior exhibits the linear behavior consistent with behavior seen in other quasicrystalline systems [12], [9], where the dominant relaxation mechanism was due to conduction electron relaxation. We focus first on the low temperature behavior, and discuss the high temperature behavior later.

When the dependence of $2W_M$ on temperature is linear, the slope of the line is denoted $(T_1T)^{-1}$ where $T_1 = 1/2W_M$. By fitting to the low temperature ^{27}Al data up to 77 K, one finds the $(T_1T)^{-1}$ to be 5.2 ± 0.3 and $5.5 \pm 0.3 \times 10^{-3}$ $s^{-1}K^{-1}$ for $Al_{68}Cu_{17}Ru_{15}$ and

$Al_{65}Cu_{20}Ru_{15}$ respectively, and 5.2 ± 0.3 and $4.9 \pm 0.3 \times 10^{-3}$ $s^{-1}K^{-1}$ for the crystalline and quasicrystalline phases of $Al_{65}Cu_{23}Fe_{12}$, respectively. Thus we find no change in $(T_1T)^{-1}$ with sample composition or long range order.

Before moving to a discussion of the NMR parameter, magnetic susceptibility, and electronic structure, we note that analysis methods of the Knight shift and spin-lattice relaxation data reported in the literature vary. It is important to discuss these alternate approaches and compare them with our own methods, discussed in Chapter 5 for the Knight shift, and in the previous section for the spin-lattice relaxation time.

Hippert [12] and Drews [9] both studied AlCuFe and obtained ^{27}Al $(T_1T)^{-1}$ values considerably different from our own, the variations stemming from the different recovery laws used to obtain $2W_M$. Hippert et al. obtained $(T_1T)^{-1} = 17 \times 10^{-3}$ $s^{-1}K^{-1}$ for both crystalline and quasicrystalline phases of $Al_{62}Cu_{25.5}Fe_{12.5}$, and reported that the standard recovery law for short irradiation of the central line, given by eqn. (3.53.1) did not yield acceptable fits. They fit their data to

$$f(t) = \alpha e^{-2W_M t} + \beta e^{-12W_M t} + \gamma e^{-30W_M t} \qquad (6.6)$$

i.e. replacing the fixed coefficients of eqn. (3.53.1) by parameters that were allowed to vary in the fit, and obtained coefficients $\alpha = 0.25$, $\beta = 0.47$, $\gamma = 0.28$, as compared with $\alpha = 0.029$, $\beta = 0.178$, $\gamma = 0.794$ of Chapter 3. This point is important, because Hippert suggests that the inadequacy of the standard recovery law might be explained by a distribution of spin-lattice relaxation times that arises from a distribution of electronic environments. Our results, on the other hand, as well as the results of Hill [15], indicate good agreement between the standard recovery laws, from which we concluded that no effect arising from a distribution of relaxation times is present. In addition, Drews et al. reported that their relaxation data, obtained by saturating the central Al line with multiple pulses, could be adequately fit with a

simple exponential recover with and additional constant to correct for incomplete saturation of the line, given by

$$f(t) = A + Be^{-2W_M t} \tag{6.7}$$

and on the basis of this they obtained the value $(T_1T)^{-1} = 73 \times 10^{-3}$ $s^{-1}K^{-1}$, which is an order of magnitude larger than our own. Our magnetization recovery data of Fig. 6.2 clearly indicate non-exponential recover, and Hill [63] has shown that the data of Drews et al. may be adequately fit by the standard recovery laws of Chapter 3, resulting in $(T_1T)^{-1} = 4.9 \times 10^{-3}$ $s^{-1}K^{-1}$. This is in very good agreement with our own value of $(4.9 \pm 0.3) \times 10^{-3}$ $s^{-1}K^{-1}$. We conclude that the most satisfying interpretation of the relaxation data therefore arises through analysis based on the standard recovery laws we have presented in Chapter 3.

Other measurements of ^{27}Al K_{iso} have been reported in both AlCuFe and AlCuRu, though no previous measurements have included the effects of the quadrupole interaction on the central line position. Hippert et al. reported $K_{iso} \leq 0.01\%$ in AlCuFe from a plot of the spin echo intensity at 7 T, and Drews et al. reported a value $K_{iso} = 0.02 \pm 0.03$ % from the same method. Hill et al. achieve greater precision by obtaining the Fourier transform spectrum of the ^{27}Al central line and 9 T, and found $K_{iso} = 0.015$ %. The above values were all found by the expression

$$K_{iso} = \frac{\nu - \nu_{ref}}{\nu} \tag{6.8}$$

where ν is the frequency at the center of the ^{27}Al resonance in the quasicrystal, and ν_{ref} is the resonance frequency of a diamagnetic reference. However, when the nucleus is has strong quadrupolar coupling, the above expression must be corrected for second order quadrupole effect, which contributes a term that varies as $1/\nu^2$ [39]. For small Knight shifts, these corrections can be significant even at high frequency. Such corrections are included in the K_{iso} values given in Table 5.1, which were obtained from the NMR lineshape simulations, by virtue of the second order quadrupole effects being included in the calculation of the

resonance frequencies. We therefore conclude by noting that the systematic error introduced by not including quadrupole effects may be seen, by comparing K_{iso} from Table 5.1 with the shifts given above, to be 60 - 70%.

3. Magnetic Susceptibility, NMR, and the Pseudogap

Analysis of the χ_P, K_{iso}, and $(T_1T)^{-1}$ values in the AlCuFe and AlCuRu alloys may be performed by a direct comparison with aluminum metal. We note the following values for aluminum metal: $\chi_P = 30 \times 10^{-6}$ emu/mole, $K_{iso} = 0.164$ %, and $(T_1T)^{-1} = 540 \times 10^{-3}$ $s^{-1}K^{-1}$ [39]. Table 6.3 lists ratios of the aluminum values to the values found in the AlCuFe and AlCuRu alloys.each parameter depends upon either the total electronic density of states at the Fermi energy $D(E_F)$--as in the case of χ_p--or the s- and d-band DOS $D_s(E_F)$, $D_d(E_F)$--as in the case of K_{iso} and $(T_1T)^{-1}$[64]:

One may interpret the results of Table 6.3 based on the following equations, which show how

$$\chi_p \propto D(E_F) \tag{6.9}$$

$$K_{iso} = \mu_B D_s(E_F) H_s^{hf} + \mu_B D_d(E_F) H_d^{hf} + \chi_{vv} H_{orb}^{hf} / \mu_B \tag{6.10}$$

$$(T_1T)^{-1} = \alpha_s K_s^2 + \alpha_d K_d^2 + \alpha_{orb} (\mu_B D_d(E_F) H_{orb}^{hf})^2 \tag{6.11}$$

Table 6.3 Ratios of Pauli susceptibility χ_p, isotropic Knight shift K_{iso}, and $(T_1T)^{-1}$ for aluminum metal and the AlCuFe and AlCuRu alloys (batch #1 samples)

Sample	${}^{metal}\chi_P / \chi_P$	${}^{metal}K_{iso} / K_{iso}$	${}^{metal}(T_1T)^{-1} / (T_1T)^{-1}$	${}^{metal}\gamma / \gamma$	Korringa Ratio
$Al_{70}Cu_{15}Ru_{15}$	6	6.3	83[a]	6.8[b]	2.7
$Al_{68}Cu_{17}Ru_{15}$	6	6.7	100	5.9[b]	2.9
$Al_{65}Cu_{20}Ru_{15}$	6	6.7	91	12 [b]	2.7
$Al_{65}Cu_{23}Fe_{12}$(C)	-	10	91	4.7[c]	1.3
$Al_{65}Cu_{23}Fe$(QC)	-	10	100	4.4[c]	1.3

a Determined from table 6.1 for 77K valve
b Taken from Biggs [31]
c Taken from Biggs [65]

The quantities $H^{hf}_{s,d,orb}$ are the magnetic hyperfine fields at the nucleus due respectively to the s- and d-band electrons, and to the electronic orbit; χ_{vv} is the Van Vleck susceptibility; and $\alpha_{s,d,orb}$ are prefactors of the s-, d-, and orbital terms. The s-band terms arise from the so-called contact hyperfine interaction, which is due to unpaired s-band conduction electrons interacting with the nucleus through the coupling of the electronic and nuclear moments. Since only s-band electrons have non-zero probability of being at the nuclear site, this contribution is typically the dominant one. However, it is possible for non-s electrons to contribute to the Knight shift and relaxation rate by polarizing paired electrons within the closed atomic s-shells, creating perturbations in the s-band wave function that depend largely on the d-band [39]. These "core polarization" effects are temperature dependent. Finally, the orbital contribution arises from the orbital magnetic moment of the conduction electrons induced by the applied magnetic field. This effect is essentially temperature independent, and results in a second order term that becomes appreciable in the d-band transition metals with half filled bands [39].

We analyzed the values of Table 6.3 as follows. For aluminum metal, the s-band contributions dominate the NMR parameters, allowing one to write

$$K_{iso} = \mu_B D_s(E_F) H^{hf}_s \tag{6.12}$$

$$(T_1T)^{-1} = \alpha_s K^2_{iso} \tag{6.13}$$

where in a non-interacting electron model $\alpha_s = \frac{4\pi k_B}{\hbar}\left(\frac{\gamma_n}{\gamma_e}\right)^2$ [34], where the gammas represent the gyromagnetic ratios of the nucleus and electron. For the ^{27}Al nucleus in AlCuRu and AlCuFe quasicrystals, the temperature independence of the ^{27}Al NMR line below room temperature (Fig. 5.3(b)), as well as the fact that the $(T_1T)^{-1}$ ratios of Table 6.3 are on the same order of magnitude as the square of the K_{iso} ratios, suggest a simple s-band description. The ratios in Table 6.3 then become ratios of the s-band densities of states at the

Fermi level. Since aluminum metal may be considered to be a free electron metal, the ratios therefore reflect a reduction in the available number of electronic orbitals at the Fermi surface in the quasicrystal. Values larger than one, as found in Table 6.3, are therefore indicative of a pseudogap. In addition, one should notice that the ratios of χ_p and the linear coefficients of the specific heat γ are nearly equal, consistent with a nearly free electron picture where both quantities are proportional to $D(E_F)$, the total density of states. We note, however, that none of the measurements that we performed on the $Al_{65}Cu_{20}Ru_{15}$ batch #1 sample reflected the factor of 2 change reported by Biggs et al in the measurement of γ. Our data therefore are consistent with the presence of a pseudogap, but not with pseudogap fine structure.

The s-band model is in reasonable agreement not only with the relative values of K_{iso} and $(T_1T)^{-1}$, but with their absolute values as well. One measure of this is the Korringa ratio, which is defined as the ratio $A = T_1TK_{iso}^2 / \alpha_s$, where the numerator is determined by experimental values. In the ideal case of a non-interacting electron gas, A = 1. In reality, deviations from 1 are common in even the simplest metals, and may often be attributed to electron - electron interactions. For example, in the alkali metals, A ranges from 0.66 to 1.7 [39]. For the ^{27}Al nucleus, $\alpha_S = 3.88 \times 10^{-6}$ sK, resulting in A values that range from 1.3 to 2.9 for the AlCuRu and AlCuFe alloys. We therefore take this as further evidence that the s-band model is appropriate.

Though no predictions exist for the depth of the pseudogap in realistic transition metal quasicrystals [29], Carlsson reports preliminary results performed using one-electron potentials and an idealized reciprocal space model for the 1/1, 2/1, 3/2, ... , 8/5 approximants [33]. The calculations indicate that the pseudogaps range from approximately 1/3 of the free electron value for the 1/1 approximant, to less than 1/10 for the 3/2 approximant. We may determine the depth experimentally based on the values of Table 6.3. One finds that the K_{iso} ratios indicate that the density of states for AlCuRu quasicrystals is 1/6 - 1/7 of the free

electron value, and that for AlCuFe crystalline approximant and quasicryalline states it is 1/10 the free electron value. In addition, the lack of any difference between our experimental values of the pseudogap depth for the AlCuFe 3/2 approximant and quasicrystalline phases indicates that the electronic properties of the quasicrystal may in fact be determined by it intermediate range order, since the local atomic order of a quasicrystal and its approximants are nearly the same. This is in agreement with the NMR results of Hippert et al. who found almost identical Knight shifts and relaxation times for the AlCuFe and AlCuLi quasicrystals and their 3/2 approximants [12], as well as with theoretical investigations of Fujiwara et al. [29], who show that both pseudogaps and fine structure exist in the density of states for both the AlCuLi quasicrystal and its 3/2 approximant.

4. NMR Pressure Study of $Al_{65}Cu_{20}Ru_{15}$ and Pseudogap Fine Structure

Having given evidence that the NMR parameters may be described by a simple s-band model, in which the Knight shift K_{iso} and the spin-lattice relaxation rate $2W_M$ are respectively proportional to $D_s(E_F)$ and $D_s^2(E_F)$, one may proceed to analyze the NMR data of Fig. 6.7 and 6.8, taken as a function of pressure.

We first estimate the change in the Fermi energy expected for the quasicrystal as the pressure is increased to 2,000 atm. For aluminum metal, which is dominated by the s-band term in both the Knight shift and the relaxation rate, Kushida [66] has shown that the pressure dependence of the Fermi energy to be

$$\frac{dE_F}{E_F} = -\frac{2}{3}(1+0.3)\beta dP \qquad (6.14)$$

where β is the isothermal compressibility, defined as $\beta \equiv -\frac{1}{V}\left(\frac{\partial V}{\partial P}\right)_T$. Since the NMR parameters of the AlCuRu quasicrystal may also be described by an s-band model, we will assume that the above equation applies to the quasicrystal as well. To estimate the compressibility β for AlCuRu, we use measurements of the elastic modulus reported by

Koester et al. The compressibility β is related to the elastic modulus E, and Poisson's ratio μ, by the expression [67]

$$\beta = \frac{3(1-2\mu)}{E} \tag{6.15}$$

Taking $\mu \approx 1/3$ as found in many metals and alloys below their elastic limit, one finds $\beta \approx 1/E$. Koester [68] reports that $E \approx 1.10 \times 10^6$ atm for $Al_{64}Cu_{22}Fe_{14}$, and we therefore find $\beta \approx 0.9 \times 10^{-6}$ atm^{-1}. We note that this value is reasonable as it is intermediate to that of aluminum ($\beta \approx 1.38 \times 10^{-6}$ atm^{-1}) and ruthenium ($\beta \approx 0.31 \times 10^{-6}$ atm^{-1}). We estimate the Fermi energy by noting that the Fermi wave vector k_F in AlMn, AlLiCu, and AlFe crystalline approximants are 1.75 Å^{-1}, 1.64 Å^{-1}, and 1.73 Å^{-1} respectively [29], and we take these values as indicative of k_F in AlCuRu quasicrystals. Taking $k_F \approx 1.7$ Å^{-1}, the nearly free electron model [69] gives the Fermi energy as $E_F = (13.6 \text{ eV})(k_F a_0)^2 \approx 10$ eV, where $a_0 = 0.529$Å. Given the above values, one therefore expects a shift in the Fermi energy over a pressure range of 2,000 atm to be

$$dE_F = (0.92 \times \times 10^{-6} \text{ atm}^{-1})(2/3)(1.3)(2{,}000)(10\text{eV}) \approx 0.02 \text{ eV} \tag{6.16}$$

We note that the shift in the Fermi energy as estimated above should allow one to probe pseudogap fine structure on the order of 0.02 eV, since in an s-band model $K_{iso} \propto D_s(E_F)$ and $2W_M \propto D_s^2(E_F)$.

One may estimate the effects of pressure on K_{iso} assuming pseudogap fine structure on the order of 0.02 eV, by noting that the pressure dependence of D_s should dominate the pressure dependence of H_s^{hf}. This may be seen by taking

$$\left(\frac{\partial K_{iso}}{\partial P}\right)_T = -V\beta\left(\frac{\partial K_{iso}}{\partial V}\right)_T \tag{6.17}$$

Therefore, one has, by inserting eqn. (6.12) into eqn. (6.17)

$$\left(\frac{\partial K_{iso}}{\partial P}\right)_T = -V\beta\mu_B\left(\frac{\partial D_s(E_F)}{\partial V}H_s^{hf} + D_s(E_F)\frac{\partial H_s^{hf}}{\partial V}\right)_T \tag{6.18}$$

which may also be written in terms of the fractional changes

$$\frac{dK_{iso}}{K_{iso}} = \frac{dD_s}{D_s} + \frac{dH_s^{hf}}{H_s^{hf}} \tag{6.19}$$

For aluminum metal, Kushida [66] reported that applying a pressure of 8,000 atm resulted in an ^{27}Al fractional Knight shift of

$$\frac{dK_{iso}}{K_{iso}} = 0.01 \tag{6.20}$$

and that the fractional changes of D_s and H_s^{hf} differ only by a factor of 1/2, i.e.

$$\frac{dD_s}{D_s} \approx -\frac{1}{2}\frac{dH_s^{hf}}{H_s^{hf}} \tag{6.21}$$

For ^{27}Al in the AlCuRu quasicrystals over a pressure range of 2,000 atm, a factor of 2 change in the density of states would give

$$\frac{dD_s}{D_s} \approx 1 \tag{6.22}$$

Since H_s^{hf} is an average of s-band electron states over the Fermi surface, it may be written

$$H_s^{hf} = \frac{8\pi}{3}\mu_B \left\langle |\psi(0)|^2 \right\rangle_{FS} \tag{6.23}$$

and we assume that dH_s^{hf}/H_s^{hf} will be similar for the quasicrystal and for aluminum metal. Under this model, the change of D_s should dominate the Knight shift, and one should therefore expect

$$\frac{dK_{iso}}{K_{iso}} \approx 1 \tag{6.24}$$

The effect of a factor of 2 change in D_s should therefore result in a shift in the central line of

$$d\nu \approx dK_{iso} \cdot \nu_0 \tag{6.25}$$

which for $K_{iso} = 0.024\%$ (Table 5.1) and $\nu_0 = 88.8$ MHz one finds $d\nu \approx 20$ kHz. This is roughly the half width of the 50 kHz ^{27}Al central line in Fig. 6.7. We conclude that the pseudogap fine structure should result in a measurable shift of the ^{27}Al resonance within the pressure range we achieved.

The effects of pseudogap fine structure of the spin lattice relaxation rate follow directly from the behavior of the Knight shift in an s-band model, where $2W_M \propto K_{iso}^2$. Therefore a factor of 2 change in D_s should result in a factor of 4 change in $2W_M$.

Having established that changes in pressure over the range we used shift the Fermi energy ≈ 0.02 eV, and that the consequences of a factor of 2 change in D_s are readily detectable, the lack of any pressure dependence in Fig.s 6.7 and 6.8 appear inconsistent with pseudogap fine structure in $Al_{65}Cu_{20}Ru_{15}$ quasicrystals. Recall that the change of sign in the thermopower of $Al_{65}Cu_{20}Ru_{15}$ was explained qualitatively [31], [18] by the existence of pseudogap fine structure on a scale less than $k_B(300\ K) \approx 0.02$ eV. If one interprets the NMR results as indicating no pseudogap fine structure exists, then one needs to return to the thermopower data and explain the change in sign with a more sophisticated theory than that given in Chapter 2. On the other hand, since NMR parameters are primarily dependent on D_s rather than the total density of states $D = D_s + D_d$, one might argue that if fine structure occurred in the d- but not in the s-band, the NMR result could be reconciled with both specific heat data and thermopower data. However, it seems implausible that the symmetry of the wavefunction should determine the presence or absence of pseudogap fine structure. We therefore conclude that fine structure in D_s, should it exist, occurs on an energy scale larger than that which would explain the anomalous thermopower results in $Al_{65}Cu_{20}Ru_{15}$ reported by Biggs et al.

5. High Temperature NMR

Through low temperature NMR measurements we have found evidence for the pseudogap in both K_{iso} and $2W_M$ measurements. However, the compositional study results of Table 6.3, as well as the NMR pressure study of $Al_{65}Cu_{20}Ru_{15}$, show no evidence of pseudogap fine structure. Hill et al. [15] have recently analyzed Knight shift and spin-lattice relaxation data up to 1,100 K and have proposed a method for that emphasizes and

interpretation of the data as the result of pseudogap fine structure. We will briefly discuss their methods and conclusions.

Fig. 6.5 compares our $2W_M$ data for $Al_{68}Cu_{17}Ru_{15}$ with those of Hill et al. for $Al_{65}Cu_{20}Ru_{15}$. The good agreement between samples is consistent with the results of Table 6.3, which indicate no dependence of NMR properties on composition. In addition, the results verify the deviation from linear behavior in $2W_M$ at room temperature and above. Hill et al. reported that above 700 K, a dramatic temperature dependence of the Knight shift is observed, where the Knight shift changes by nearly a factor of 3 up to a temperature of 1,100 K. Such a strong temperature dependence of the Knight shift is unusual, though it has been seen in normal metals such as cadmium.

Hill et al. analyze their data with the following expressions:

$$2W_M = W_0\left(T + \frac{\pi^2 k_B^2}{3}\frac{D''(E_F)}{D(E_F)}T^3\right) \tag{6.26}$$

$$K_{iso} = K_{iso}(0)\left\{1 + \frac{\pi^2 k_B^2}{6}\left[\frac{D''(E_F)}{D(E_F)} - \left(\frac{D'(E_F)}{D(E_F)}\right)^2\right]T^2\right\} \tag{6.27}$$

where the derivatives of the density of states arise from higher order corrections that are expected to occur if the density of state exhibits high curvature, i.e. fine structure [15]. However, the corrections were obtained by approximating integrals of the form

$$\int_{-\infty}^{\infty} D(E_F)\frac{\partial f}{\partial E}dE \tag{6.28}$$

where $\partial f/\partial E$ is the derivative of the Fermi function

$$f(E) = \frac{1}{e^{(E-E_F)/k_BT} + 1} \tag{6.29}$$

Such integrals may be approximated by series expansions in temperature if the density of states does not vary too rapidly on a scale of k_BT [69]. Hill et al therefore apply the above equations to data from 150 K to 500 K, and obtain the following derivative ratios from fits using the above equations: $D''(E_F)/D(E_F) = 490\ eV^{-2}$ and $D'(E_F)/D(E_F) = \pm 22\ eV^{-1}$.

Hill et al. calculated the width of the pseudogap assuming these derivatives and approximating the shape of the pseudogap with a parabola, and found a full width at half maximum of 0.26 eV. We note that this width is 10 times larger than the 0.02 eV upper limit necessary to account for the change in sign of the thermopower reported by Biggs et al. [31].

We note, however, that the temperature dependence of the Knight shift in cadmium metal was explained by Kasowski [70] without assuming fine structure in the pseudogap. In Kasowski's model, the pseudogap was created by the unusually strong crystal potential in cadmium, which causes a decrease in the density of states at the Fermi level as compared with that of the free electron value. The temperature dependence of the Knight shift was adequately explained by the temperature dependence of the atomic potential, determined by the thermal vibrations of the atoms through the Debeye-Waller factor. At higher temperatures the thermal motions of the nuclei reduce the effective potential and make the density of states come closer to the free electron value. It is therefore conceivable that the temperature dependence of the Knight shift in quasicrystalline $Al_{65}Cu_{20}Ru_{15}$ may be explained without assuming fine structure in the pseudogap, as Hill et al. do.

We conclude that the results of Hill et al. yield an approximate pseudogap width that is an order of magnitude too large to explain the anomalous thermopower data of Biggs et al. However, the width is qualitatively consistent with the lack of any detectable pressure dependence we observed in the NMR parameters of $Al_{65}Cu_{20}Ru_{15}$ up to pressures of 2,000 atm. All the NMR available therefore consistently suggest a lack of pseudogap fine structure on a scale that would explain the anomalous thermopower and specific heat data of Biggs et al.

CHAPTER 7. SUMMARY AND CONCLUSIONS

^{27}Al NMR spectra in the AlCuFe and AlCuRu quasicrystalline and crystalline approximant phases give clear evidence for a quasicontinuous distribution of electric field gradient (EFG) tensor components at the aluminum sites. The quadrupole perturbed NMR spectra were analyzed with a lineshape simulation program, and we found that a gaussian distribution of quadrupole coupling constants gave satisfactory agreement with the experimental data. Guided by the quadrupole interaction strengths inferred from the NMR spectra, we were able to observe, for the first time in quasicrystals, the ^{27}Al NQR spectrum at 4.2 K. The NMR and NQR data were found to be in good agreement, and both unambiguously indicate the existence of a very wide distribution of quadrupole interactions at the aluminum sites. A model calculation of the aluminum electric field gradients in AlCuRu was successful in explaining the observed quadrupole interactions. In particular, we concluded that the unusually wide distribution of quadrupole resonance frequencies in the NQR spectrum may be explained by a multiplicity of non-equivalent aluminum sites within the quasilattice, which gives rise to a wide distribution of EFG values associated with the contribution of the surrounding ionic charges. The average EFG value is largely determined by the Al atomic p - wave function, which is assumed to be the same for all aluminum sites. We obtained a lower limit of approximately 50 non - equivalent aluminum sites, based on a reasonable value for the width of each NQR component of the spectrum due to lattice defects and strains. In addition, ^{27}Al NMR in a single grain AlPdMn quasicrystal gave evidence that a distribution of local EFG principal axis orientations exists, and shows no preference for direction within experimental uncertainty. ^{63}Cu NMR was less conclusive, but indicated that the average experimental EFG at the copper sites is significantly less than the average EFG at the aluminum sites. Since the calculation of the lattice contribution to the EFG yields comparable results at the aluminum and copper sites, we tentatively concluded that the

difference observed should be ascribed to a more s - like symmetry of the valence electronic wave function at the copper sites with respect to the aluminum sites.

The values of the ^{27}Al Knight shift, relaxation time, and bulk magnetic susceptibility measurements, confirm the existence of a pseudogap in the electronic density of states in both AlCuFe and AlCuRu, consistent with the large overlap of the highly symmetric pseudo-Brillouin zone boundary and the Fermi surface. In AlCuFe, the 3/2 approximant phase had Knight shift and relaxation time measurements that are the same as those for the quasicrystal, within experimental uncertainty. This is consistent with the view that the electronic properties are determined by intermediate - range, rather than long - range, order. In AlCuRu, no dependence of Knight shift or relaxation rate on copper concentration occurred within experimental uncertainty, and we found no pressure dependence in either the ^{27}Al / ^{65}Cu Knight shift or spin - lattice relaxation times up to 2,000 atm. We conclude that, on an energy scale of $\approx$ 0.02 eV, the s - band density of states in AlCuRu shows no unusually rapid variations of the kind previously proposed to account for specific heat and thermopower data in the AlCuRu system.

REFERENCES

[1] P. J. Steinhardt, S. Ostlundt, *The Physics of Quasicrystals*, (World Scientific, New Jersey, 1987).

[2] C. Janot, *Quasicrystals: A Primer*, (Clarendon Press, Oxford 1992).

[3] D. P. DiVincenzo, P. J. Steinhardt, *Quasicrystals: The State of the Art*, (World Scientific, New Jersey, 1991).

[4] W. W. Warren, H. S. Chen, J. S. Hauser. Phys. Rev. B, **32**, 7614 (1985).

[5] M. Rubinstein, G. H. Stauss. J. Mater. Res., **1**, 243, (1986).

[6] K. R. Carduner, B. H. Suits, J. A. DiVerdi, M. D. Murphy, D. White. J. Mater. Res. **2**, 431 (1987).

[7] C. Lee, D. White, B. H. Suits, P. A. Bancel, P. A. Heiney. Phys. Rev. B, **37**, 9053 (1988).

[8] E. Jeong, J. C. Holzer, A. E. Carlsson, M. S. Conradi, P. A. Feddars, K. F. Kelton. Phys. Rev. B, **41**, 1695 (1990).

[9] A. R. Drews, M. Rubinstein, G. H. Stauss, L. H. Bennet, L. J. Swartzendruber. J. Alloys Comp., **190**, 189 (1993).

[10] A. Shastri, F. Borsa, A. I. Goldman, J. E. Shield, D. R. Torgeson. J. NonCrys. Solid, **153&154**, 347 (1993).

[11] H. Yasuoka, A. Soyama, K. Kimura, S. Takeuchi. J. Phys. Soc. Japan, **55**, 1058 (1986).

[12] F. Hippert, L. Kandel, Y. Calvayrac, B. Dubost. Phys. Rev. Let., **69**, 2086 (1992).

[13] T. Shinohara, A. P. Tsai, T. Masumoto. J. Mater. Res, **7**, 62 (1992).

[14] H. Fujimaki, K. Motoya, H. Yasuoka, K. Kimura, T. Shibuya, S. Takeuchi. J. Phys. Soc. Japan, **60**, 2067 (1991).

[15] E. Hill, T. C. Chang, Y. Wu, S. J. Poon, F. S. Pierce, Z. M. Stadnick, to Be Published (1993).

[16] C. Kittel, *Introduction to Solid State Physics*, (Wiley, New York, 1976).

[17] V. Elser, Acta Cryst., **A42**, 36 (1986).

[18] S. J. Poon. Adv. Phys., **41**, 303, (1992).

[19] A. Katz, M. Duneau, J. Physique, **47**, 181 (1986).

[20] A. I. Goldman, M. Widom. Annu. Rev .Phys. Chem., **42**, 685 (1991).

[21] C. Janot, M. Audier, M. De Boissieu, J. M. Dubois, Europhys. Lett., **14**, 355 (1991).

[22] J. E. Shield, C. Hoppe, R. W. McCallum, P. C. Gibbons, K. F. Kelton, A. I. Goldman, Phys. Rev. B, **45**, 2063, (1992); J. E. Shield, R. W. McCallum, A. I. Boldman, P. C. Gibbons, K. F. Kelton, J. Non-cryst. Solids, **153 & 154**, 504, (1993).

[23] C. A. Guryan,, A. I. Goldman, P. W. Stephens, K. Hiraga, A. P. Tsai, A. Inoue, T. Masumoto, Phys. Rev. Lett., **62**, 2409 (1989).

[24] S. W. Kycia, A. I. Goldman, T. A. Lograsso, D. W. Delaney, D. Black, M. Sutton, E. Dufresne, R. Bruening, B. Rodricks. Phys. Rev. B, **48**, 3544 (1993).

[25] A. Sadoc, J. M. Dubois, Phil. Mag. B, **66**, 541 (1992).

[26] R. Hu, T. Egami, A. P. Tsai, A. Inoue, T. Masumoto, Phys. Rev. B. **46**, 6105 (1992).

[27] P. A. Bancel, P. A. Heiney, Phys. Rev. B, **33**, 7917 (1986).

[28] V. G. Vaks, V. V. Kamyshenko, B. D. Samdyuk, Phys. Lett. A, **132**, 131 (1988).

[29] T. Fujiwara, T. Yokokawa, Phys. Rev. Lett., **66**, 333 (1991).

[30] J. L. Wagner, B. D. Biggs, S. J. Poon, Phys. Rev. Lett., **65**, 203 (1990).

[31] B. D. Biggs, S. J. Poon, N. R. Munirathnam, Phys, Rev. Lett., **65**, 2700 (1990).

[32] N. F. Mott, E. A. Davis, *Electronic Processes in Non-crystalline Materials*, (Clarendon Press, Oxford, 1971).

[33] A. E. Carlsson, J. Non-cryst. Solids, **153 & 154**, 386 (1993).

[34] C. P. Slichter, *Principles of Magnetic Resonance*, 3rd ed., (Springer - Verlag, New York 1990).

[35] A. Abragam, *Principles of Nuclear Magnetism*, (Clarendon Press, Oxford, 1989).

[36] H. Chihara, N. Nakamura, Landolt - Boernstein New Series III: Crystal and Sol. Phys., **20**, pp. 2 - 18.

[37] D. Mueller, B. Wolfgang, G. A. Ruediger, Z. Chem., **17**, 453 (1977).

[38] P. C. Taylor, P. J. Bray. J. Mag. Res., **2**, 305 (1970); P. C. Taylor, J. F. Baugher, H. M. Kriz. Chem. Rev., **75**, 203 (1975).

[39] G. C. Carter, L. H. Bennet, D. J. Kahan, *Metallic Shifts in NMR*, (Pergamon Press, Oxford, 1977).

[40] A. Narath. Phys. Rev., **162**, 320 (1967).

[41] A. I. Goldman, J. E. Shield, C. A. Guryan, P. W. Stephens. Proc. 25th Anniversary Adriatico Research Conf. on Quasicrystals, eds. M. Jaric and S. Lundqvist (World Scientific, 1990), p. 60.

[42] M. Audier, P. Guyot. Proc. 25th Anniversary Adriatico Research Conf. on Quasicrystals, eds. M. Jaric and S. Lundqvist (World Scientific, 1990), p. 74.

[43] P. Bancel. Phys. Rev. Lett., **63,** 496 (1990).

[44] J. M. Dubois, C. Dong, C. Jonot, M. de Boissieu, M. Audier. Phase Transitions, **32**, 3 (1991).

[45] J. E. Shield, private communication, (1994).

[46] C. Swenson, unpublished (1994).

[47] D. J. Adducci, B. C. Gerstein, Rev. Sci. Instrum., **50**, 1403 (1979).

[48] D. R. Torgeson, unpublished.

[49] D. J. Adducci, P. A. Hornung, D. R. Torgeson, Rev. Sci. Instrum., **47**, 1503 (1976).

[50] C. Dimitropoulos, M. Maglione, F. Borsa, Phys. Rev. B, **37**, 3159 (1988).

[51] D. R. Torgeson, unpublished.

[52] E. R. Andrew, D. P. Tunstall. Proc. of Phys. Soc., **78**, 1 (1961).

[53] W. H. Jones, T. P. Graham, R. G. Barnes, Phys. Rev., **132**, 1898 (1963).

[54] R. R. Hewitt, T. T. Taylor, Phys. Rev. B, **125**, 524 (1962).

[55] K. Ishida, et al., J. Phys. Soc. Japan, **62**, 2803 (1993).

[56] Z. Tan, et. al., Physica C, **156**, 137 (1988).

[57] D. E. MacLaughlin, M. Daugherty, Phys. Rev. B, **6**, 2502 (1972).

[58] E. Cocayne, et. al., J. Non-Crys. Solids, **153&154**, 140 (1993).

[59] M. H. Cohen, R. Reif, *Solid State Physics,* edited by F. Seitz and D. Turnbull, (Academic Press, New York 1957), Vol. 5, p. 321.

[60] E. N. Kaufmann, R. J. Vianden, Rev. Mod. Phys., **51**, 161 (1979).

[61] R. G. Barnes, W. V. Smith, Phys. Rev., **93**, 95 (1954).

[62] J. Ostenson, unpublished (1993).

[63] E. Hill, private correspondence, (1993).

[64] Y. Yafet, V. Jacarino, Phys. Rev., **133**, A1630 (1964).

[65] B. D. Biggs, Y. Li, S. J. Poon, Phys. Rev. B, **43**, 8747, (1991).

[66] T. Kushida, J. C. Murphy, Phys. Rev. B, **3**, 1574 (1971).

[67] E. F. Byars, R. D. Snyder, *Engineering Mechanics of Deformable Bodies*, 3rd ed, (Thomas Y. Crowell Co, 1975) p. 82.

[68] U. Koester, W. Liu, H. Liebertz, M. Michel, J. Non-cryst. Solids, **153 & 154**, 446 (1993).

[69] N. W. Ashcroft, N. D. Mermin, *Solid State Physics*, (Holt, Rinehart, and Winston, 1976).

[70] R. V. Kasowski, L. M. Falicov, Phys. Rev. Lett., 1001, (1969).

ACKNOWLEDGEMENTS

This work was completed with the help of many individuals.

I thank my advisor, Dr. F. Borsa, and D. R. Torgeson, for help with the theoretical and practical aspects of NMR. Thanks go also to Dr. J. E. Shield, and S. W. Kycia for supplying various samples, and Dr. A. I. Goldman for details that helped in my understanding of quasicrystals. I owe a great deal to D. B. Baker, at the time a graduate student at Washingtion University in St. Louis, MO, and Dr. M. S. Conradi, for their help in running the high pressure NMR experiment. In the process, I learned a great deal. Dr. C. Swenson made very useful comments in the progress of this work, and his suggestions were always well focussed and useful. Dr. S. Qiu gave several useful suggestions in the writing of the electric field gradient simulation, and was extremely patient in the process.

However, the people most directly responsible for the completion of this work are my parents, my sisters, my wife, and my daughter. This project was completed with their support.

This work was performed at Ames Laboratory under Contract No. W-7405-eng-82 with the U.S. Department of Energy. The United States government has assigned the DOE Report number IS-T 1731 to this thesis.

APPENDIX 1: NMR LINESHAPE SIMULATION PROGRAM

We now describe in detail the NMR lineshape simulation program, which, given the distributions of parameters ν_Q, η, K_{iso}, K_{an}, and ε that describe the Knight shift and quadrupole interactions, will calculate a composite NMR powder pattern.

In Chapter 3, the NMR spectrum for a single non-equivalent site and fixed orientation θ, ϕ of the electric field gradient principal axis system with the static field was described and shown in Fig. 3.2. The intensity for each $m \leftrightarrow m - 1$ transition is given by the magnetic dipole matrix element $I(I + 1) - m(m - 1)$, and the frequency at which each transition occurs is given in Chapter 3 by eqn.s (3.28) - (3.33).

The powder pattern is simulated over a frequency range $[\nu_1, \nu_2]$ by dividing the interval into N_1 intervals of width $\Delta\nu$

$$\Delta\nu = \frac{\nu_2 - \nu_1}{N_1} \tag{A1.1}$$

and by dividing space into increments of solid angle of value

$$\Delta\Omega(\theta,\phi) = \Delta\theta\Delta\phi\sin\theta \tag{A1.2}$$

where

$$\Delta\theta = \Delta\phi = \frac{\pi}{N_2} \tag{A1.3}$$

We typically took $N_1 = N_2 = 100$.

The simulated NMR spectrum is best described as a histogram with bin widths $\Delta\nu$, and with an intensity $I(\nu_0)$ given by the sum over $I(I + 1) - m(m - 1)$ for all nuclear transitions $\nu(\theta,\phi)$, given by eqn.s (3.28) - (3.33), that meet the resonance condition within the width of the histogram bin, i.e. $\nu_0 \le \nu(\theta,\phi) \le \nu_0 + \Delta\nu$. For powders, the grains are oriented at random, and the number of grains oriented at angle θ is proportional to $\Delta\Omega/4\pi$. Therefore, the simulated lineshape is determined by

$$I(\nu_0) \propto \sum_m \sum_{\theta,\phi} \left(I(I+1) - m(m-1)\right) \frac{\Delta\Omega(\theta,\phi)}{4\pi} \tag{A1.4}$$

where it is understood that a contribution to the sum over theta and phi occurs only when the resonance condition is met. As a programming shortcut, one may notice from the formulas for the transition frequencies that the angular dependence of all the terms is described by linear combinations of the spherical harmonics $Y_{20}(\theta,\phi)$, $Y_{22}(\theta,\phi), Y_{2\bar{2}}(\theta,\phi)$. The symmetries of these terms allow one to reduce the angular sum over all space, in eqn. (A1.4), to the first octant.

The above algorithm describes how an NMR lineshape may be calculated given full knowledge of the distribution of transition frequencies. To include distributions over the electric field gradient tensor components ν_Q, η, additional loops were added to the program. Powder patterns were calculated for specific values of ν_Q and η, and the final composite powder pattern was obtained from the weighted sum

$$I_c(\nu_0) = \sum_{\nu_Q,\eta} F(\nu_Q)G(\eta)I(\nu_0) \qquad \text{(A1.5)}$$

where it is understood that $I(\nu_0)$ was determined from a single non-equivalent site with ν_Q and η, and where F and G are distribution functions of the tensor parameters.

The FORTRAN codes for both field and frequency scans follow.

```
ccccccccccccccccccccccccccccccccccccccccccccccccccccccccc
c       sim6.for
ccccccccccccccccccccccccccccccccccccccccccccccccccccccccc
c       June 8, 1993
c       Ananda Shastri
ccccccccccccccccccccccccccccccccccccccccccccccccccccccccc
c             Contents
c       ---------------
c       I.  Introduction
c       II.  Program Description
c          A.  Field Scan Simulation
c          B.  First and Second Order
c              Quadrupole Effects
c          C.  Convolution:  Used for
c              Distribution of Sites
```

```
c
c I.  Introduction
c     ------------
c sim4.for calculates the NMR spectrum for quasicrystalline
c materials following the method of Warren , et.al [1].
c Standard line shape numerical synthesis methods have
c been taken from papers [2-4]. Reference [4] gives explicit
c formulas for the first and second order contributions to
c level spacings and was used for programming these interactions.
c  For a description of the workings of the program, programming
c shortcuts used, testing, and problems, see A. Shastri's notebook
c "Al-Pd-Mn NMR" .

c II.  Program Description
c      -------------------
c
c  A. Field Scan Simulation.  This program was written
c       to simulate NMR field scans for a powder.  The program takes
c       input parameters from an input file that
c       must be formatted in the following way:
c
c      1       2       3       4
c1234567890123456789012345678901234567890  (This line for reference only.)
c
c      carrier frequency (Hz) = 24.e6
cnuclear gamma factor (Hz/Tesla) = 11.094e6
c         nuclear spin I     = 2.5
c    asymmetry parameter   eta = 0.
c              mean nuQ (Hz) = 1.6e6
c       deviation of nuQ (Hz) = .22e6
c          theta,phi division = 100.
c          integral tolerance = .01
c      number of field points  = 100.
c      beginning field (Tesla) = 1.9
c      ending field    (Tesla) = 2.3
c       beginning eta          = 0.
c       ending eta               = 0.1
c
c  B.  First and Second Order Quadrupole Effects.  The mechanisms
c       that alter line spacings from the Zeeman level spacings are
c       first and second order quadrupole effects only.  We assume
c       that the anisotropic Knight shift is negligible.
c
```

```
c   C. Convolution:  Used for Distribution of Sites.  For materials
c          that have a broad distribution of inequivalent sites, a distri-
c          bution over those sites must be included in the program to
c          "smear" the line.  This is done by a loop that calls the
c          lineshape generating subroutinge for a range of nuQ values,
c          and weights the resulting lineshape with a gaussian
c          weighting factor.  The distribution over nuQ is uniform.
c
ccccccccccccccccccccccccccccccccccccccccccccccccccccccccc
c References
c [1]  W.W.Warren et.al. PRB, 32, 7614 (1985)
c [2]  J.F.Bauger et.al. J.Chem.Phys., 50, 4914 (1969)
c [3]  H.Ebert et.at. J.Phys.F., 16, 1287 (1987)
c [4]  P.C.Taylor et.al., J.Mag.Res., 2, 305 (1970)
c [5]  R.B.Creel et.al., J.Chem.Phys., 60, 2310 (1974)
ccccccccccccccccccccccccccccccccccccccccccccccccccccccccc

      external LineShape
      double precision Hprime,pi,num,xx
      double precision field(300),spect(300),spectrum(300),etasum(300)
      double precision func,LineShape,error,hQmean,gbar,etabeg,etaend
      double precision  I,m,eta,nu0,nuQ,divsn,dH,Hbeg,Hend,dTheta,dPhi,nuL
      integer N
      character*34 a1
      parameter (pi=3.1415926)

      read(5,30) a1,nu0,a1,gbar,a1,I,a1,nuQ,a1,sigmaf,
     #          a1,divsn,a1,error,a1,num,a1,Hbeg,a1,Hend,a1,
     #          etabeg,a1,etaend

      write(6,20) 'TitleText: ', nu0,I,etabeg,nuQ,sigmaf,divsn,error,num
      write(6,*) '"Simulation"'
20    format(a14,' ',d7.2,' ',d7.2,' ',d7.2,' ',d7.2,' ',d7.2,' ',d7.2
     #     , ' ',d7.2,' ',d7.2)

      dTheta=Pi/2./divsn
      dPhi=  Pi/2./divsn
      esq=eta*eta

      do eta=etabeg,etaend,0.1

        xxbeg=nuQ-5*sigmaf
        xxend=nuQ+5*sigmaf
```

```
        xxinc=10*sigmaf/60.
        do xx=xxbeg,xxend,xxinc
       call LineShape(Hbeg,Hend,num,xx,nu0,gbar,dTheta,dPhi,I,eta,
     #                    esq,field,spect,MaxH)
         gauss=exp(-(xx-nuQ)*(xx-nuQ)/2/sigmaf/sigmaf)/sigmaf/sqrt(2*
     *                                        Pi)
          do j=1,MaxH
           spectrum(j)=spectrum(j)+gauss*spect(j)
          enddo
        enddo
        do j=1,MaxH
         etasum(j)=etasum(j)+spectrum(j)
        enddo
      enddo

       xnorm=0.
       do j=1,MaxH
         xnorm=xnorm+etasum(j)
       enddo

       xnorm=xnorm/MaxH
       do  j=1,MaxH
        spectrum(j)=spectrum(j)/xnorm
        write(6,10) field(j),spectrum(j)
       enddo


10    format(e15.7,e15.7)
30    format(a34,g15.7)
       end

ccccccccccccccccccccccccccccccccccccccccccccccccccccccccccccccccccc
       subroutine LineShape(Hbeg,Hend,xnum,xnu,xnu0,gbar,dTheta,dPhi,I,e,esq,
     *                            field,spect,MaxH)
       implicit integer (j-n)
       implicit double precision (a-i,o-z)
       double precision spect(300),field(300)
       double precision x1(20),x2(20),x3(20),x4(20),x13b(200)
       double precision x19(40000),x20(40000),x21(40000)
       double precision x22(1000),x23(1000)
       parameter (Pi=3.1415926)

       dH=(Hend-Hbeg)/(xnum-1.)
```

```
      f=I*(I+1.)

      j=0
      do 100 x=-I,I
      j=j+1
      x1(j)=x-.5
      x2(j)=2*f-6*x*(x-1.)-3.
      x3(j)=4*f-24*x*(x-1.)-9.
      x4(j)=f-x*(x-1.)
      MaxM=j
100   continue

      k=0
      jj=0
      do 200 Theta=dTheta/2.,Pi/2.,dTheta
      k=k+1
      x5=cos(Theta)
      x7=x5*x5
      x6=3*x7-1.
      x8=x7*x7
      x9=1+x7
      x10=1-x7
      x12=x9*x9
      x13=x10*x10
      x13b(k)=sin(Theta)
      MaxTh=k

       mm=0
       do 300 Phi=dPhi/2.,Pi/2.,dPhi
       mm=mm+1
       jj=jj+1
       x14=cos(2*Phi)
       x15=x14*x14
       x16=1.-x15
       x19(jj)=x13-2./3.*e*(1.-x8)*x14+4./9.*esq*x7*x16
     #      +1./9.*esq*x12*x15
       x20(jj)=x10*(x7+2./3.*e*x7*x14+1./9.*esq*x7*x15
     #            +1./9.*esq*x16)
       x21(jj)=x6-e*x10*x14
       MaxPh=mm
300    continue
200   continue
```

```
      j=0
      do 400 H=Hbeg,Hend,dH
      j=j+1
      x22(j)=H*gbar
      x23(j)=xnu*xnu/8./x22(j)
      MaxH=j
400   continue

      Max=MaxTh*MaxPh

      do 700 j=1,MaxH

       powpat=0.
       do 800 k=1,MaxM
        do 900 l=1,Max
            ll=1+int((l-1)/MaxPh)
            r1=-xnu/2.*x1(k)*x21(l)
            r2=x23(j)*(.25*x2(k)*x19(l) - x3(k)*x20(l))
          freq=x22(j)+r1+r2
            chi=(freq-xnu0)/gbar
            dchi=dH-chi
            if(dchi.gt.0.d0.and.chi.gt.0.d0) powpat=powpat+
     #                        2./Pi*x4(k)*dTheta*dPhi*x13b(ll)/dH
900         continue
800     continue

        H=Hbeg+(j-1)*dH
        field(j)=H
        spect(j)=powpat
700   continue
10    format(e15.7,e15.7)
      return
      end



ccccccccccccccccccccccccccccccccccccccccccccccccccc
c       sim7.for
c Same as sim6 except this is a frequency scan
c Normalization of components patterns corrected
c July 6, 1993.
```

```
ccccccccccccccccccccccccccccccccccccccccccccccccccccc
c       July 6, 1993
c       Ananda Shastri
ccccccccccccccccccccccccccccccccccccccccccccccccccccc
c            Contents
c       ---------------
c       I.  Introduction
c       II.  Program Description
c          A.  Frequecny Scan Simulation
c          B.  First and Second Order
c              Quadrupole Effects
c          C.  Convolution:  Used for
c              Distribution of Sites
c
c I.   Introduction
c      ------------
c sim4.for calculates the NMR spectrum for quasicrystalline
c materials following the method of Warren , et.al [1].
c Standard line shape numerical synthesis methods have
c been taken from papers [2-4].  Reference [4] gives explicit
c formulas for the first and second order contributions to
c level spacings and was used for programming these interactions.
c   For a description of the workings of the program, programming
c shortcuts used, testing, and problems, see A. Shastri's notebook
c "Al-Pd-Mn NMR" .

c II.  Program Description
c      -------------------
c
c   A.  Frequency Scan Simulation.  This program was written
c         to simulate NMR freq scans for a powder.  The program takes
c         input parameters from an input file that
c         must be formatted in the following way:
c
c       1       2       3       4
c12345678901234567890123456789012345678901234567890  (This line for reference only.)
c
c      reference frequency (Hz) =  90.963e6
cnuclear gamma factor (Hz/Tesla) =  11.094e6
c          nuclear spin I     =  2.5
c     asymmetry parameter   eta =  0.1
c               mean nuQ (Hz) =  1.6e6
c        deviation of nuQ (Hz) =  .22e6
```

```
c          theta,phi division =  100.
c          integral tolerance =  .01
c       number of freqcy points  =  100.
c        beginning freq  (Hz  ) =  89.e6
c        ending freq     (Hz  ) =  94.e6
c        beginning eta          =  0.1
c        ending eta             =  0.4
c
c   B.  First and Second Order Quadrupole Effects.  The mechanisms
c       that alter line spacings from the Zeeman level spacings are
c       first and second order quadrupole effects only.  We assume
c       that the anisotropic Knight shift is negligible.
c
c   C.  Convolution:  Used for Distribution of Sites.  For materials
c       that have a broad distribution of inequivalent sites, a distri-
c       bution over those sites must be included in the program to
c       "smear" the line.  This is done by a loop that calls the
c       lineshape generating subroutine for a range of nuQ values,
c       and weights the resulting lineshape with a gaussian
c       weighting factor(the lineshape subroutine generates
c       patterns normalized in the frequency domain.
c        The distribution over eta is uniform.
c
ccccccccccccccccccccccccccccccccccccccccccccccccccccccccc
c References
c [1]  W.W.Warren et.al. PRB, 32, 7614 (1985)
c [2]  J.F.Bauger et.al. J.Chem.Phys., 50, 4914 (1969)
c [3]  H.Ebert et.at. J.Phys.F., 16, 1287 (1987)
c [4]  P.C.Taylor et.al., J.Mag.Res., 2, 305 (1970)
c [5]  R.B.Creel et.al., J.Chem.Phys., 60, 2310 (1974)
c [6]  P.C.Taylor et.al.,J.Chem.Phys.,
ccccccccccccccccccccccccccccccccccccccccccccccccccccccccc

      external LineShape
      double precision Hprime,pi,num,xx
      double precision carfr(300),spect(300),spectrum(300),etasum(300)
      double precision func,LineShape,error,hQmean,gbar,etabeg,etaend
      double precision  I,m,eta,nu0,nuQ,divsn,dx,xbeg,xend,dTheta,dPhi,nuL
      integer N
      character*34 a1
      parameter (pi=3.1415926)

      read(5,30) a1,nu0,a1,gbar,a1,I,a1,nuQ,a1,sigmaf,
```

```
#          a1,divsn,a1;error,a1,num,a1,xbeg,a1,xend,a1,
#          etabeg,a1,etaend

      write(6,20) 'TitleText: ', nu0,I,etabeg,nuQ,sigmaf,divsn,error,num
      write(6,*) '"Simulation"'
20    format(a14,' ',d7.2,' ',d7.2,' ',d7.2,' ',d7.2,' ',d7.2,' ',d7.2
#       , ' ',d7.2,' ',d7.2)

      dTheta=Pi/2./divsn
      dPhi=  Pi/2./divsn
      esq=eta*eta

      write(6,*) 'entering eta loop'   !kill
      do eta=etabeg,etaend,0.1

        xxbeg=nuQ-5*sigmaf
        xxend=nuQ+5*sigmaf
        xxinc=10*sigmaf/60.
        if(eta.eq.etabeg) write(6,*) 'entering nuQ loop' !kill
        do xx=xxbeg,xxend,xxinc
          if(xx.eq.xxbeg) write(6,*) 'calling lineshape'  !kill
       call LineShape(xbeg,xend,num,xx,nu0,gbar,dTheta,dPhi,I,eta,
#                     esq,carfr,spect,MaxH)
          if(xx.eq.xxbeg) write(6,*) 'returned from lineshape'
          gauss=exp(-(xx-nuQ)*(xx-nuQ)/2/sigmaf/sigmaf)/sigmaf/sqrt(2*
*                                          Pi)
            do j=1,MaxH
              spectrum(j)=spectrum(j)+gauss*spect(j)
            enddo
        enddo
        do j=1,MaxH
          etasum(j)=etasum(j)+spectrum(j)
        enddo
      enddo

       xnorm=0.
       do j=1,MaxH
         xnorm=xnorm+etasum(j)
       enddo

       xnorm=xnorm/MaxH
       do  j=1,MaxH
        spectrum(j)=spectrum(j)/xnorm
```

```
          write(6,10) carfr(j),spectrum(j)
         enddo


10     format(e15.7,e15.7)
30     format(a34,g15.7)
       end

ccccccccccccccccccccccccccccccccccccccccccccccccccccccccccccccccc
       subroutine LineShape(xbeg,xend,xnum,xnu,xnu0,gbar,dTheta,dPhi,I,e,esq,
     *                      carfr,spect,MaxH)
       implicit integer (j-n)
       implicit double precision (a-i,o-z)
       double precision spect(300),carfr(300)
       double precision x1(20),x2(20),x3(20),x4(20),x13b(200)
       double precision x19(40000),x20(40000),x21(40000)
       double precision x22(1000),x23(1000)
       parameter (Pi=3.1415926)

       dx=(xend-xbeg)/(xnum-1.)
       dH=dx/gbar
       f=I*(I+1.)

       j=0
       do 100 x=-I,I
       j=j+1
       x1(j)=x-.5
       x2(j)=2*f-6*x*(x-1.)-3.
       x3(j)=4*f-24*x*(x-1.)-9.
       x4(j)=f-x*(x-1.)
       MaxM=j
100    continue

       k=0
       jj=0
       do 200 Theta=dTheta/2.,Pi/2.,dTheta
       k=k+1
       x5=cos(Theta)
       x7=x5*x5
       x6=3*x7-1.
       x8=x7*x7
       x9=1+x7
       x10=1-x7
```

```
      x12=x9*x9
      x13=x10*x10
      x13b(k)=sin(Theta)
      MaxTh=k

       mm=0
       do 300 Phi=dPhi/2.,Pi/2.,dPhi
       mm=mm+1
       jj=jj+1
       x14=cos(2*Phi)
       x15=x14*x14
       x16=1.-x15
       x19(jj)=x13-2./3.*e*(1.-x8)*x14+4./9.*esq*x7*x16
     #      +1./9.*esq*x12*x15
       x20(jj)=x10*(x7+2./3.*e*x7*x14+1./9.*esq*x7*x15
     #           +1./9.*esq*x16)
       x21(jj)=x6-e*x10*x14
       MaxPh=mm
300    continue
200   continue


      j=0
      do 400 x=xbeg,xend,dx
      j=j+1
      carfr(j)=x
      x22(j)=xnu0
      x23(j)=xnu*xnu/8./x22(j)
      MaxH=j
400   continue

      Max=MaxTh*MaxPh

      do 700 j=1,MaxH
       powpat=0.
       do 800 k=1,MaxM
        do 900 l=1,Max
            ll=1+int((l-1)/MaxPh)
            r1=-xnu/2.*x1(k)*x21(l)
            r2=x23(j)*(.25*x2(k)*x19(l) - x3(k)*x20(l))
          freq=x22(j)+r1+r2
            chi=(freq-carfr(j))
            dchi=dx-chi
```

```
            if(dchi.gt:0.d0.and.chi.gt.0.d0) powpat=powpat+
     #                        2./Pi*x4(k)*dTheta*dPhi*x13b(ll)/dH
900             continue
800         continue
            spect(j)=powpat
700     continue
        j=1
        do x=xbeg,xend,dx
         sum=sum+spect(j)*dx
         j=j+1
        enddo

        do x=xbeg,xend,dx
         spect(j)=spect(j)/sum
        enddo

10      format(e15.7,e15.7)
        return
        end
```

APPENDIX 2. ELECTRIC FIELD GRADIENT CALCUALATION PROGRAM

As described in Chapter 5, we simulated the electric field gradients at Al and Cu sites in the 1/1 approximant model of Cockayne et al. The coordinates of the non-equivalent sites are given in Table 5.2, from which all the atomic sites within the crystal may be calculated by application of the $P2_13$ symmetry operations of the approximant [58].

```
c       EFG Calculation for AlCuFe, AlCuRu Approximants
c
c       Coordinates are generated from table 1 given in
c       the paper by E. Cocayne et. al. J. Non-Crys. Solids 153-154,
c       (1993) 140-144.
c
ccccccccccccccccccccccccccccccccccccccccccccccccccccccccccc
c
c       Versions and Changes
c       11/17/93, version#3, changed input of ion charges
c               n1,n2,n3 so that
c               they can be read from file efgsym.
c
c       11/11/93, version #3,  diagonalizes the full efg tensor
c               New subroutines are efgtensor, Jacobi, eigsrt (modified
c               from _Numerical Recipes_ version to order the
c               eigenvalues according to the rule |Vzz|>|Vyy|>|Vxx|).
c
c       11/6/93, version #2,  instead of simply a single box
c               with one vertex at the origin, a routine added
c               to translate box to each of 26 positions around
c               original box.  This is to eliminate the finite
c               boundary effects of first calculation.  Subroutines
c               added are Vector(trans) and Move(trans,jmax,E).
c       11/1/93, version #1, calculates Vzz for all Al atoms in
c               the approximant.  Atoms are arranged in a unitless
c               cube of side a=1, with center at the origin.
c
ccccccccccccccccccccccccccccccccccccccccccccccccccccccccccc

      external gensite,check,vector,move,efgtensor,jacobi,eigsrt
      dimension B(200,3), B2(5400,3), trans(27,3)
      dimension V(3,3),Q(3,3),P(3)
```

```
      character*2 C(200), C2(5400), Nuc
      character*3 D(200), D2(5400), Sym
      real*8 xn1,xn2,xn3

      parameter(pi=3.1415926)
      n=3
      jsite=1
      read(5,1) xn1,xn2,xn3
      write(6,*) xn1,xn2,xn3
1     format(f5.2,5x,f5.2,5x,f5.2)
5     read(5,10,end=20) Nuc, Sym, x,y,z
10    format(4x,a2,6x,a2,3x,f5.3,2x,f5.3,2x,f5.3)
      if (Nuc.eq.'**') goto 20
      call gensite(jsite,x,y,z,B,C,D,Nuc,Sym)
      call gensite(jsite,y,z,x,B,C,D,Nuc,Sym)
      call gensite(jsite,z,x,y,B,C,D,Nuc,Sym)
      jmax=jsite
      goto 5
20    continue

      jmax=jmax-1
      junit=jmax

      call vector(trans)
      call move(trans,B,C,D,B2,C2,D2,jmax)

      do k=1,junit
       kk=13*junit+k
       if(C2(kk).eq.'Al')then
        call efgtensor(junit,jmax,kk,xn1,xn2,xn3,B2,C2,V)
        call Jacobi(V,n,n,P,Q)
        call eigsrt(P,Q,n,n)
        theta=acos(Q(1,3))*180/pi
        write(6,*) kk,P(1),P(2),P(3),theta
       endif
      enddo
      end
ccccccccccccccccccccccccccccccccccccccccccccccccccc
c     subroutine gensite
c
c     This subroutine generates the coordinates of the
c     Al, Cu, and Fe(Ru) atoms based upon the symmetry
c     of the site as given in Table 1 of Cockayne's paper.
```

```
c
ccccccccccccccccccccccccccccccccccccccccccccccccc

      subroutine gensite(jsite,x,y,z,B,C,D,Nuc,Sym)

      dimension B(200,3)
      character*2 C(200), Nuc
      character*3 D(200), Sym

      x2=x
      y2=y
      z2=z
      call check(jsite,x2,y2,z2,B,C,D,Nuc,Sym)
      x2=0.5+x
      y2=0.5-y
      z2=-z
      call check(jsite,x2,y2,z2,B,C,D,Nuc,Sym)
      x2=-x
      y2=0.5+y
      z2=0.5-z
      call check(jsite,x2,y2,z2,B,C,D,Nuc,Sym)
      x2=0.5-x
      y2=-y
      z2=0.5+z
      call check(jsite,x2,y2,z2,B,C,D,Nuc,Sym)

      return
      end

ccccccccccccccccccccccccccccccccccccccccccccccccc
c     subroutine check
c
c     This subroutine checks the atomic coordinates
c     generated by the symmetry rules in subroutine
c     gensite and makes sure that the coordinate is
c     in the unit cube and that the coordinate is not
c     a duplicate of a previous symmetry operation.
c     If the coordinate is not in the unit cube, the
c     appropriate translation is performed to move
c     it into the cube.
c
ccccccccccccccccccccccccccccccccccccccccccccccccc
```

```
      subroutine check(jsite,x2,y2,z2,B,C,D,Nuc,Sym)

      parameter(tol=5e-4)
      dimension B(200,3), A(3)
      character*2 C(200), Nuc
      character*3 D(200), Sym

      A(1)=x2
      A(2)=y2
      A(3)=z2

      do k=1,3
       if (0..le.A(k).and.A(k).le.1.) then
         goto 10
       else if (1..le.A(k).and.A(k).le.2.) then
         A(k)=A(k)-1.
         goto 10
       else if (-1..le.A(k).and.A(k).lt.0.) then
         A(k)=A(k)+1.
         goto 10
       else
         write(6,*) 'error 2'
       endif
10     continue
      enddo

      x2=A(1)
      y2=A(2)
      z2=A(3)


      if (jsite.ne.1) then
       do k=1,jsite-1
         xx=abs(x2-B(k,1))
         yy=abs(y2-B(k,2))
         zz=abs(z2-B(k,3))
         if (xx.lt.tol.and.yy.lt.tol.and.zz.lt.tol)then
           goto 30
         endif
       enddo
       B(jsite,1)=x2
       B(jsite,2)=y2
       B(jsite,3)=z2
```

```
          C(jsite)=Nuc
          D(jsite)=Sym
         else
          B(jsite,1)=x2
          B(jsite,2)=y2
          B(jsite,3)=z2
          C(jsite)=Nuc
          D(jsite)=Sym
         endif
         jsite=jsite+1
30       continue
         return
         end
ccccccccccccccccccccccccccccccccccccccccccccccccccccccccccccccccccccc
c        subroutine Vector(trans)
c
c        This subroutine produces the 27 translation vectors
c        that will translate the unit cube to other postions
c        so as to completely surround the central cube, thereby
c        eliminating surface effects.  The vectors are the permutations
c        of -1,0,1.
c
ccccccccccccccccccccccccccccccccccccccccccccccccccccccccccccccccccccc

         subroutine vector(trans)
         dimension trans(27,3)

         j=1
         do k=-1,1
          do l=-1,1
            do m=-1,1
              trans(j,1)=k
              trans(j,2)=l
              trans(j,3)=m
              j=j+1
            enddo
          enddo
         enddo
         return
         end
ccccccccccccccccccccccccccccccccccccccccccccccccccccccccccccccccccccc
c        subroutine move(trans,B,C,D,B2,C2,D2,jmax)
c
```

```
c       This subroutine move the oringinal unit box of  atoms
c       by each of the translation vectors produced in Vector.
c       It keeps track which positions are occupied by which
c       atoms.
c
ccccccccccccccccccccccccccccccccccccccccccccccccccccccccccccccccc

        subroutine move(trans,B,C,D,B2,C2,D2,jmax)

        dimension trans(27,3), B(200,3), B2(5400,3)
        character*2 C(200), C2(5400)
        character*3 D(200), D2(5400)

        do j=1,27
         do k=1,jmax
         kk=(j-1)*jmax+k
         C2(kk)=C(k)
         D2(kk)=D(k)
           do l=1,3
            B2(kk,l)=B(k,l)+trans(j,l)
           enddo
         enddo
        enddo
        jmax=kk
        return
        end
ccccccccccccccccccccccccccccccccccccccccccccccccccccccccccccccccc
c       subroutine efgtensor
c
c       This subroutine calculates the 9 component of the
c       electric field gradient tensor and sums over all
c       the ions in within a sphere of radius 1 (in units of
c       the lattice constant a=12.3 A
c
ccccccccccccccccccccccccccccccccccccccccccccccccccccccccccccccccc

        subroutine efgtensor(junit,jmax,kk,xn1,xn2,xn3,B2,C2,V)

        dimension B2(5400,5400),x(3),V(3,3)
        character*2 C2(5400)
        real*8 xn1,xn2,xn3,xn

         do mm=1,3
```

```
          do nn=1,3
            V(mm,nn)=0.
          do l=1,jmax
             if (l.eq.kk) goto 30
             if (C2(l).eq.'Al') then
                 xn=xn1
                 goto 25
             else if (C2(l).eq.'Cu') then
                 xn=xn2
                 goto 25
             else if (C2(l).eq.'Fe') then
                 xn=xn3
                 goto 25
             else
                 write(6,*) 'error 1'
             endif
25           continue
             do jj=1,3
                 x(jj)=B2(l,jj)-B2(kk,jj)
             enddo
             r=sqrt(x(1)*x(1)+x(2)*x(2)+x(3)*x(3))
             if(r.gt.1.) goto 30
               if(mm.eq.nn)then
              V0=xn*(3*x(mm)*x(mm)/r/r-1)/r/r/r
             else
              V0=xn*3*x(mm)*x(nn)/r/r/r/r/r
             endif
             V(mm,nn)=V(mm,nn)+V0
30           continue
           enddo
          enddo
        enddo

c       do j=1,3
c         do k=1,3
c           write(6,*) 'V(',j,',',k,')=',V(j,k)
c         enddo
c       enddo

        return
        end
ccccccccccccccccccccccccccccccccccccccccccccccccccccccccccccccccccccccc
c       subroutine jacobi.for from _Numerical Recipes_
```

```
c
ccccccccccccccccccccccccccccccccccccccccccccccccccccccccccccccccccccccc

      SUBROUTINE JACOBI(A,N,NP,D,V,NROT)
      PARAMETER (NMAX=100)
      DIMENSION A(NP,NP),D(NP),V(NP,NP),B(NMAX),Z(NMAX)
      DO 12 IP=1,N
       DO 11 IQ=1,N
        V(IP,IQ)=0.
11     CONTINUE
       V(IP,IP)=1.
12    CONTINUE
      DO 13 IP=1,N
       B(IP)=A(IP,IP)
       D(IP)=B(IP)
       Z(IP)=0.
13    CONTINUE
      NROT=0
      DO 24 I=1,50
       SM=0.
       DO 15 IP=1,N-1
        DO 14 IQ=IP+1,N
         SM=SM+ABS(A(IP,IQ))
14      CONTINUE
15     CONTINUE
       IF(SM.EQ.0.)RETURN
       IF(I.LT.4)THEN
        TRESH=0.2*SM/N**2
       ELSE
        TRESH=0.
       ENDIF
       DO 22 IP=1,N-1
        DO 21 IQ=IP+1,N
         G=100.*ABS(A(IP,IQ))
         IF((I.GT.4).AND.(ABS(D(IP))+G.EQ.ABS(D(IP)))
     *      .AND.(ABS(D(IQ))+G.EQ.ABS(D(IQ))))THEN
          A(IP,IQ)=0.
         ELSE IF(ABS(A(IP,IQ)).GT.TRESH)THEN
          H=D(IQ)-D(IP)
          IF(ABS(H)+G.EQ.ABS(H))THEN
           T=A(IP,IQ)/H
          ELSE
           THETA=0.5*H/A(IP,IQ)
```

```
          T=1./(ABS(THETA)+SQRT(1.+THETA**2))
          IF(THETA.LT.0.)T=-T
        ENDIF
        C=1./SQRT(1+T**2)
        S=T*C
        TAU=S/(1.+C)
        H=T*A(IP,IQ)
        Z(IP)=Z(IP)-H
        Z(IQ)=Z(IQ)+H
        D(IP)=D(IP)-H
        D(IQ)=D(IQ)+H
        A(IP,IQ)=0.
        DO 16 J=1,IP-1
          G=A(J,IP)
          H=A(J,IQ)
          A(J,IP)=G-S*(H+G*TAU)
          A(J,IQ)=H+S*(G-H*TAU)
16        CONTINUE
        DO 17 J=IP+1,IQ-1
          G=A(IP,J)
          H=A(J,IQ)
          A(IP,J)=G-S*(H+G*TAU)
          A(J,IQ)=H+S*(G-H*TAU)
17        CONTINUE
        DO 18 J=IQ+1,N
          G=A(IP,J)
          H=A(IQ,J)
          A(IP,J)=G-S*(H+G*TAU)
          A(IQ,J)=H+S*(G-H*TAU)
18        CONTINUE
        DO 19 J=1,N
          G=V(J,IP)
          H=V(J,IQ)
          V(J,IP)=G-S*(H+G*TAU)
          V(J,IQ)=H+S*(G-H*TAU)
19        CONTINUE
        NROT=NROT+1
      ENDIF
21    CONTINUE
22  CONTINUE
    DO 23 IP=1,N
      B(IP)=B(IP)+Z(IP)
      D(IP)=B(IP)
```

```
      Z(IP)=0.
23    CONTINUE
24   CONTINUE
     PAUSE '50 iterations should never happen'
     RETURN
     END
ccccccccccccccccccccccccccccccccccccccccccccccccccccccccccccccc
c       subroutine eigsrt.for from _Numerical Recipes_ (NR)
c       This subrouine sort the  eigenvalues of the
c       EFG tensor and defines the x-,y-,z-axes such that
c       |Vzz|>|Vyy|>|Vxx|.  The NR recipes routine had to be
c       slightly modified at points within the program, and
c       these points are indicated within the code.
c
ccccccccccccccccccccccccccccccccccccccccccccccccccccccccccccccc

     SUBROUTINE EIGSRT(D,V,N,NP)
     DIMENSION D(NP),V(NP,NP),e(3)

     DO 13 I=1,N-1
      K=I
      P=abs(D(I))
      DO 11 J=I+1,N
       IF(abs(D(J)).GE.P)THEN
        K=J
        P=abs(D(J))
          nn=j
       ENDIF
11     CONTINUE
        p=d(nn)
      IF(K.NE.I)THEN
       D(K)=D(I)
       D(I)=P
       DO 12 J=1,N
        P=V(J,I)
        V(J,I)=V(J,K)
        V(J,K)=P
12      CONTINUE
      ENDIF
13   CONTINUE
     RETURN
     END
```